SAPIENZA
UNIVERSITÀ DI ROMA

# Production and Characterization of ZnO/Graphene Devices for Energy Harvesting

**Faculty of Civil and Industrial Engineering**
**Ph.D School on Electrical, Materials and Nanotechnology Engineering**

Ph.D in Nanotechnology Engineering
ING-IND/31- Electrotechnics
XXXI Cycle 2015-2018

**Ph.d Candidate**
**Marco Fortunato**
**1201930**

Supervisor
Professor Maria Sabrina Sarto

A/A 2017-2018

*To my family*

*If we knew what it was we were doing, it would not be called research, would it?*

*A. Einstein*

# Contents

# Abstract

In this thesis, different types of innovative highly performing piezoelectric nanomaterials and nanocomposites have been synthesized and characterized for energy harvesting application. In order to evaluate the piezoelectric properties of the produced materials, a novel approach to quantitatively evaluate the effective piezoelectric coefficient $d_{33}$, trough Piezoresponse Force Microscopy (PFM), has been developed. PFM is one of the most widely used techniques for the characterization of piezoelectric materials at nanoscale, since it enables the measurement of the piezo-displacement with picometer resolution. PFM is a non-invasive and easy to use test method; it requires only a bottom electrode (no need of a top-electrode deposition over the material under test), thus considerably simplifying the test structure preparation. In particular, in order to have a quantitative information on the $d_{33}$ a calibration protocol was developed. To get a macroscale characterization of the piezoelectric coefficient, the PFM signal is averaged over different areas of the sample. The proposed method allows to precisely evaluate the piezoelectric coefficient enabling a proper comparison among the different materials analysed.

Two different classes of piezoelectric materials have been synthesized and characterized:

- zinc oxide nanostructures, in particular zinc oxide nanorods (ZnO-NRs) and zinc oxide nanowalls (ZnO-NWs),
- polyvinylidene fluoride (PVDF) nanocomposites films.

The produced piezoelectric materials were fabricated using process which are cost-effective, time-consuming and easy to scale-up. The ZnO nanostuctures were grown by chemical bath deposition (CBD), that guarantees high deposition rate on a wide variety of substrates. PVDF nanocomposite films were produced with a simple solution casting method, without the need of subsequent electrical poling step. To enhance the piezoelectric properties of PVDF films we investigated different PVDF nanocomposite films:

- PVDF filled with Graphene nanoplatelets (GNPs) or with ZnO-NRs;
- PVDF filled with different types of hexahydrate metal-salts (HMS);
- PVDF filled with HMS in combination with nanofillers, like GNPs or ZnO-NRs.

We found that the piezoelectric coefficient of the ZnO-NRs is (7.01±0.33) pm/V and (2.63±0.49) pm/V for ZnO-NWs. The higher piezoelectric response of ZnO-NRs is believed to be due to a better crystallinity and a less defectiveness of the ZnO-NRs if compared to the ZnO-NWs, as it has been confirmed by X-ray diffraction (XRD) spectra and by photoluminescence spectroscopy (PL) measurements.

The neat PVDF show a $d_{33}$ limited to 4.65 pm/V; when the nanofillers are added the $d_{33}$ increases up to 6 pm/V. This value reaches 8.8 pm/V when a specific hexahydrate metal-salts: [$Mg(NO_3)_2 \cdot 6H_2O$] is dispersed in the PVDF polymer matrix.

From the comparative analysis of the synthesized materials we found that the sample produced using the dissolution of HMS in PVDF shows the best piezoelectric response (8.8 pm/V) and the most attractive structural and mechanical properties to fabricate a flexible nanogenerators. Therefore, a porous piezoelectric HMS-PVDF nanocomposite film has been used as active material to fabricate flexible nanogenerator. To build such a device, graphene-gold flexible top electrodes were developed. The bilayer electrode structure avoids short circuits between top and bottom electrodes, observed in the absence of graphene interlayer. The nanogenerator was tested using a commercial mini-shaker and operated successfully. The piezoelectric coefficient determined from the electromechanical tests was 9.00 pm/V, which is in good agreement with the one (8.88±3.14) pm/V measured through PFM on the same PVDF film without top electrode. We also measured the piezoelectric coefficient of PVDF using PFM with and without top electrode and both values were found to be in close agreement. This finding suggests that the local characterization using PFM is also a good representation of the global piezoelectric properties of the samples.

The progress on advanced piezoelectric materials reported in this work opens new opportunities to fabricate energy harvesters and sensors for wearable and smart clothing applications.

# *CHAPTER I*

## *INTRODUCTION*

# Chapter I

# Introduction

All materials can be categorized according to their electrical conductivity into: conductors, semiconductors, and insulators. Where in conductors and semiconductors, electrons are free to move (in semiconductors under certain condition) an insulator has only bound electrons. Since the electrons cannot move in insulators, when an electric field is applied, they can only be displaced within the unit cell i.e. the can be polarized, causing dielectric polarization. If the dielectric is composed of regions of atoms with homogenous polarization (domains), the applied field not only polarizes those atoms, but also can reorient the domains, so that their symmetry axes align to the field (see Fig. 1).

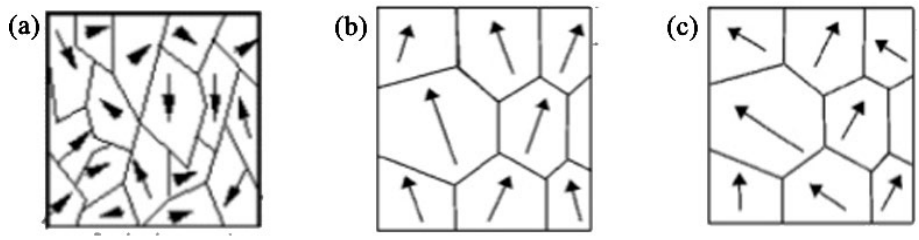


**Fig. 1 Piezoelectric domains in a ceramic (a) before, (b) during and (c) after the application of an external electric field.**

Generally, the polarization varies approximately linearly with the electric field. Another qualification of physical solids can be made on basis of their crystallinity. When atoms or molecules are packed in a regularly ordered repeating pattern, materials are called crystalline. Materials are called single crystal when the crystal lattice of the entire sample is continuous, with no grain boundaries [1]. Several special electrical phenomena can occur in dielectric crystalline materials. Among these of relevance are:

- Piezoelectricity means "pressure electricity", from the Greek verb πιέζειν (*piézein*), which means squeeze or press. It is the phenomenon of some materials of generating an electrical potential in response to an applied stress;

- Pyroelectricity, the phenomenon of some materials of generating an electrical potential when they are heated or cooled;
- Ferroelectricity, the phenomenon of some materials where the spontaneous polarization can be reversed by applying an electric field.

Ferroelectric materials are a sub-group of piezoelectric materials (i.e. all ferroelectrics are piezoelectrics but not all piezoelectrics are ferroelectrics) which are a part of the largest category of dielectric materials. Therefore, piezoelectric materials combine properties of ferroelectric and dielectric materials with the further characteristic of varying their polarization due to an external deformation and vice versa.

In this thesis we will focus on the study of some piezoelectric materials. Piezoelectricity is the property of many materials to develop a polarization (or dielectric displacement) when a mechanical stress is applied (the materials is squeezed or stretched), as sketched in Fig. 2 (a). This phenomenon is called direct piezoelectric effect and the sign of the polarization is reversed according to whether the deformation is due to a compression or a pull. Vice versa, a strain is developed when an electric field is applied, Fig. 2 (b). and in this case the phenomenon is called converse piezoelectric effect.

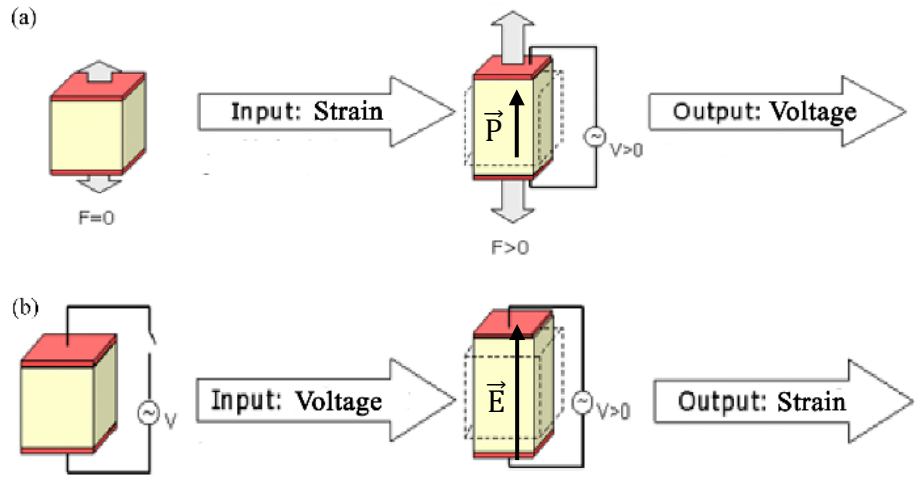


**Fig. 2 Direct piezoelectric effect (a) and converse piezoelectric effect (b).**

Whether a material is piezoelectric depends on its microscopic charge distribution. For example, the charge distribution in Fig. 3 (a), when deformed into Fig. 3 (b), results in a net polarization [2].

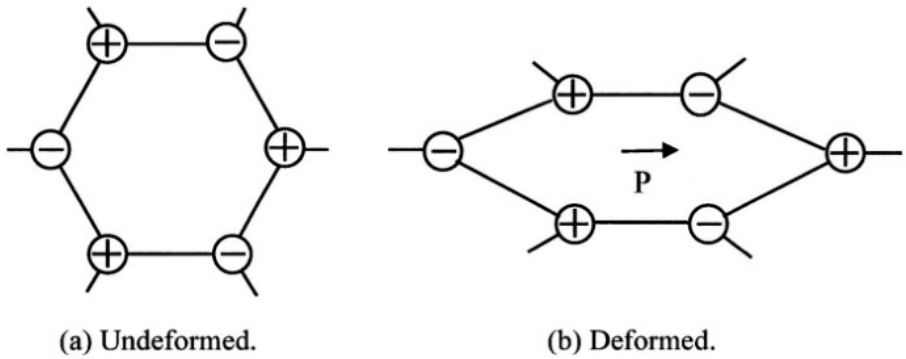


**Fig. 3 Origin of the direct piezoelectric effect [2].**

The first experimental demonstration of the connection between the macroscopic piezoelectric phenomena and the crystallographic structure was published in the 1880 by Pierre and Jacques Curie, who measured the surface charging that appeared on appropriately prepared crystals (i.e. tourmaline, quartz, and salt of Rochelle) subjected to mechanical stress [3]. The first application of piezoelectricity was developed by Langevin, during the first world war, who built the first sonar (an underwater ultrasound source) made by piezoelectric quartz elements interposed between steel plates. The sonar success stimulated the development of other devices exploiting the piezoelectric effect. The crystal frequency control became essential for the broadcasting industry and radio communication. Most of classical piezo applications (microphones, accelerometers, ultrasonic transducers, bending element actuators, phonograph pick-ups, filters of signal, etc.) were developed despite the fact, that the available materials often limited the performance of the devices. During the second world war, the discovery of the possibility to induce the piezoelectricity applying a strong electric field to metal oxides, synthesized in order to align the dipole domains, allowed new piezo-electric applications and opened the way to intense research on piezoceramics. However, it required a long time and the discovery of new materials before piezoelectric devices became competitor to the electro-

dynamic and magnetic based devices, which for a long time were the only way to transform electrical energy or signals into mechanical ones or vice versa effectively. Nowadays the principal research lines on piezoelectric materials are:

- piezoelectric ceramics based on barium titanite and on zirconate titanate lead (PZT).
- crystals and nano-crystals with a perovskite structure
- piezoelectric polymers like Poly[vinylidene fluoride] (PVDF) and its co-polymer poly[vinylidenefluoride-co-trifluoroethylene] (PVDF-TrFE).

The coupling of electrical and mechanical energy makes the piezoelectric materials useful for a wide range of applications, grouped into the following classes:

- Sensors - they take advantage of the direct effect.
- Actuators - they take advantage of the converse effect.
- Energy conversion – convert mechanical energy into electricity or vice versa.

## *1.1 Piezoelectric Effect*

A material can only be piezoelectric if its crystalline structure does not have a symmetry centre or as said is non-centrosymmetric. Among the 32 crystallographic groups 21 are non-centrosymmetric and of these 20 are piezoelectric. A stress (traction or compression) applied to this type of material modifies the position between the sites containing the positive and negative charge in each elementary cell, leading to a net polarization on two opposite surfaces of the crystal. The relationship between the applied stress $\sigma$ and the resulting polarization $P$ is linear:

$$P = d_{\text{direct}} \cdot \sigma \tag{1.1}$$

in which $d_{\text{direct}}$ is the piezoelectric coefficient. This means that the induced polarization varies proportionally with the applied stress and is also dependent on the direction; according to this principle, compressive or tensile stress generates electric fields, and therefore a voltage. In the case of a compressive stress the output voltage has the same polarity of

the crystal domains, while if we apply a tensile stress the output voltage has the opposite polarity of the crystal domains. As already mentioned, the phenomenon is also reciprocal, so the same material, if instead of being subjected to a force it is exposed to an electric field, it will undergo an elastic deformation or strain ε, which causes, to a first approximation, an increase or a reduction of its dimension along the direction of the applied electric field, according to the polarity of the applied field (Fig. 2 (a), (b)):

$$\varepsilon = d_{\text{converse}} \cdot E \tag{1.2}$$

The piezoelectric constant $d_{\text{direct}}$ is conventionally expressed in Coulomb per Newton [C/N] for the converse piezoelectric coefficient $d_{\text{converse}}$ as meter per Volt [m/V]. The coefficient connecting the field and the strain in the converse effect is the same as that connecting the stress and the polarization ($d_{\text{direct}} = d_{\text{converse}}$). The proof of this equality is based on thermodynamic reasoning. More precisely the constitutive relations for a piezoelectric material can be expressed as [4]:

$$D_i = e_{ij}^{\sigma} E_j + d_{im}^{d} \sigma_{jk} \tag{1.3}$$

$$\varepsilon_k = d_{jk}^{c} E_j + s_{km}^{E} \sigma_m \tag{1.4}$$

which can be written as:

$$\begin{bmatrix} D \\ \varepsilon \end{bmatrix} = \begin{bmatrix} e^{\sigma} & d^{d} \\ d^{c} & s^{E} \end{bmatrix} \begin{bmatrix} E \\ \sigma \end{bmatrix} \tag{1.5}$$

where vector $D$ of size (3×1) is the electric displacement (C/m$^2$), $\varepsilon$ is the strain vector (6×1) (dimensionless), $E$ is the applied electric field vector (3×1) (V/m) and $\sigma_m$ is the stress vector (6×1) (N/m$^2$). The piezoelectric constants are the dielectric permittivity $e_{ij}^{\sigma}$ of size (3×3) (F/m), the piezoelectric coefficients $d_{im}^{d}$ (3×6) and $d_{jk}^{c}$ (6×3) (C/N or m/V), and the elastic compliance $s_{km}^{E}$ of size (6×6) (m$^2$/N). The piezoelectric coefficient $d_{jk}^{c}$ (m/V) defines strain per unit field at constant stress and $d_{im}^{d}$ (C/N) defines electric displacement per unit stress at constant electric field. The superscripts *c* and *d* have been added to differentiate between the converse and direct piezoelectric effects, though in practice, these coefficients are numerically equal. The superscripts $\sigma$ and $E$ indicate that the quantity is measured at constant stress and constant electric field respectively. To improve the piezoelectric properties, generally a "*poling*" process is performed, i.e. a high electric field (1--4MV/cm) is applied to

the material to align most of the unit cells as closely parallel to the applied field as possible. Usually, the poling process is carried out at temperatures higher than the room temperature (typically in the range of 60°C--100°C) to be more effective. This process imparts a permanent net polarization to the piezoelectric materials, although not all the dipoles are oriented along the direction of the field, due to the anisotropy that characterizes these materials. To realize the poling process electrodes must be deposited onto the piezoelectric material. The poling procedure is sketched in Fig. 4.

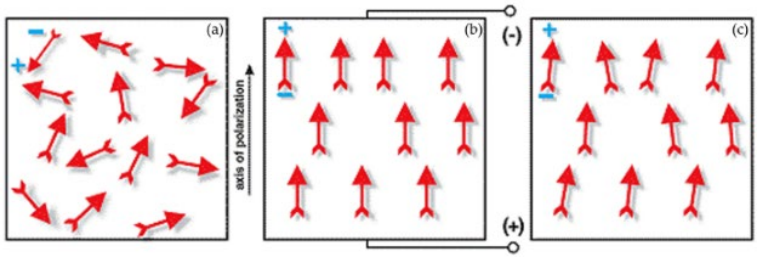


**Fig. 4 Poling procedure: random orientation of polar domains prior to polarization (a); polarization in DC electric field (b); remanent polarization after the electric field is removed (c).**

The direction of the applied field is usually along the thickness and is denoted as the 3- axis and the 1-axis and 2-axis are in the plane of the sheet. The piezoelectric materials are anisotropic materials. For that reason, is necessary to use a notation that allows to identify the directions in which mechanical stresses and electric responses occur and vice versa. The directions X, Y, Z are for convenience of notation indicated respectively with the number 1, 2 and 3, while the rotation around these axes are indicated by numbers 4, 5 and 6, as showed in Fig. 5.

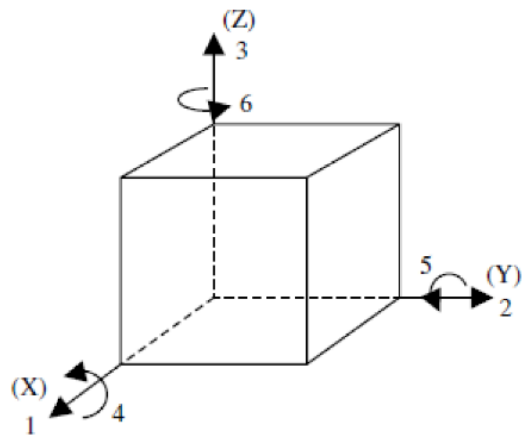


**Fig. 5 Conventional notation of the axes** [5].

The $d_{jk}^{c}$ matrix can then be expressed as:

$$d = \begin{bmatrix} 0 & 0 & d_{31} \\ 0 & 0 & d_{32} \\ 0 & 0 & d_{33} \\ 0 & d_{24} & 0 \\ d_{15} & 0 & 0 \\ 0 & 0 & 0 \end{bmatrix} \tag{1.6}$$

where the coefficients $d_{31}$, $d_{32}$ and $d_{33}$ relate to the normal strain in the 1, 2 and 3 directions respectively to a field along the poling direction, $E_3$. The coefficients $d_{15}$ and $d_{24}$ relate the shear strain in the 1-3 plane to the field $E_1$ and shear strain in the 2-3 plane to the $E_2$ field, respectively. Note that it is not possible to obtain shear in the 1-2 plane purely by application of an electric field.

Generally, the compliance, the permittivity metrics and the stress vector are of the form:

$$s^{E} = \begin{bmatrix} s_{11} & s_{12} & s_{13} & 0 & 0 & 0 \\ s_{12} & s_{22} & s_{23} & 0 & 0 & 0 \\ s_{13} & s_{23} & s_{33} & 0 & 0 & 0 \\ 0 & 0 & 0 & s_{44} & 0 & 0 \\ 0 & 0 & 0 & 0 & s_{55} & 0 \\ 0 & 0 & 0 & 0 & 0 & s_{66} \end{bmatrix} \tag{1.7}$$

$$e^{\sigma} = \begin{bmatrix} e_{11}^{\sigma} & 0 & 0 \\ 0 & e_{22}^{\sigma} & 0 \\ 0 & 0 & e_{33}^{\sigma} \end{bmatrix} \tag{1.8}$$

$$\sigma = \begin{bmatrix} \sigma_1 \\ \sigma_2 \\ \sigma_3 \\ \sigma_4 \\ \sigma_5 \\ \sigma_6 \end{bmatrix} = \begin{bmatrix} \sigma_{11} \\ \sigma_{22} \\ \sigma_{33} \\ \sigma_{23} \\ \sigma_{31} \\ \sigma_{12} \end{bmatrix} \tag{1.9}$$

Equation (1.3) is the formula that describes the direct piezoelectric effect and that is the so called “sensor equation”. The piezoelectric material is exposed to a stress field and generates a charge in response. Equation (1.4) is the formula that describes the converse piezoelectric effect and that is the so called “actuator equation”. The actuator is bonded

to a structure and an external electric field is applied to it, which results in an induced strain field. In the case of a piezoelectric material, where the applied external electric field is zero, Equation (1.5) becomes:

$$\begin{bmatrix} D_1 \\ D_2 \\ D_3 \end{bmatrix} = \begin{bmatrix} 0 & 0 & 0 & 0 & d_{15} & 0 \\ 0 & 0 & 0 & d_{24} & 0 & 0 \\ d_{31} & d_{32} & d_{33} & 0 & 0 & 0 \end{bmatrix} \begin{bmatrix} \sigma_1 \\ \sigma_2 \\ \sigma_3 \\ \sigma_4 \\ \sigma_5 \\ \sigma_6 \end{bmatrix} \tag{1.10}$$

This equation summarizes the principle of operation of piezoelectric materials. A stress field causes surface charging to be generated (Equation 1.10) as a result of the direct piezoelectric effect. Note that shear stress in the 1-2 plane, $\sigma_6$, is not capable of generating any electric response. If we considered a parallelepiped of a piezoelectric material and two electrodes placed on its faces, there are 3 possible types of energy conversion:

- Effect 33 → the stress is applied along the direction 3 (transverse stress) and the voltage is in direction 3: this is the effect that will studied in this thesis.
- Effect 31 → the stress is applied along the direction 1 (longitudinal stress) and the electric field is again in direction 3;
- Effect 15 → the stress is applied along the direction 5 (shear stress) and the tension is in direction 1.

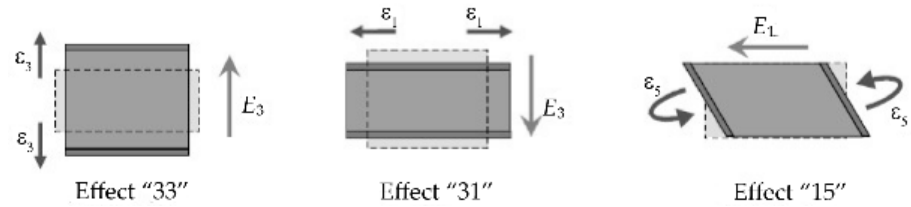


**Fig. 6 Relation stress-voltage [5].**

The behaviour of strain versus applied electric field appears in the shape of a butterfly loop (Fig. 7 (a)). In an ideal case (Fig. 7 (b)), when the electric field ($E$) is applied in the same direction of the polarization the material stretches ($\varepsilon > 0$), as showed in Fig. 7 (b) step 0-1-2. When the electric field is inverted, the material initially contracts, until the electric field reaches an strength equal to the coercive electric field ($-E_c$) capable of reversing the polarization direction of the material, step 0-3-4 in Fig. 7

(b). For $E < E_c$ the direction of dipole is inverted, and the material re-stars to stretch. When the polarization changes direction, the sign of the strain changes and when it is stable the strain is linear with the field. The value of the piezoelectric coefficient is obtained by calculating the slope of the linear part. In real crystals the strain versus applied field assume a characteristic butterfly shape, given by the fact that different polarization orientations are present in the crystal, making the curve smoother in accordance with the change in polarization.

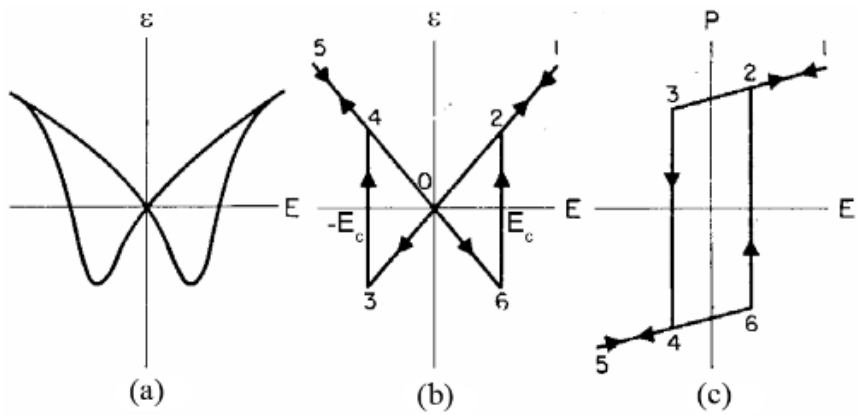


**Fig. 7 Schematic description of the converse piezoelectric effect. Actual butterfly loop (a); theoretical butterfly loop of strain vs field (b); polarization hysteresis loop (c). In (a) and (b), ε denotes the uniaxial strain.**

## *1.2 Piezoelectric Materials*

The main piezoceramics can be grouped depending upon their crystalline structure and they are schematically summarized in Fig. 8. Perovskite ceramics are the most important polycrystalline structures for piezoelectric applications, thanks to the high values of their piezoelectric constants. The most common piezoceramics with a perovskite structure are Barium Titanate ($BaTiO_3$) or Lead Zirconate Titanates [$Pb(Zr,Ti)O_3$ or PZTs]. The $BaTiO_3$ was widely used after the second world war in acoustic and ultrasonic actuators. Today it is generally replaced by PZT for its larger piezoelectric coefficients and higher operating temperatures. A perovskite crystal exhibits a FCC lattice with metallic atoms at the vertices, oxygen atoms at centre of the faces and a heavier atom in the centre of the unit cell. The heavier atom is confined between octahedral spaces, which are positions with lower energy, but in which it cannot

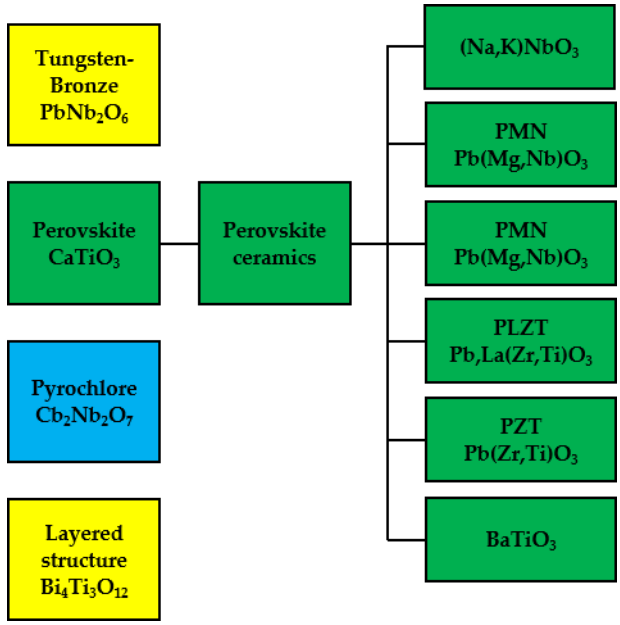


**Fig. 8 Main classes of piezoelectric ceramic materials.**

move without distorting the lattice (as show in Fig. 9 for PZT). It is a metastable structure. Appling an electric field the central atom exceeds the potential threshold and it moves to one of two octahedral spaces realizing a lower energy configuration but leading to an imbalance in the charges that is expressed in the formation of an electric dipole.

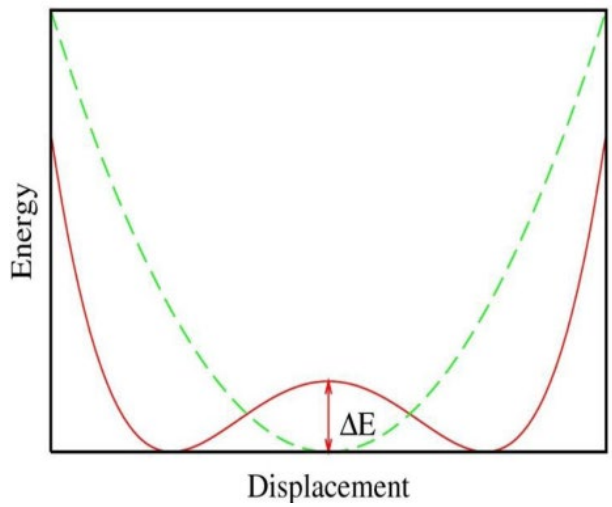


**Fig. 9 One equilibrium position of energy for T>Tc, green line, and two equilibrium position of energy for T<Tc, red line, in function of the displacement of the central cation.**

This behaviour can be verified below the Curie temperature ($T_C$), where the elementary cell is slightly distorted and tetragonal, exhibiting a non-zero dipole moment. Above $T_C$, the elementary cell is cubic and symmetrical, and the piezoelectric effect disappears because of the minor rigidity of the lattice due to greater atomic agitation.

PZT is a solid solution of lead zirconate and lead titanate, often doped with other elements to obtain specific properties. PZT is produced by mixing a proportional amount of lead, zirconium, and titanium oxide powders and heating it to temperatures of 800-1000°C. During subsequent cooling phase, the cubic unit cell of the PZT becomes tetragonal. As consequence the material undergoes to a paraelectric ferroelectric phase transition. The tetragonal cell is elongated in one direction and has a permanent dipole moment oriented along its long axis (c-axis) (Fig. 10).

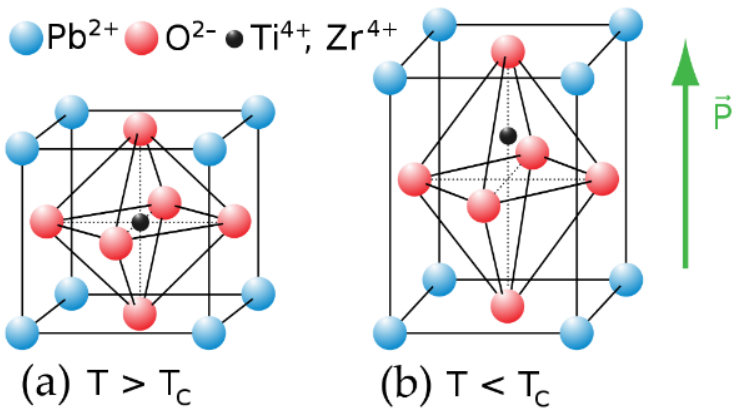


**Fig. 10 Unit cell of perovskite crystals: paraelectric phase, $T>T_C$ (a) and piezoelectric phase with polarization vector pointing upwards $T<T_C$ (b).**

The unpoled ceramic has no net polarization because of the presence of many randomly oriented domains. Appling a high electric field (1--4 MV/cm) we can align most of the unit cells as closely parallel to the applied field as possible. This process, as said, is called "*poling*". PZT exhibit typically characteristics of the piezoelectric ceramics, such us a high elastic modulus, brittleness, and low tensile strength [4].

To overcome the material's brittleness different polymeric piezoelectric materials and nanostructured materials have been investigated. Polymers exhibit a piezoelectric effect thanks to their molecular structure and arrangement. One of the most used piezoelectric polymers is Poly(vinylidene fluoride) [PVDF; $(CH_2CF_2)_n$] a semi-crystalline and ferroelectric polymer. It has attracted much interest due to

its chemical resistance, thermal stability, high mechanical strength, large polarization, short switching time, and peculiar electrical properties. In recent years, PVDF is widely used in organic electronics, biomedical applications, optoelectronics and energy harvesters [6–8].

In PVDF, both amorphous and crystalline phases coexist. Several crystalline phases can be identified in PVDF ($\alpha$-, $\beta$-, $\gamma$-, and $\delta$-phase). The $\alpha$-phase is non-polar and it is the most stable polymorph when PVDF is directly cooled down from the molten state. It has, like the $\delta$-phase, the so called TGTG' (trans-gauche-trans-gauche) chain conformation (Fig. 11). The $\beta$-phase exhibits the strongest ferro-, piezo-, pyroelectric properties, due to its largest spontaneous polarization ($7x10^{-30}$ C·m) [9]. This phase is generally obtained through uniaxial or biaxial stretching of melt-crystallized films [10], melt crystallization under high pressure [11], crystallization from solution under special condition [12] or through the application of high electric fields to PVDF in its $\alpha$-phase [13]. Depending on the processing route, $\beta$-PVDF can be obtained in a porous or non-porous form [14]. The $\beta$-phase present the so called TTT (all trans) planar zigzag chain conformation. The $\gamma$-phase, also piezoelectric, shows the $T_3GT_3G'$ configuration (Fig. 11) [15].

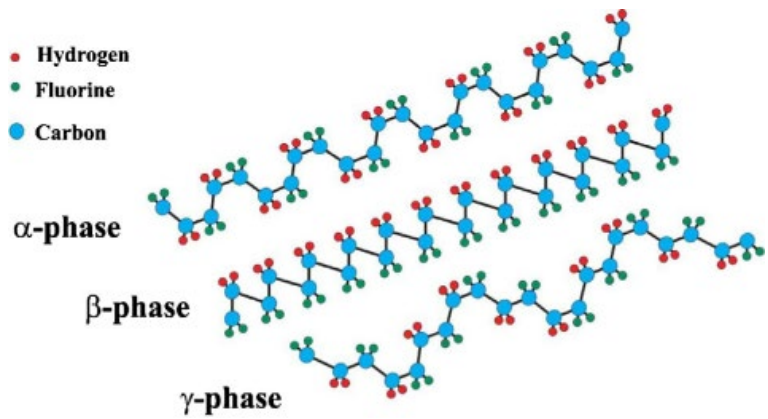


**Fig. 11 Schematic representation of the chain conformation for the $\alpha$, $\beta$ and $\gamma$ phases of PVDF** [15].

Among the piezoelectric nanostructured materials great interest have attracted the zinc oxide (ZnO) nanostructures, such as nanorods (NRs) and nanowalls (NWs). The ZnO nanostructures have high elasticity, hence they can be bent to a large extent. Moreover, the piezoelectric coefficient is much higher for nanostructures as compared to their bulk structure [16]. These properties make the ZnO nanostructures ideal to

develop a flexible nanogenerator with high performance. ZnO is an n-type semiconductor (II-VI) with a wide energy gap (3.37 eV), high exciton binding energy (60meV), high electron mobility, and unique optical, pyroelectric, and piezoelectric properties [17]. It crystallizes in three different forms: hexagonal wurtzite, cubic zincblende and the rarely observed cubic rocksalt. The hexagonal wurtzite-type structure is the most common phase of ZnO and it is showed in Fig. 12. The lattice parameters are $a$=0.32495 nm and $c$=0.52069 nm [18]. The structure is composed of several alternating planes with tetrahedrally-coordinated $O^{2-}$ and $Zn^{2+}$ ions, stacked along the c-axis. The positively charged Zn-(0001) polar surface and negative charged O-(000$\bar{1}$) polar surface are the strongest polarity surfaces. This polar surface present the piezoelectric effect: when a stress is applied, the non-central symmetric structure will lead to the separation of the central point of positive charges and that of negative charges, resulting in a net polarization [19].

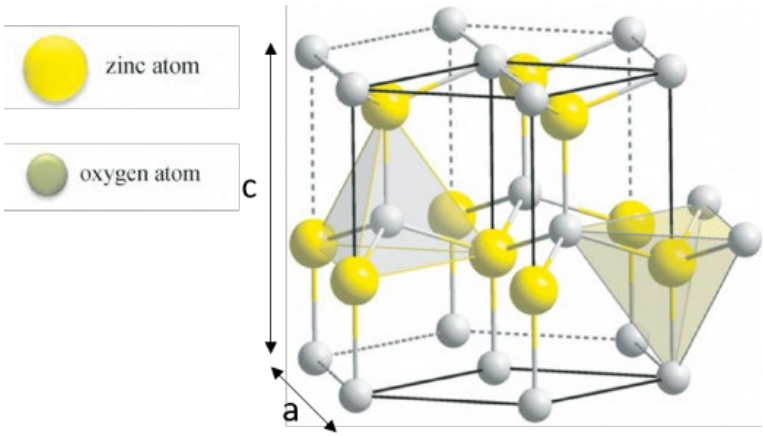


**Fig. 12 Hexagonal wurtzite crystal structure of ZnO.**

## *1.3 Piezoelectric Devices*

One of the most useful applications of the direct piezoelectric effect is in the field of sensors. A sensor is a device that can converts a physical quantity that is to be measured in a signal of different nature, typically electric, more easily measurable. Piezoelectric sensors are active electrical systems; it means that piezoelectric materials produce an electrical output only when there is a variation in the mechanical load (stress). For this reason, they are not able to carry out static measurements. Piezoelectric

sensors are used in all applications that require accurate measurement of dynamic changes of mechanical quantities such as pressure, force and acceleration. They are used in aerospace, ballistic, biomedicine, mechanical and structural engineering. The most used material to realize piezoelectric sensors is quartz ($SiO_2$) thanks to his high resistance to the mechanical stress, high piezoelectric thermal stability up to 500°C, high rigidity, high linearity, constant sensitivity in a wide temperature range and low conductivity. The quartz transducers are made with a layer of crystal cut along any of its axes x, y and z, depending on the specific application. Appling a force the crystal generates a charge of few pC proportional to the applied force. To pick up the electric charge, two conductive electrodes are applied to the crystal at the opposite side (Fig. 13). The piezoelectric effect is simple: when a mechanical force is applied to the crystal, the electric charges move and accumulate on the opposite faces.

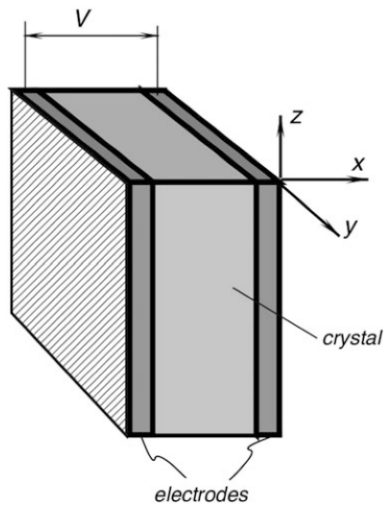


**Fig. 13 Piezoelctric sensor** [20]**.**

In this configuration, the piezoelectric sensor is a capacitor in which the dielectric material, in-between the metal plates, is a piezoelectric crystalline. The dielectric acts as a generator of electric charge, resulting in voltage V across the capacitor. Although charge in a crystalline dielectric is formed at the location of an acting force, metal electrodes equalize charges along the surface making the capacitor not selectively sensitive [20]. Therefore, a piezoelectric sensor is a direct converter of a

mechanical stress into electricity or vice versa a converter of electricity into strain.

Another important application of the piezoelectric materials is as actuator. These devices exploit the converse piezoelectric effect to convert the electrical energy in mechanical energy. For example, an electric motor is an actuator: it converts electric energy into mechanical action.

In recent years great interest was devoted to the use of piezoelectric materials to realize flexible nanogenerators. Such devices can find applications as wearable energy harvesters and sensors for smart clothing applications. Energy harvesting from ambient vibrations originating from sources such as moving parts of machines, fluid flow and even body movement, has enormous potential for small power applications, such as wireless sensors, flexible, portable, wearable electronics, and biomedical implants, to name a few. Vibrational mechanical energy is one of the most present and accessible forms of energy. Random vibrations have frequencies ranging from hundreds of Hz to kHz and the available energy density is in the range of a few hundred microwatts to milliwatt per cubic centimetre [21]. In this specific sector great interest has been attracted by piezoelectric polymers, such as PVDF ant its co-polymer such us PVDF-TrFe, semiconducting metal oxide nanomaterials such as ZnO and novel polymer-based piezoelectric composites.

## *1.4 Thesis Objective and Organization*

Piezoelectric nanomaterials and novel polymer-based piezoelectric composites with enhanced electromechanical properties open new opportunities to the development of wearable energy harvesters and sensors for smart clothing applications.

The objectives of this thesis are:

- to develop new piezoelectric materials, suitable for the fabrication of low-cost flexible nanogenerators;
- define a characterization protocol, based on the Piezoresponse Force Microscopy (PFM), allowing quantitative evaluation of the piezoelectric response, to easily compare different materials and using simple test structures;
- demonstrate a flexible nanogenerator based on the developed piezoelectric materials.

Among the different emerging piezoelectric materials, we focused on two different classes of piezoelectric materials: zinc oxide nanostructures and piezoelectric polymer nanocomposites based on PVDF.

As already mentioned, Zinc oxide (ZnO) has been attracting a great deal of interest, owing to a variety of intriguing properties, along with a remarkable performance for several applications, such as piezoelectric transducers, photovoltaic devices, gas and bio-sensors, nanoscale optoelectronics and self-powered micro/nanosystems.

Poly(vinylidene fluoride) [PVDF; $(CH_2CF_2)_n$] is a semi-crystalline piezoelectric polymer. Due to its chemical resistance, thermal stability, high mechanical strength, large remnant polarization, short switching time, and unique electrical properties, PVDF has found a wide range of applications in organic electronics, biomedicine, optoelectronics and energy harvesters.

PFM technique is particularly interesting for measuring sub-picometer deformations and mapping piezoelectric domains with a lateral resolution of some nanometres. The success of this technique lies in its versatility, ease of use, non-invasiveness and the possibility of imaging the piezoelectric domains of any type of material without any particular sample preparation procedure. However, PFM does not allow to directly determine the absolute value of the piezoelectric coefficient. To this purpose, in this work, a specific protocol, based on a calibration procedure, has been proposed to provide a quantitative evaluation of the piezoelectric coefficients.

As final test vehicle a flexible piezoelectric nanogenerator has been fabricated by using as active layer the best performing piezoelectric material among those investigated. To this end, we had to also to develop advanced top electrodes, based on graphene-Au bilayers.

Moreover, various characterization techniques, such as field emission scanning electron microscopy (FE-SEM), energy dispersive X-ray analysis (EDX), X-ray diffraction (XRD), X-ray photoelectron spectroscopy (XPS), photoluminescence spectroscopy (PL) and Fourier transform infrared spectroscopy (FT-IR) have been used to probe the properties of the produced materials.

In Chapter II the principle of operation of AFM and the PFM is described. First, the two main operation modes for the AFM, contact- and tapping-mode, are discussed. Then the PFM set-up is described and it is pointed out how to perform the imaging of the piezoelectric domains. Then, a specific protocol, based on a calibration procedure, is proposed to

perform the quantification of the piezoelectric coefficient ($d_{33}$) of the materials studied in this thesis.

Chapter III focusses on the study of two different ZnO nanostructures namely nanorods (NRs) and nanowalls (NWs). These two nanostructured materials have been analysed in terms of morphological and chemical properties using FE-SEM, EDX and XPS. The structural analysis was assessed trough XRD and the defectivity was studied trough PL. The $d_{33}$ is measured trough PFM using the calibration protocol presented in Chapter II.

In Chapter IV, in order to increase the $d_{33}$ of the PVDF films, three different nanocomposites have been studied: PVDF plus nanofillers like GNPs or ZnO-NRs; PVDF plus different HMS and PVDF plus HMS in combination with two different nanofiller either ZnO-NRs or GNPs. The morphology of the produced sample was investigated trough FE-SEM, the presence of the $\beta$-phase was assessed through FT-IR and in the sample with HMS the XRD was used to better understand the role of HMS in the formation of the $\beta$-phase. Finally, the $d_{33}$ of all the produced sample was measured.

In Chapter V the fabrication and the characterization of a flexible nanogenerator based on the best PVDF nanocomposite is presented. To guarantee high flexibility and high conductivity the top and bottom electrodes are made with a bilayer of graphene-gold (GGE). The device was successfully operating and a value of the piezoelectric coefficient of 9.00 pm/V was measured. This value was found in very good agreement with the value obtained through PFM measurements (8.88 ± 3.14) pm/V (measured without top electrode).

In Chapter VI concluding remarks on the synthesis and characterization of the different types of piezoelectric materials investigated in this thesis are reported. Future perspectives are also mentioned.

# *CHAPTER II*

## *SCANNING PROBE MICROSCOPY*

# Chapter II

# Scanning Probe Microscopy

Scanning Probe Microscopy (SPM) includes a vast range of technologies that are based on scanning a sample's surface with a mechanical probe and it is able to give different sample's details. SPM techniques can be divided in two main categories, depending upon the feedback signal: 1) the scanning tunnelling microscopy (STM) where the current is the feedback signal and is suitable only for conducting surfaces; 2) the atomic force microscopy (AFM) where the feedback is related to the van der Waals and Pauli interactions and is suitable for all surfaces. AFM is one of the most used tools in SPM, since it allows the investigations of a wide range of surface properties on any materials, spanning from morphology to piezometric properties. In this chapter, after discussing the experimental setup and the operating principle of AFM, Piezoresponse Force Microscopy (PFM) will be explained and the experimental procedure to perform the domain imaging and the quantitative determination of the piezoelectric coefficient will be illustrated.

## *2.1 Atomic Force Microscopy*

Atomic force Microscopy (AFM) is one of the most important SPM techniques employed to characterize a sample surface at extremely high resolution. In Fig. 14 is shows the Bruker-Veeco Dimension Icon that was used to characterize the samples.

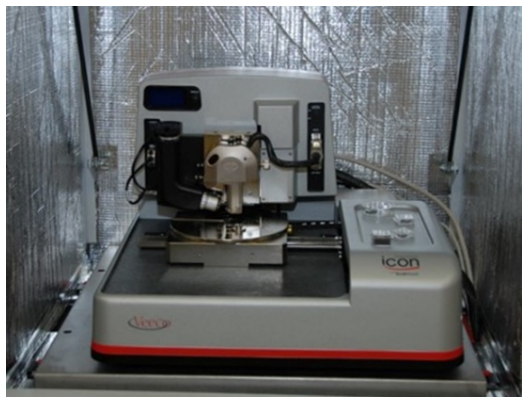


**Fig. 14 AFM Bruker-Veeco Dimension Icon.**

The working principle of AFM is based on the interaction between a sharp probe, a tip with a radius from 10 nm to 100 nm, placed on a cantilever, that is lead into proximity with the sample to be analysed. The interaction between tip and sample leads to a deformation of the cantilever. During the interaction between tip and sample two kinds of atomic forces are involved: at large distance the van der Waals force is the dominant one; at short distance the repulsive Pauli force is the dominant one. Probe and sample are moved relative to each other in a raster pattern, each line of the selected area is scanned forth (*trace*) and back (retrace), then the cantilever following the topography of the sample give back the morphology of the sample itself. A feedback loop controls the cantilever's deformation, controlling a piezoelectric actuator (Z scanner), which keeps either the tip at a constant distance from the surface or tip contact force constant (depending on the used scanning mode). The cantilever deformation is detected trough a laser beam, focused onto the backside of the probe, then reflected and collected through a photodetector, consisting of four different photodiodes. This setup is called beam deflection method, which measure the displacement with respect to the equilibrium beam position. In Fig. 15 a schematic representation of the AFM setup is reported.

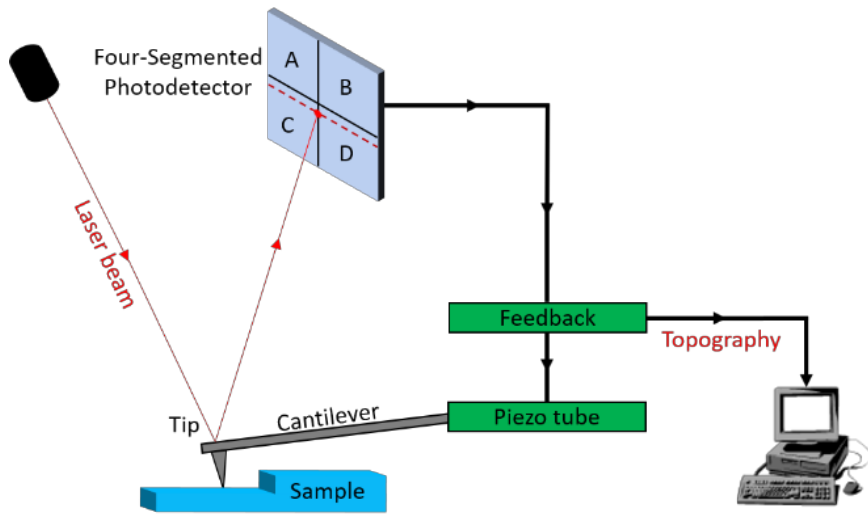


**Fig. 15 Schematic representation of e AFM setup.**

The angular displacement of the cantilever results in a variation of the laser spot position on the photodetector, corresponding in one

photodiode which collect more light then the other, generating an output signal. The deformation can be due to a vertical or lateral force ($F_v$ and $F_l$). The photodiode, measuring the intensity A, B, C and D of the reflected laser beam, can distinguish the signals of vertical and lateral forces as follows:

Vertical Signal: $$S_v = \frac{(A+D)-(B+C)}{(A+B+C+D)} \quad (2.1)$$

Lateral Signal: $$S_l = \frac{(A+B)-(C+D)}{(A+B+C+D)} \quad (2.2)$$

The difference between the sum of the signal of the top two elements and the two bottom elements provides the measure of the vertical deflection $S_v$ of the cantilever while the difference between the sum of the two left elements and the sum of the two right elements provides the measure of the torsion of the cantilever $S_L$. In Fig. 16 is sketched the cantilever deformation that correspond to the vertical and lateral deflection.

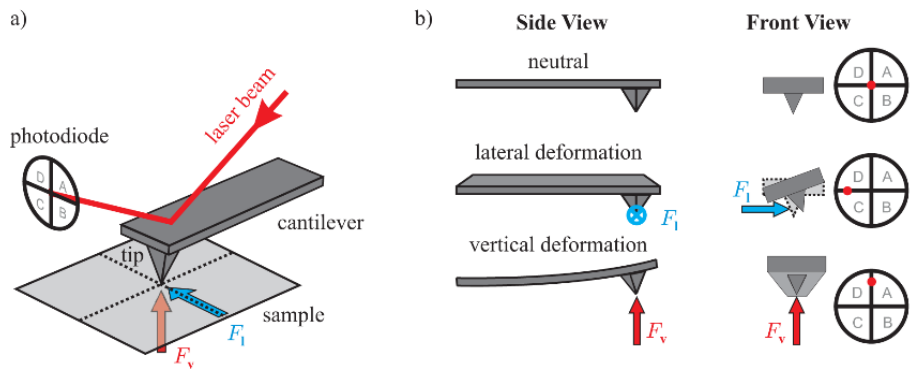


**Fig. 16 Vertical and lateral forces ($F_v$ and $F_l$) acting on the tip (a); deformation of the cantilever and corresponding deviation of the laser spot (b)** [22]**.**

The two principal operating modes for the AFM are: contact mode and tapping mode.

## *2.1.1 Contact Mode*

Contact mode is the basic and fundamental AFM mode and it is used to measure a series of surface properties, including conductive AFM and PFM. Extending the Z scanner, the probe approaches the surface of the sample. Once the tip is in contact with the sample the cantilever starts to

bend. When the cantilever deflection reaches the defined setpoint, that corresponds to a predetermin contact force, the extinction of the Z scanner stops. The scanning over the sample's surface causes the cantilever deflection to change. In this case the feedback element controls the Z scanner in a way that the force between sample and tip is kept constant to a chosen setpoint. This procedure provides the topography information which is visualized by a computer [22].

The interaction between tip and surface can be expressed by the Lennard-Jones potential that, as well known, is the result from the combination of the terms: an attractive interaction Van-der-Walls force and a repulsion interaction Pauli force (see Fig. 15). During the probe approach, the attractive Van-der-Waals interaction is dominant. At short distance the Pauli repulsion overcomes the attraction. In the contact mode the distance is $z \ll 1$ nm where the repulsive forces control the cantilever deformation. The steep trend of the potential guarantees a high vertical resolution [22].

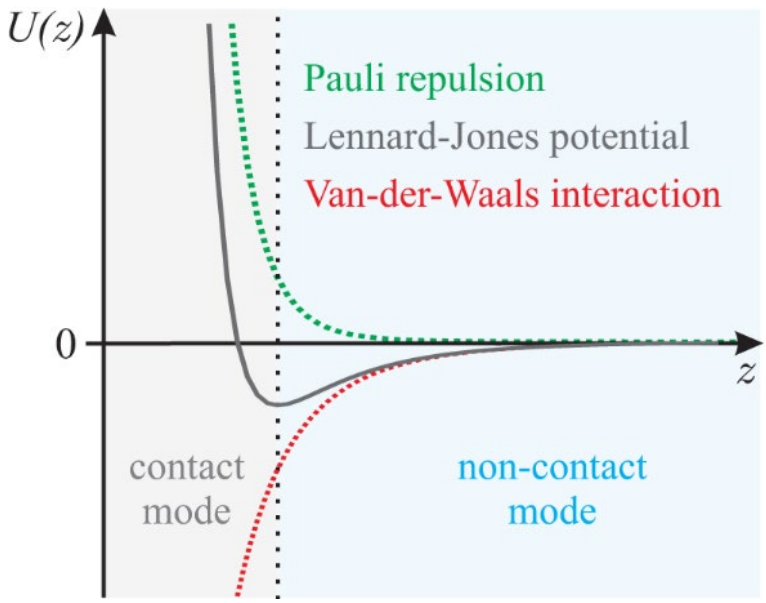


**Fig. 17 Lennard-Jones potential U(z) for two atoms with distance z** [22].

The contact force can be estimated performing the so-called *force plot* procedure. In order to perform this measurement, the Z scanner has to make, without any feedback, two different movements: first the probe approaches the surface and then retracts from it. In Fig. 18 a typical force curve is reported: the deflection of the cantilever is plotted as a function

of the of the position of the Z scanner. From the non-contact position, the probe goes down until it touches the surface. The cantilever is not bent, and there is no tip-sample contact and the beam is in its equilibrium position (blue line, segment 1), until the attractive forces, in proximity of the surface, pull down the tip. The tip starts to be in contact with the sample and the cantilever bends downwards, with a decrease in deflection (segment 2). Once in contact, the probe descends further producing an increasing of the contact force, and the cantilever bends upward resulting in an increase of the deflection (segment 3). When the Z scanner is moving in the reverse direction, the probe starts ascending, the force decreases, and the cantilever relaxes (red line, segment 4). Attractive capillary forces between tip and surface make the tip to hold on it, causing the cantilever to bend downward (segment 5). The deflection decreases further until the spring force of the cantilever overcomes the attractive forces (segment 6) at the pull-up point. The cantilever comes back to the non-contact position (segment 7).

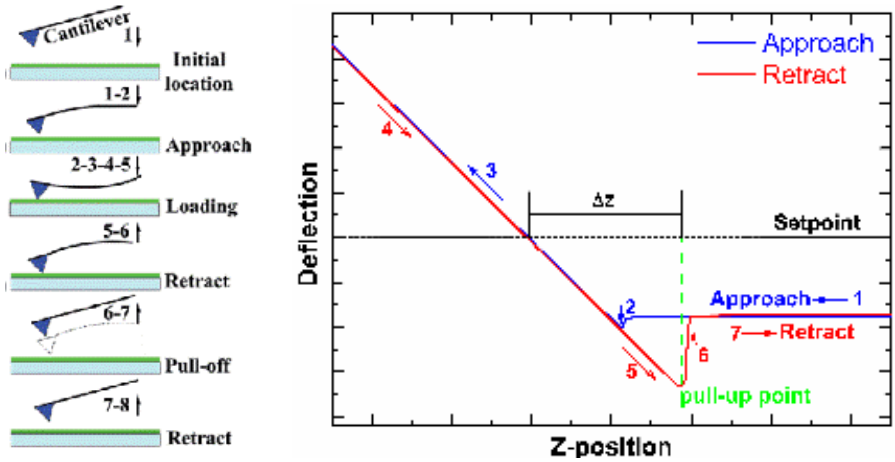


**Fig. 18 Typical force curve. The red line represents the response during the tip approaching while the blue line is the response during the retracting.**

The deflection setpoint determines the contact force. From the force curve it is possible to calculate the contact force maintained by the feedback loop during the measurement. The vertical deflection of the cantilever coincides to the Z scanner movement. If the cantilever spring constantan $k$ is known, using the Hooke's law it is possible to calculate the contact force:

$$F_{con} = k \cdot \Delta z \qquad (2.3)$$

where Δz is the distance covered by the Z scanner to bring the cantilever deflection from the setpoint to the pull-up point. Typical contact forces are in the range of $10^{-9}$ N.

In contact mode AFM there are high lateral forces between the tip and the surface that can damage the tip or the sample surface. To overcome this problem the tip can touch the sample's surface only for a short time using a so-called tapping mode AFM.

## *2.1.2 Tapping Mode*

Tapping mode AFM operates by scanning a tip attached to the end of an oscillating cantilever across the sample surface. The cantilever is oscillated at or slightly below its resonance frequency with an amplitude ranging typically from 20 nm to 100 nm. A typical response curve of a cantilever is shown in Fig. 19. When the tip is close to the surface, because of their interaction, the resonance shifts to lower frequencies and exhibits a drop-in amplitude. The tip lightly "taps" on the sample surface during scanning, contacting the surface at the bottom of its swing. The feedback loop maintains a constant oscillation amplitude by maintaining a constant RMS of the oscillation signal acquired by the split photodiode detector. The photodetector sends the signal to an internal lock-in amplifier (LIA), which yields a DC signal proportional to the amplitude of the cantilever

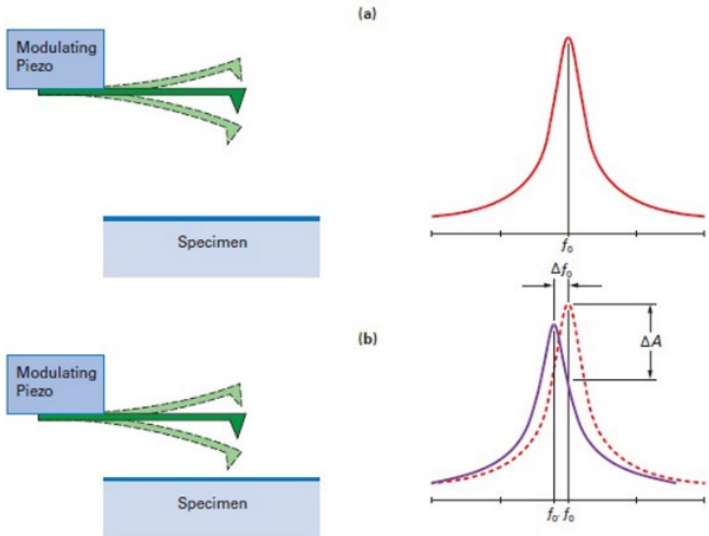


**Fig. 19 Resonance curve of a tapping mode cantilever above (a) and close to the surface (b)** [23]**.**

oscillation. To maintain constant the amplitude oscillation the feedback control drives a piezo-tube to adjust the vertical position of the cantilever. The vertical position of the scanner at each (x,y) data point is stored by the computer to form the topographic image of the sample surface. By maintaining a constant oscillation amplitude, a constant tip-sample interaction is maintained during imaging. A schematic representation of the tip oscillation, without feedback loop (a) and with feedback loop (b), for two different average tip-sample distance is reported in Fig. 20.

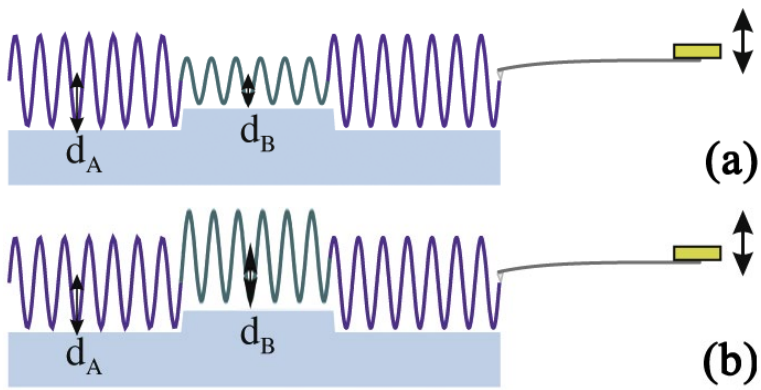


**Fig. 20 Tip oscillation without feedback loop (a) and with feedback loop (b) for two different average tip-sample distances $d_A$ and $d_B$. The oscillation remains sinusoidal also at reduced distances d** [24].

Fig. 21 shows the topography of a calibration grating with 10 μm pitch and 180 nm step height.

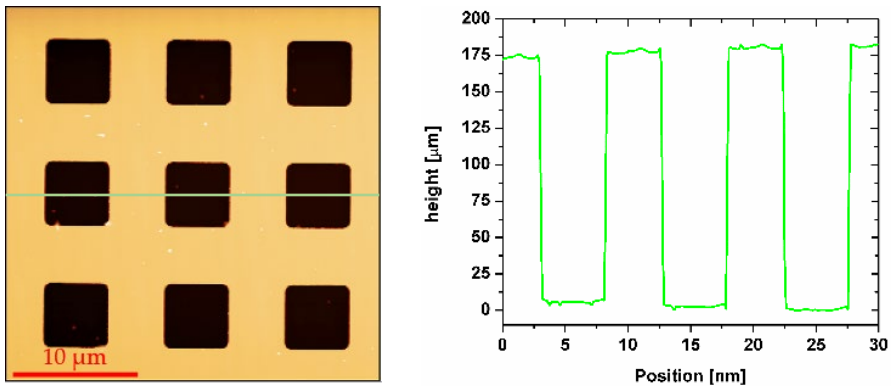


**Fig. 21 Topography of a calibration grating with 10 μm pitch and 180 nm step height(a) and heigt profile along the green line (b).**

It should be pointed out that, thanks to the LIA technique, the tapping mode guarantees a higher lateral resolution respect to the contact mode.

## 2.2 *Piezoresponse Force Microscopy (PFM)*

Piezoresponse Force Microscopy (PFM) is an AFM technique able to record the piezoelectric response of a sample. The technique allows to detect the piezoelectric amplitude and phase imaging with high resolution, down to 0.1 nm. The mechanisms contribution to the contrast in PFM imaging are still under debate in literature and can hardly be used for quantitative measurements. In this thesis PFM has been applied to quantitatively evaluate the piezoelectric coefficient of the different investigated materials.

### *2.2.1 History of PFM*

PFM was introduced to measure the local piezoelectric coefficient at the nanoscale as a non-destructive method. In the ideal case, the electromechanical response can be linked to the local piezoelectric response.

At the beginning of the 90s some research groups started to modify the AFM setup. To detect the polarization in ferroelectric samples they used a tip as movable electrode. In 1991 the Dransfeld's group [25] using a scanning tunnelling microscope (STM) measured the piezoelectric coefficient of a vinylidene fluoridetrifluoroethilene (VDF-TrFE) sample provided with a top gold electrode. One year later [26] they developed an AFM using the tip as top electrode for both polarizing and detecting polarization in VDF-TrFE.

Since then a great attention was focused on ferroelectric materials in view of data storage applications. PFM evolved with the combination of vertical and lateral PFM, and the area of research expanded over PZT thin films and different materials [27]. In order to have a proper interpretation of the PFM data a lot of groups started to study the process underlying PFM measurements. Among those, in 2006, Jungk et al. [28] developed a vectorial analysis of the PFM mechanism to detect the piezoresponse signal. In particular they pointed out how the presence of a background noise, coming from the experimental setup, is responsible of many irregularities in PFM measurements.

## 2.2.2 Operating Principle of PFM

PFM is based on the standard contact mode AFM setup, schematically sketched in Fig. 22. The imaging contrast for domains is based on the converse piezoelectric effect.

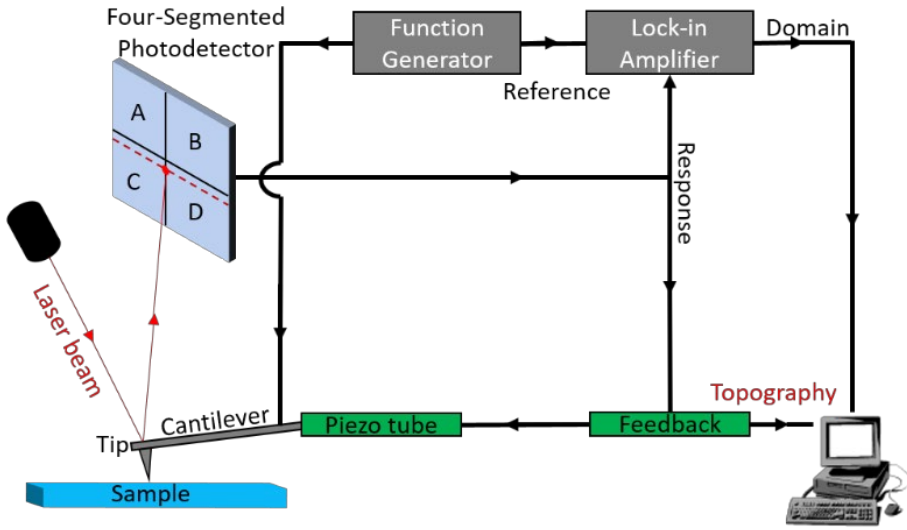


**Fig. 22 Schematic representation of the piezoresponse force microscopy (PFM).**

In addition to the standard AFM setup, an alternating voltage is applied between the mandatorily conductive tip and a back electrode behind the sample. The alternating voltage can also be applied to the back-electrode (BE) while grounding the tip. Such an interchange results only in a phase shift of $\pi$ of the lock-in output signal.

The modulation voltage generates an alternating field across the sample, which makes it to vibrate. The phase $\Theta$ of such a vibration depends on the polarization direction inside the sample. If the latter is in phase with the applied field, the vibration of the sample is in phase with respect to the modulation voltage ($\Theta = 0$). Conversely, for opposite mode it is out of phase ($\Theta = \pi$, see Fig. 23).

The BE, that is grounded, guarantees a well defined electric field distribution and thereby reproducible conditions for PFM imaging. The piezoelectric samples respond to the alternating electric field with a periodic deformation. Consequently, according to the piezoelectric

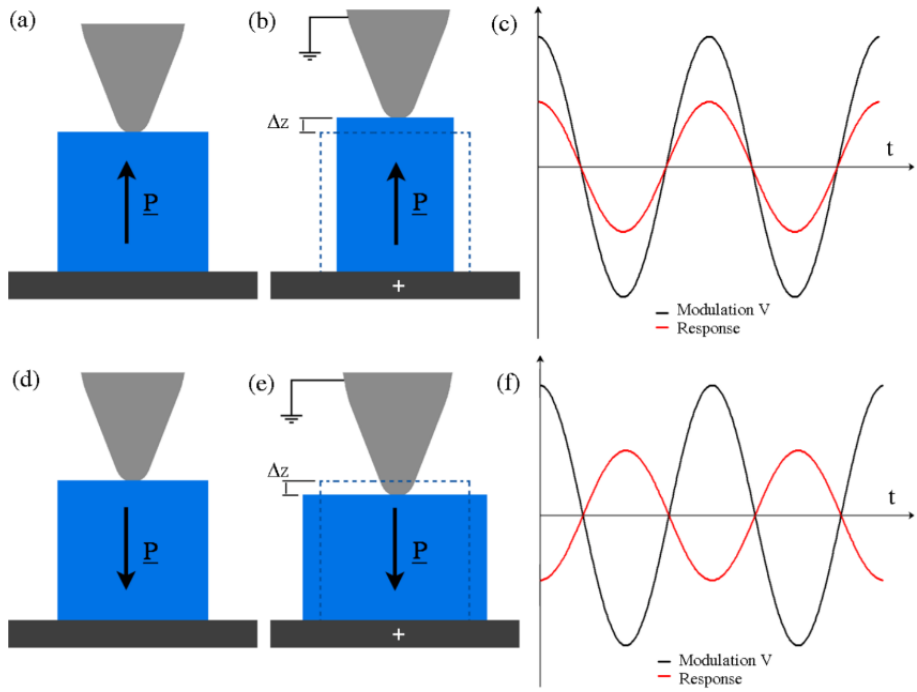


**Fig. 23 Phase shift in piezoresponse: for a upward polarization (a), the volume expand for an upward field (b) and the vibration is in phase with the excitation voltage (c). For a downward polarization domain (d), the volume contracts for upward field (e) and the vibration is out of phase with the modulation voltage (f)** [27].

coefficients the sample will be deformed and this deformation will be followed by the tip. The probe displacement, due to the deformation, is recorded via the photodiode. In order to separate the topography and piezoresponse signal, a lock-in amplifier (LIA), which also acts as a sharp band pass filter, is required. The LIA compares the response signal with the reference signal and amplifies only the frequency component that is equal to the reference signal. Since the reference signal and the voltage applied to the tip have the same frequencies, the expected piezoresponse is also at the same frequency. This allows measurements with a high signal-to-noise ratio even for small signals, like average displacements of just a few picometers (pm). Generally, the amplitude is set to values up to 10 V and the frequency from 10 kHz to 100 kHz. PFM can measure both out-of-plane and in-plane components of the piezoresponse [29], performing complementary measurements called vertical PFM (VPFM)

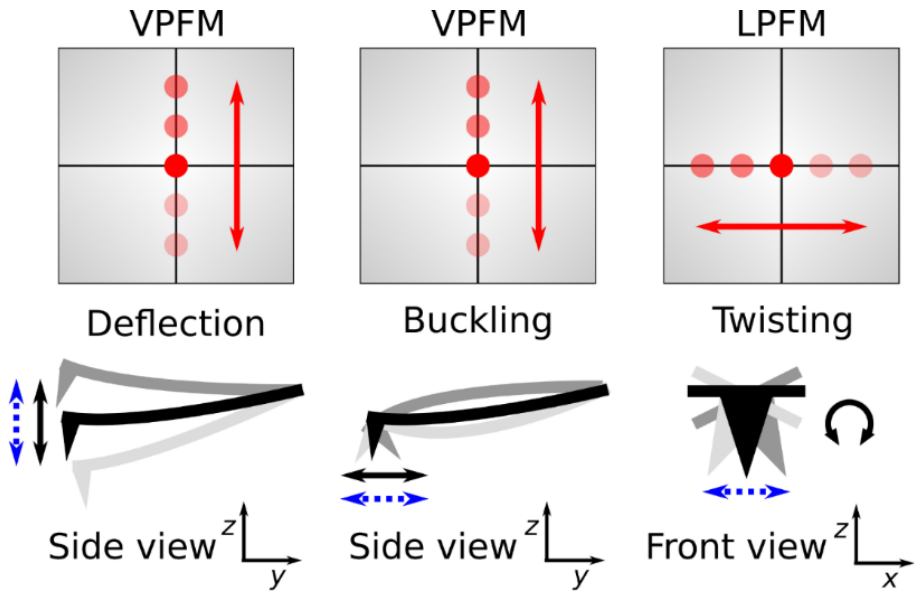


**Fig. 24 Possible movements of the cantilever due to forces acting on the tip. Flexural deflection (left), detected in VPFM, originates from an out-of-plane piezoresponse. Flexural buckling (centre), detected in VPFM, and lateral twisting (right), detected in LPFM, both originate from an in-plane piezoresponse. The double arrows in the upper part of the figure represent changes in the laser spot position on the photodiode. The solid double arrows in the lower part represent the cantilever motion, while the dashed double arrows represent the motion of the sample surface acting of the cantilever** [29].

and lateral PFM (LPFM). As showed in Fig. 24, VPFM detects vertical movements of the laser position on the photodiode, associated with the flexural deflection or buckling of the cantilever, while LPFM detects the lateral movements of the laser position, associated with the lateral twisting of the cantilever.

Flexural deflection is caused by an out-of-plane piezoresponse (deformations in the z direction), but flexural buckling is caused by an in-plane piezoresponse parallel to the cantilever axis (deformations in the y direction). Lateral twisting is caused by an in-planepiezoresponse perpendicular to the cantilever axis (deformations in the x direction).

### *2.2.3 Imaging of the Piezoelectric Domains*

Periodically poled lithium niobite (PPLN) is a very useful sample to demonstrate the relationship between polarization orientation and

piezoresponse, since it exhibits a simple 180° domain structure, as sketched in Fig. 25. Furthermore, in Fig. 25 are reported the corresponding vertical and lateral PFM signals.

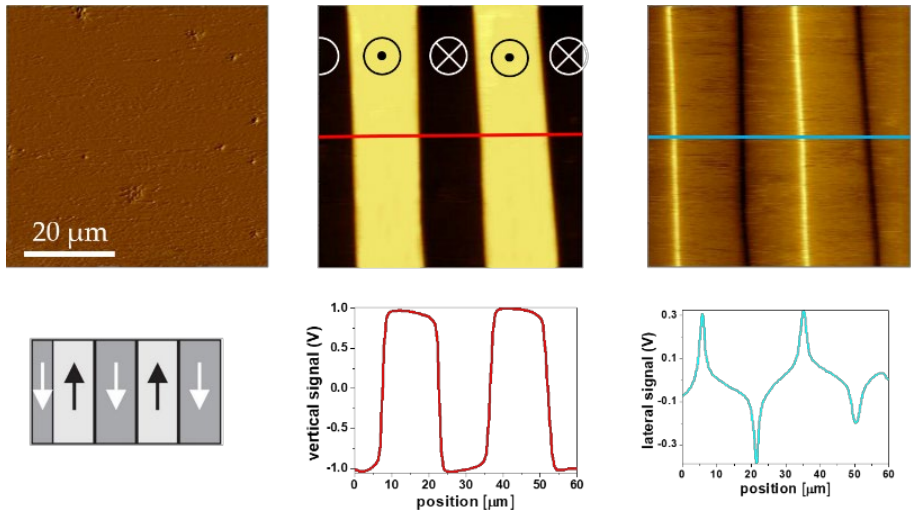


**Fig. 25 Morphology and domain structure of PPLN (a), vertical (b) and lateral (c) PFM signal domain image and the relative profile, respectively along the red and the blue line.**

The two 180° domains cause a 180° phase shift in the respective vertical piezoresponse. This results in a positive and negative DC signal from the LIA, respectively, that is visible as a contrast in the vertical PFM image (Fig. 25 (b)). Since for z-cut PPLN the polarization is always perpendicular to the sample surface, there is a lateral signal that which produces a peak-like structure at the domain boundaries, as can be seen in Fig. 25 (c) [30].

## *2.2.4 Quantification of the Piezoelectric Coefficient*

PFM is well used to detect the ferroelectric domain patterns with a high lateral resolution of about 10 nm and has also proven to be extremely sensitive as it allows measurement of local surface displacements in the sub-pm regime [31]. Nevertheless, there is still lack of an opportune procedure to determine the absolute values of the piezoelectric coefficient with high precision. In this thesis a procedure to quantitative evaluate the piezoelectric coefficient ($d_{33}$) is proposed and applied to a variety of samples. In the PFM measurements, thanks to the LIA, a periodic signal from a noisy environment can be extracted and rectified and comparing it with an external reference frequency a phase $\Theta$ can be attributed to the

signal. The LIA measurement can be presented either as two amplitudes ($X$, $Y$) or as magnitude and phase ($R$, $\Theta$). These two representation are connected by $X = R \sin \Theta$ and $Y = R \cos \Theta$ [31]. It has to be pointed out that the LIA determines ($X$, $Y$) electronically and calculate ($R$, $\Theta$) in a successive step. A useful way to understand the evaluation of the background is to use a $x$–$y$-representation on an oscilloscope of the $X$- and $Y$ -output LIA signals (see Fig. 26).

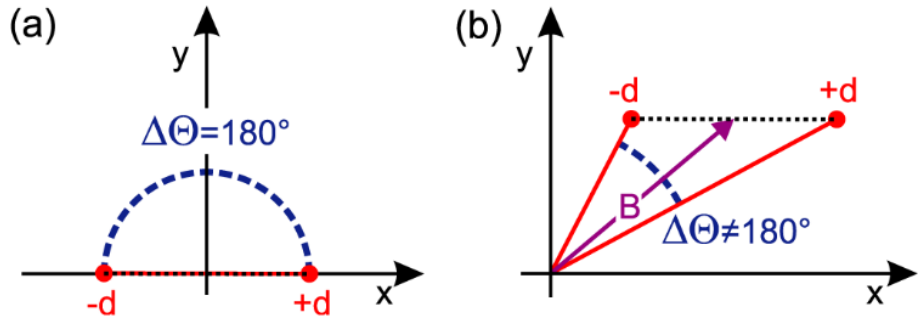


**Fig. 26 x/y-representation of the PFM signal obtained on a PPLN sample with piezoresponse d in the case of no background (a) and with background (b)** [31].

A PPLN sample, that is characterized by two-domain (↑↓) (see Fig. 25) with a piezoresponse $+d$ and $-d$, is used as test sample. The alternating voltage $V_{ac}$, applied to the tip, fixed the external reference frequency. When the output LIA signal is background free the magnitudes R on both domains are the same and their relative phase difference is $\Delta\Theta = 180°$, as sketched in Fig. 26 (a). When a background $\vec{B}$ is present the origin of the Cartesian coordinate system is shifted to a new position by the vector $\vec{B}$. The consequence is that the magnitude $R$ of the PFM signals on the two domains are no longer equal, and their phase difference $\Delta\Theta \neq 180°$ [31]. A simple way to overcome the background problem consists in recording the X-output signal of the LIA for PFM imaging. Since any contribution to the PFM signal caused by the piezoresponse from the PPLN must be either in phase or 180° out of phase with respect to the $V_{ac}$, any information in the $Y$-output must be either due to the background or to an electronic delay in the electronics of the system. The $X$-output signal of the LIA therefore contains the complete information of a PFM measurement.

The PFM technique gives us both the phase Θ and the magnitude R of the LIA output channels. The Θ output of the LIA, as said before, gives us only two values: 0° and 180°, even if the polarization vector is not oriented normal to the sample surface but at a certain angle $\phi$ (see Fig. 27 (a)), the Θ output of the LIA yields only these two values. The magnitude of the output *R* presents the displacement at the sample surface. The amplitude output X contains both the phase and the magnitude information. In the case of a background the Θ output can exhibit values different from 0° and 180°. In this case we need to estimate the background and subtract it from the PFM measurements [28]. Briefly, the procedure is based on the evaluation of the vertical PFM signal of the PPLN. If the VPFM signal of PPLN is symmetric respect to the vertical signal axis (see Fig. 25), the background is nought. Otherwise, the background signal is the mean value between the highest and the lowest value of the VPFM, for each applied voltage value.

In Fig. 27 the LIA output signals Θ, *R* and *X* are shown for a sample exhibiting seven domains with the polarization pointing into different directions. It can be seen that the combination of the Θ and *R* output signals yields the same information as the *X* output signal on its own.

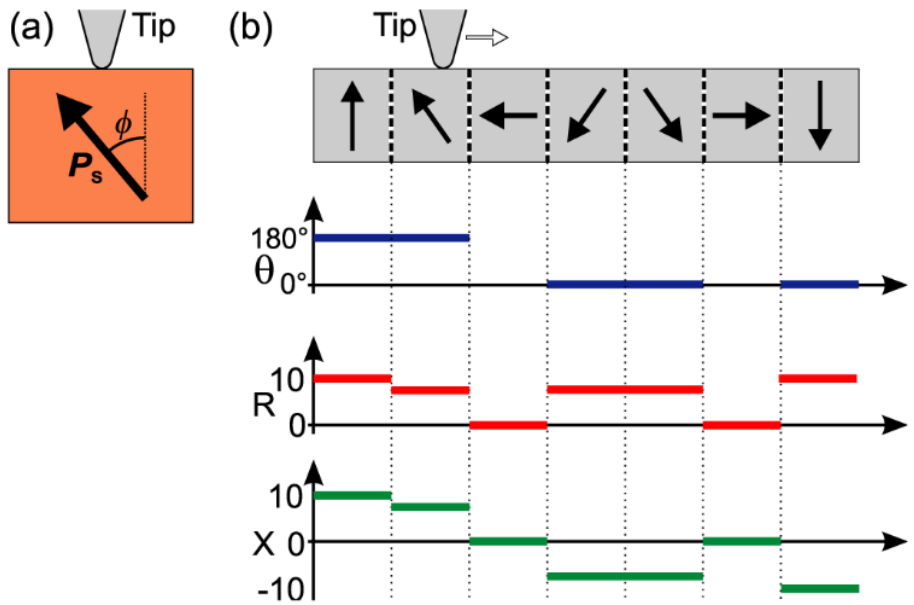


**Fig. 27 Sample with polarization vector oriented at the angle $\phi$ with respsct to the surface sample (a). Phase Θ, magnitude R and amplitude X of a sample with polarization vector pointing in seventh different directions** [31].

The deformation at the surface of the sample, Δz, due to the converse piezoelectric effect, is a linear function of the amplitude of the applied a.c. voltage $V_{ac}$:

$$\Delta z = d_{ij}\, V_{\mathrm{ac}} \tag{2.4}$$

in which $d_{ij}$ is the local relevant element of the third-rank piezoelectric tensor of the material [32]. The raw amplitude signal, measured using the segmented photodiode and LIA, is converted to a displacement amplitude by applying a calibration factor, which is obtained through the measurement of a calibration piezoelectric material. To this purpose a Bruker reference sample, consisting of a periodically poled lithium niobate (PPLN) specimen, with an effective piezoelectric coefficient $d_{33\_\mathrm{PPLN}} = 7.5$ pm/V, is employed. In the ideal case the amplitude of the measured piezoresponse $X$ depends linearly from $V_{ac}$:

$$X = \xi\, d_{33}\, V_{\mathrm{ac}} \tag{2.5}$$

in which $\xi$ is a calibration parameter, $d_{33}$ is the effective piezoelectric coefficient measured via PFM and $V_{ac}$ is the amplitude alternating voltage. In order to estimate $\xi$ the background correction technique, briefly outlined above and discussed in in more detailed in [31], is applied. At first, six areas at the same point of the specimen were scanned, with a scan area (60×7.5) μm² in size with (256×32) measured points with an applied alternating voltage at a fixed frequency ($10\ \mathrm{kHz} \leq f \leq 100\ \mathrm{kHz}$, typically 15 kHz) and increasing amplitude from 0 V to 10V with a step of 2V. The amplitude of the PFM signal ($X$) resulting from the average of the (256×32) measurement points over the scanning area is plotted as a function of $V_{ac}$ (see Fig. 28). Then, through a linear fitting of the straight line the slope of the calibration sample ($m_{\mathrm{PPLN}}$) is evaluated and the calibration factor is estimated:

$$\xi = m_{\mathrm{PPLN}}/d_{33\_\mathrm{PPLN}} \tag{2.6}$$

where $d_{33\_\mathrm{PPLN}}$ is the known piezoelectric coefficient of the PPLN. Finally, the response of the sample under test is measured and using $\xi$ we convert the $X$ signal (expressed in V) into the vertical displacement ($A_{piezo}$):

$$A_{piezo} = X/\xi \tag{2.7}$$

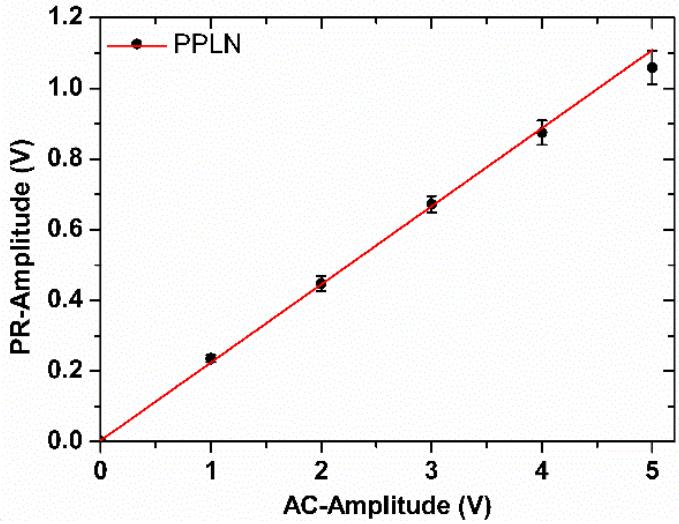


**Fig. 28 Measured amplitude of the piezoresponse of PPLN with respect to the applied voltage $V_{ac}$.**

Using the well-known equation of the converse piezoelectric effect ($A_{piezo} = d_{33} \cdot V_{ac}$) evaluating the slope (m) of the $A_{piezo}$ in function of the $V_{ac}$, through a linear fitting, we estimated the $d_{33}$:

$$d_{33} = m = \frac{A_{piezo}}{V_{ac}} \tag{2.8}$$

After completing the PFM characterization of the desired sample, the reference PPLN was tested again in order to verify that the system was still calibrated. For this purpose, we repeated the measurement of the piezoelectric signal ($X$) of the reference PPLN sample and we compared the new value with the corresponding value previously measured (before the characterization of the desired sample). If the difference between the two calibration piezoelectric signals for each value of the applied voltage $V_{ac}$is less than 20%, the measurement of the sample under test is considered reliable. Differences larger than 20% may occur due to several instabilities, including tip degradation, drift of the electronic apparatus or of the thermal and noise conditions.

The proposed protocol can be then schematically summarized as follows:

- First a calibration measurement of the PPLN sample, with known $d_{33}$, is conducted in the amplitude voltage range at which the sample will be tested;

- Then the sample under test is measured in the selected amplitude voltage range;
- The PPLN is measured again and the new VPFM signals, for each value of the applied voltage $V_{ac}$, are compared with the corresponding values measured during the first calibration cycle;
- If the difference between the two piezoelectric calibration signals is less than 20%, the measurement of the sample under test is considered reliable;
- Then the calibration factor $\xi$ is evaluated, averaging over the two calibration measurements, and the $d_{33}$ value of the sample under test is calculated, according to equation (2.8).

# CHAPTER III

## ZINC OXIDE NANOSTRUCTURES

# Chapter III

# Zinc Oxide Nanostructures

Zinc oxide (ZnO) nanostructures, such as ZnO nanorods (NRs) and nanowalls (NWs), have attracted a great interest to fabricate devices for energy harvesting, thanks to their capability to convert the ambient vibrational energy into electrical energy. In this chapter, after a brief description of the synthesis method of ZnO NRs and NWs, structural, crystalline, chemical electronic and piezoelectric properties of the materials are analysed.

## *3.1 Introduction*

Several methods have been developed to grow ZnO nanostructures [33–38]. Among them chemical bath deposition (CBD) [35–37] has received much attention, as it ensures a high deposition rate on a wide variety of substrates; moreover, it is facile, cost-effective and easy to scale-up. The properties of ZnO nanostructures are strongly depending on their size, shape, and morphology [36,39–41]. In particular, the characterization of the piezoelectric properties of ZnO nanostructures having different morphology is a fundamental step towards the production and performance optimization of nano-generators and nano-actuators.

## *3.2 Growth of ZnO Nanorods*

In this thesis the ZnO NRs are grown using a facile CBD, developed by Chandraiaghari during his PhD thesis [19,42]. All chemicals are of reagent grade and used as obtained from the manufacturer: zinc acetate dihydrate ($Zn(CH_3COO)_2{\cdot}2H_2O$, Sigma-Aldrich, ≥ 98%), zinc nitrate hexahydrate ($Zn(NO_3)_2{\cdot}6H_2O$, Acros Organics, 98%), hexamethylenetetramine (HMTA, $C_6H_{12}N_4$, Fisher Scientific, ≥99%), isopropanol ($(CH_3)_2CHOH$, Sigma-Aldrich, ACS reagent, ≥ 99%), acetone ($CH_3COCH_3$, Acros Organics, ≥ 99%) and deionized water (DI) with a resistivity of 18 MΩ·cm.

The substrates, generally glass or polyethylene terephthalate (PET) covered with a thin film of indium tin oxide (ITO), are first cleaned in acetone and then in isopropanol. Subsequently they are dried in an oven at 70 °C for 10 min. Prior to growth, a seed layer is deposited onto the

cleaned substrates by the dip-coating method. A seed solution is prepared by dissolving 5 mM of zinc acetate dehydrate in to 40 ml of isopropanol using magnetic stirring at room temperature. The substrates were then dip-coated in the seed solution and underwent thermal annealing inside a muffle furnace at 300 °C for 30 min, in the case of a PET/ITO as a substrate the thermal annealing is inside a furnace at 150 °C for 30 min. This process resulted in substrates coated uniformly with ZnO seed particles having an average diameter of 20 nm (see Fig. 29) [42].

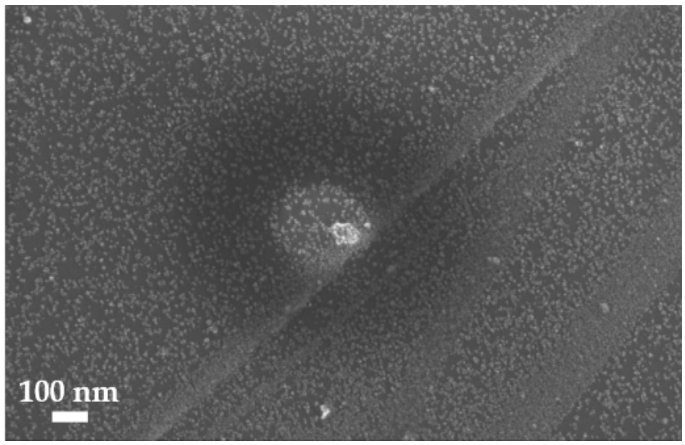


**Fig. 29 FE-SEM micrograph of the ZnO seed particles.**

ZnO nanostructures are grown on the seeded substrates using CBD [32]. Briefly, an aqueous growth solution is prepared by dissolving 20 mM equimolar ratios of zinc nitrate hexahydrate and hexamine together in 100 ml of DI water. The seeded substrate was then vertically immersed into the growth solution. The suspension was placed on a hot plate (Heidolph MR-Hei Standard) under static conditions for 4.5 h. During the reaction, the beaker was sealed with an Al foil and the solution temperature was fixed at 60 °C using an automatic electronic temperature controller (EKT Hei-Con). After Zn nitrate dissociation, $Zn^{2+}$ ion forms a complex with six water molecules $[Zn(H_2O)_6]^{2+}$. The essential equations for the description of ZnO-NRs growth is the following [37]:

$$[Zn(H_2O)]^{2+} + H_2O \leftrightarrow [Zn(H_2O)_5OH]^{+} + H_3O^{+} \quad (3.1)$$

$$[Zn(H_2O)_5OH]^{+} + H_2O \leftrightarrow Zn(OH)_{2(s)} + H_3O^{+} + 4H_2O \quad (3.2)$$

$$Zn(OH)_{2(s)} \leftrightarrow ZnO_{(s)} + H_2O \quad (3.3)$$

while hydrolysis equilibria of $Zn^{2+}_{(aq)}$ move to the right for the simultaneous protonation of the HMTA itself or of the ammonia groups coming from HMTA decomposition:

$$(CH_2)_6N_4 + H_3O^+ \leftrightarrow [(CH_2)_6N_4]H^+ + H_2O \quad (3.4)$$

or

$$(CH_2)_6N_4 + 6H_2O \leftrightarrow 6HCHO + 4NH_3 \quad (3.5)$$

$$NH_3 + H_3O^+ \leftrightarrow NH_4^+ + H_2O \quad (3.6)$$

Afterwards the growth reaction, the substrate is removed from the solution, rinsed in DI water and dried in oven at 120 °C for 30 min. At the end of the process ZnO-NRs were grown. A FE-SEM cross-section of the produced ZnO-NRs is showed in Fig. 30.

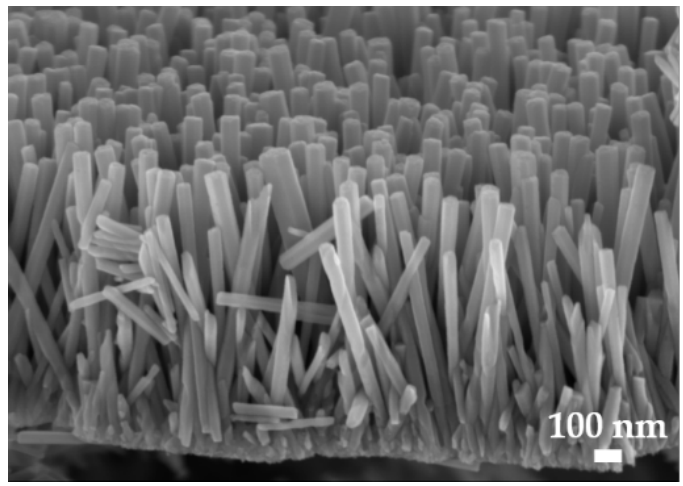


**Fig. 30 FE-SEM cross section of the produced ZnO-NRs.**

## *3.3 Techniques used for the characterization of ZnO Nanostuctures*

The morphology of the ZnO-NRs is investigated through FE-SEM (Zeiss Auriga) and AFM (Bruker-Veeco Dimension Icon). In particular, FE-SEM images are used to estimate the lateral size of the ZnO-NRs, while the height is assessed through tapping mode AFM scan [32].

Chemical composition analysis is performed through Energy Dispersive X-ray Analysis (EDX) using the FE-SEM, Zeiss Auriga,

equipped with a Bruker Quantax EDX capable of an energy resolution of 123 eV at Mn K$\alpha$.

The structural characterization and phase identification of the synthesized ZnO-NRs are performed, in collaboration with Department of Earth Sciences, Sapienza University of Rome, through Powder X-ray Diffraction (P-XRD) in transmission mode on a focusing beam Bruker AXS D8 Advance diffractometer using CuK$\alpha$ radiation ($\lambda = 0.15418$ nm), operating at 40 kV and 40 mA. Data are collected in a 2θ angular range extending from 20° to 145° with a step size 0.022° and 1 s counting time. The instrument is fitted with incident-beam Göbel mirrors and a position sensitive detector VÅntec. Samples are prepared as capillaries loaded with the Zno-NRs in powder form obtained upon removal from the growth substrate by using bath sonication. A preliminary check is done using a Siemens D5000, operating in reflection mode, using CuK$\alpha$ radiation ($\lambda = 0.15418\,nm$), operating at 40 kV and 40 mA. Analyses pointed out the presence of ZnO under the hexagonal wurtzite modification. Structural refinements are performed by the Rietveld method using TOPAS v.4.2 (Bruker AXS 2009) software. Details of the refinement procedure can be found in [35].

X-ray Photoelectron Spectroscopy (XPS) is performed, in collaboration with CNR-ISMN, Monterotondo, Rome, using a monochromatized spectrometer Escalab 250Xi (Thermo Fisher Scientific, UK) equipped with a six-channeltron detection system for spectroscopy. The samples are loaded in an ultra-high vacuum (UHV) chamber, using the Al K$\alpha$ X-ray source set to the diameter of 900 μm, the analyzer at a constant pass energy of 20 eV, and the standard mode of electromagnetic input lenses (about 1 mm in diameter). The acquired data were processed by the Avantage v.5 software (Thermo Fisher Scientific, UK).

The photoluminescence (PL) spectra are recorded, in collaboration with ENEA, Frascati, Italy, at room temperature by using the 266 nm line of a Nd:YAG pulsed laser (Thomson DIVA) as the exciting source, having 10 ns pulse length and 20 Hz repetition rate. Further details on the PL experimental setup and procedure can be found in [35]. Spectra are repeated on the same sample 16 times and averaged to get proper statistics. The measurements are performed at different power levels of the exciting laser in the range 700-1300 W/m$^2$, in order to discriminate

between linear and non-linear behaviour of the defect-related and band edge PL emissions. Since the ZnO-NRs are grown on a substrate, the spectra of bare ITO/glass is also acquired for reference, and used to correct the spectra of the ZnO-NRs sample.

PFM measurements are performed using a commercial Bruker-Veeco Dimension Icon AFM, equipped with the piezoelectric module under the following conditions: silicon cantilever (Bruker) with 115-135 μm length, nominal spring constant of 5 N/m, Co-Cr coated tip with electrical resistivity of 0.01-0.025 Ω·cm, tip curvature radius ~35 nm and nominal resonance frequency of 150 kHz. In order to measure the piezoresponse of the samples, an a.c. voltage is applied to the tip, with amplitude varying from 4 mV to 5 V at a fixed frequency of 17 kHz. Scan rate was 0.5 Hz and the scan area is (600×600) $nm^2$. Three different areas are scanned, and the measured data were averaged. All measurements are performed in an insulating chamber to avoid acoustic excitation [32].

### *3.3.1 Morphological and Chemical Characterizations*

The morphology of ZnO-NRs as observed through FE-SEM, is shown in Fig. 31 (a)-(b). As expected it is obtained a vertical alignment with a very narrow size distribution of the nanostructures with estimated diameter of $(\sim 42 \pm 5)$ nm. This value is estimated by averaging the diameters of ten different NRs, evaluated using a commercial image processing software (ImageJ ©).

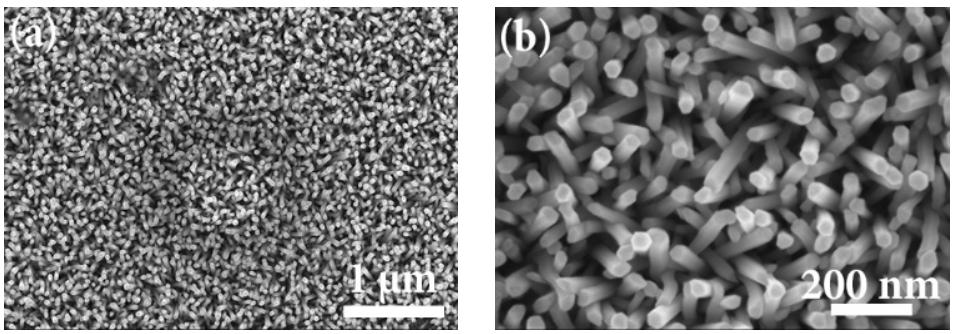


**Fig. 31 FE-SEM micrographs of ZnO-NRs at low magnification (25 kX) (a), and at high magnification (100 kX) (b)** [32]**.**

The EDX analysis (Fig. 32(a), (b)) shows an excess of Zn, and a few small peaks originated by the ITO/Glass substrate. The excess of Zn implies a non-stoichiometric Zn/O ratio. The compositional Zn map,

reported in Fig. 32(a), shows a homogenous distribution of Zn over the ZnO-NRs structures. Mapping the topography of the ZnO-NRs trough the AFM, using the tapping mode (see Fig. 33(a)), is possible to estimate the height differences of the nanostructures, resulted in values of ($\sim 150 \pm 80$) nm as deduced from the reported signal profiles, averaged along the scanned area (see Fig. 33(b)).

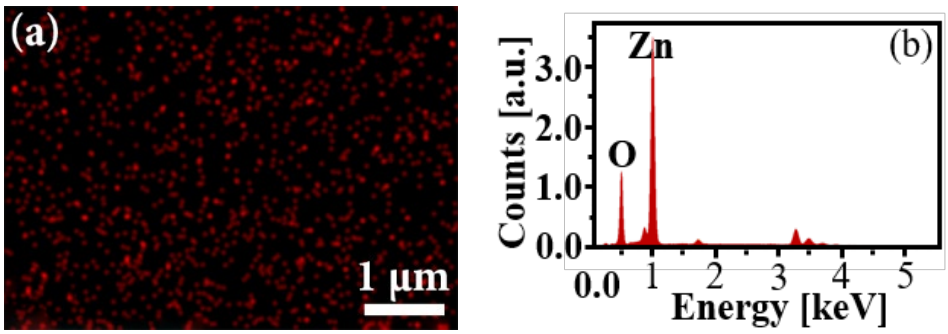


**Fig. 32 EDX elemental Zn mapping (a) and EDX spectra (b) of ZnO-NRs** [32].

The uncertainty on the height differences is due to the error stemming from the convolution of the real morphology and the tip shape, resulting in a curvature radius of the tip comparable with the diameter of the nanostructures under analysis. We note that the height of the NRs, estimated from the SEM image reported in Fig. 30, is $\sim 800 - 900\ nm$ and the AFM measurements represent a qualitative indication only of the height differences of the structures.

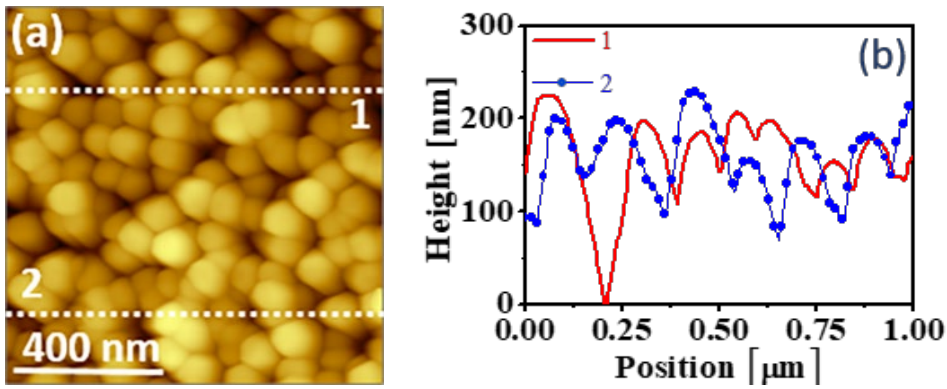


**Fig. 33 AFM topography in tapping mode (a) and the correspond height profile along the lines 1 and 2 for ZnO-NRs (b)** [32].

### 3.3.2 Structural Analysis

The crystallinity of the ZnO-NRs powder was evaluated by XRD analysis. In Fig. 34(a) is reported the pattern of the P-XRD. The sharp and intense peaks, which are observed, indicate the highly crystalline nature of the produced ZnO nanostructures. XRD data collected directly on the ITO-grown ZnO NRs (see Fig. 34(b)) indicate a single strong peak at $2\vartheta_{NRs} = 34.48°$ arising from the (002) planes of the wurtzite hexagonal modification of ZnO (JCPDS 36-1451). This fact testifies the preferential growth of the ZnO NRs perpendicularly to the substrate, as confirmed also by the FE-SEM images shown in Fig. 31(b) [43].

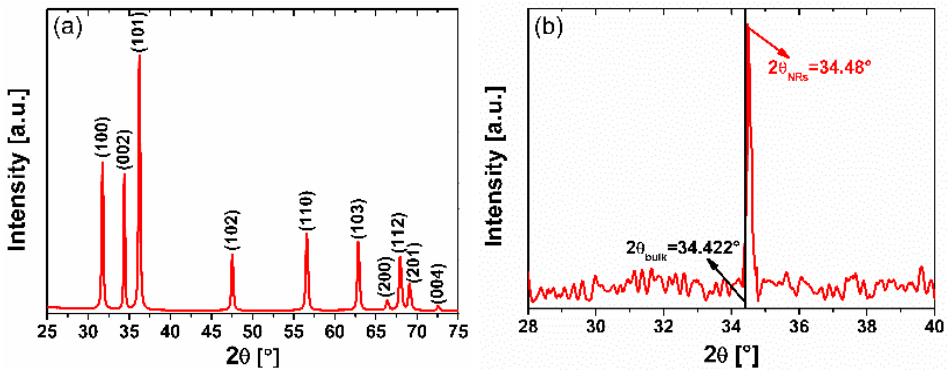


**Fig. 34 X-ray diffraction (XRD) pattern acquired on ZnO-NRs powder (a) and directly on the ITO/Glass substrate** [32]**.**

The produced ZnO-NRs are characterized by cell parameters and bond distances very similar to those reported for other nanorods samples [35]. In particular, the cell volume of 47.6318(3) $Å^3$ is higher than the one reported for bulk ZnO [44]. This behaviour agrees with that reported for other simple oxides, whose cell parameters and volume of the bulk material are smaller than those of micro- and nano-structured equivalents [45–47]. The <Zn-O> bond distance is of 1.978 Å and the $ZnO_4$ tetrahedron is slightly distorted as a result of 3 x 1.9753(3) Å and 1 x 1.9864(12) Å bond distances. ZnO-NRs has an $\varepsilon_0$ micro-strain (lattice strain), defined as $\beta_i = 4\varepsilon_0 \tan\theta$, $\beta_i$ being the peak integral width, of 0.0376(5).

### 3.3.3 Chemical Composition

The surface chemical composition of ZnO-NRs has been analysed by XPS. In the samples, Zinc is present in the Zn(+2) chemical state, which is evident from the binding-energy (BE) value of the Zn $2p_{3/2}$ peak at 1021.4 eV (Fig. 35(a)) and from the Auger Zn LMM peak position at a

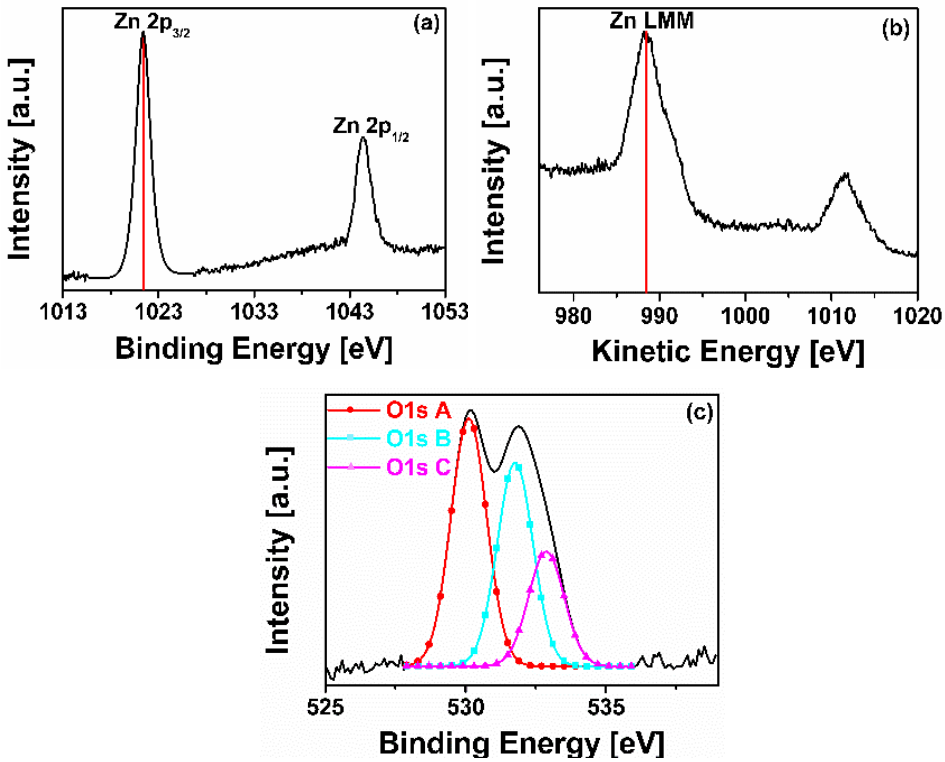


**Fig. 35 XPS Zn 2p (a), O1s (c) spectra and Auger Zn LMM spectra (b) of ZnO-NRs** [32].

kinetic energy (KE) of ~988.5 eV (Fig. 35(b)) [48,49]. In addition, the values of the modified Auger parameter $\alpha \approx 2009.9$ eV correspond to the Zn(+2) chemical state [48,50]. The spectra of Zn 2p and Zn LMM regions are shown in Fig. 35(a) and (b), respectively. The O1s spectra, shown in Fig. 35(c), consists of three components indicated as O1sA, O1sB and O1sC. The first component is attributed to $O^{2-}$ ions in the wurtzite structure of ZnO, whereas the second one is attributed to the loosely bound oxygen on the surface, such as in adsorbed hydroxyl groups -OH and/or -CO3 radicals [48,51]. The third components at BE ≈ 533 eV is due to the water molecules absorbed on the sample surface. XPS quantification was done by using Shirley background subtraction and a standard set of Scofield sensitivity factors. The surface contaminants (C and N) were not included in this quantification. The obtained results are summarized in Table 1.

The O1s spectra including the peak fitting are presented in Fig. 35 (c). To better understand the chemical composition, the ratio of Zn to O was computed for the component of oxide O 1s A. In the case of Zn/O > 1, the

**Table 1 XPS Elemental quantification.**

| Sample | Peak | BE (eV) | Atomic % | Chemical State |
|---|---|---|---|---|
| ZnO-NRs | O1s A | 530.1 | 28.5 | ZnO |
| | O1s B | 531.8 | 23.4 | $OH^-$ |
| | O1s C | 532.9 | 13.2 | $H_2O$ |
| | $Zn2p_{3/2}$ | 1021.4 | 34.9 | ZnO |

lack of oxygen is an indicator of a higher number of defects in zinc oxide. For ZnO-NRs, the Zn/O ratio was equal to 1.2. This result is in good agreement with the results of EDX and PL measurements (shown in the next paragraph), confirming an excess of Zn in ZnO-NRs.

### *3.3.4 Photoluminescence Properties*

Photoluminescence spectra have been studied in order to investigate the presence of defects. The results obtained for the excitation laser power of 1300 W/m² are reported in Fig. 36.

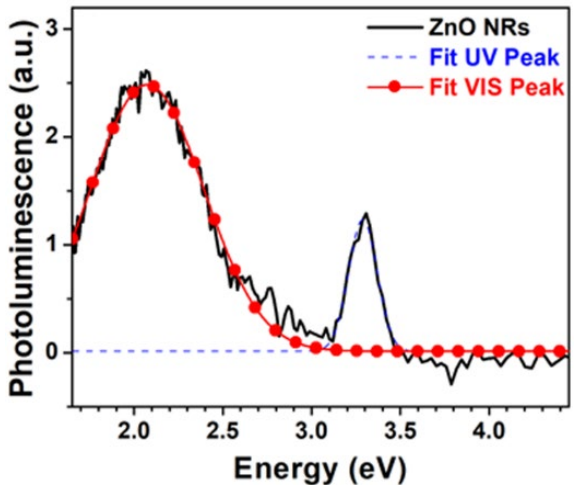


**Fig. 36 Photoluminescence spectra of ZnO-NRs. Continuous line represents experimental data corrected for substrate contribution; dashed and dotted line represents Gaussian best fitting results. The spectrum was taken at 1300 W/m² excitation power** [32].

The spectrum has been corrected by taking into account the effect of the substrates, and then it is fitted to multiple Gaussian peaks to identify the UV and VIS components, as shown in Fig. 36. The obtained best fit results is reported in Table 2, which shows also the values of the calculated UV/VIS ratio.

**Table 2 Best fit results of the ZnO-NRs PL spectra reported in Fig. 36. The UV/VIS ratio is calculated from the amplitude values of the Gaussian peaks.**

| Parameter | ZnO-NRs | |
|---|---|---|
| | UV | VIS |
| Energy (eV) | 3.289±0.005 | 2.075±0.008 |
| Width (meV) | 80±5 | 330±10 |
| Amplit. (a.u.) | 12500±700 | 24500±700 |
| UV/VIS | 0.51±0.08 | |

Actually, the UV/VIS emission intensity ratio is usually taken as an indicator of crystal quality [52,53], independently on the precise identification of the involved defects and their distribution in the nanostructures.

From Fig. 36, we observe that the PL spectra of ZnO-NRs is characterized by an ultraviolet (UV) peak at ~3.3 eV, corresponding to the band edge emission, and by a visible (VIS) bands centred at ~ 2.1 eV. It is important to underline that the different energy values of the centre of the VIS bands originate from different kinds of defects [52–58].

The effect of varying the excitation powers on PL emission was essentially to enhance the UV/VIS intensity ratio for increasing powers, as reported in Fig. 37.

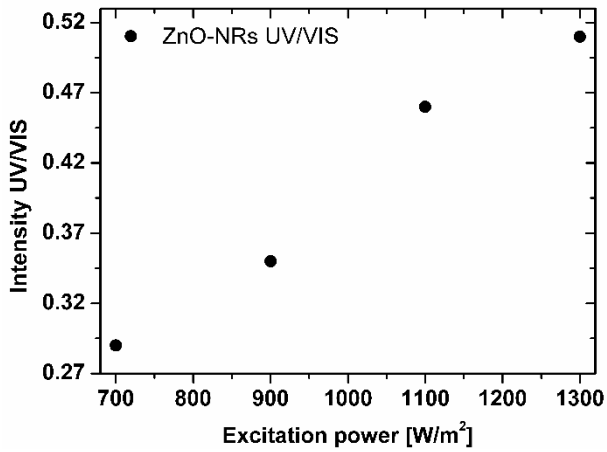


**Fig. 37 ZnO-NRs UV/VIS intensity ratio vs the PL excitation power.**

Such an effect was consistent with the present interpretation of the UV and VIS peaks, since defect-related PL emissions typically tend to saturate at lower excitation powers than band-gap emission (i.e. "intrinsic"

emission), since they are limited by the concentration of the defects involved in the recombination. PL peak positions did not show any evident dependence on PL excitation power, out of the measurement's uncertainty.

From Table 2, it can be observed that the ZnO-NRs has a UV peak centred at 3.289 eV, whereas the VIS band is located at ~ 2.1 eV (yellow band). The identification of the defects responsible for this band is still debated in the current literature, allowing for multiple and controversial interpretations.

Nevertheless, a possible explanation of the yellow band observed in our sample can be attributed to the presence of oxygen vacancies. A similar interpretation has been recently proposed in the literature [53] for vertically aligned ZnO-NRs. In that work, the authors reported the observation of a PL band around 2 eV, whose intensity decreased after oxygen ions irradiation, and increased with the diameter of the nanorods, indicating that the defects responsible for that emission involve oxygen vacancies which were localized in the nanorods, within a region up to ~ 100 nm from their outermost surface.

Therefore, since the average diameter of ZnO-NRs is ~ $(42 \pm 5)$ nm, we can assume that, according to [53], the oxygen vacancies associated to the yellow PL band are distributed in the whole volume of the nanostructures, resulting in an overall oxygen deficient oxide material. This assumption is supported by XPS and EDX analysis, which indicate a Zn/O ratio >1.

### *3.3.5 Piezoelectric Properties*

The piezoelectric coefficient $d_{33}$ of the nanostructured thin films of ZnO-NRs was estimated through PFM. The measurements are performed using the procedure described in Chapter 2. In particular, in our test setup, we applied an a.c. voltage to the sample under test, through the tip, and the bottom electrode was grounded. A comparison of the topographic map and of the vertical (out-of-plane) PMF-signal map is shown in Fig. 38. The good correlation between morphology and PFM signals suggests that the vertical piezoelectric domains are well localized in each single nanorod.

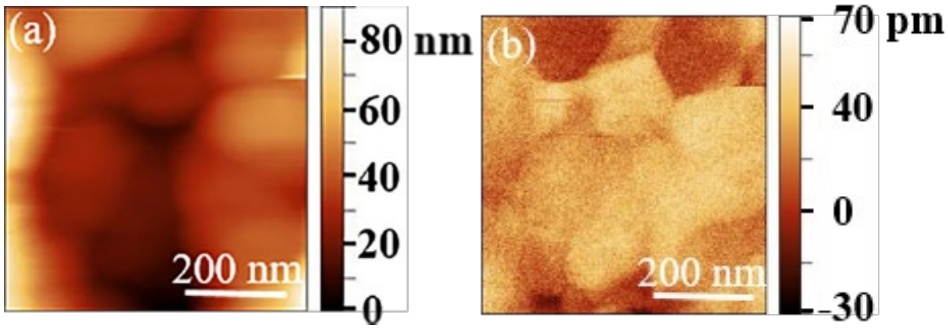


**Fig. 38 Typical scanning piezoresponse measurements showing the morphology (a) and the vertical (out-of-plane) PFM signal for ZnO-NRs (b)** [32].

In order to evaluate the average piezoelectric properties of the samples, PFM measurements were performed over 3 different areas on each sample. Each area has a scanning size of (600×600) nm², which guarantees a good average signal, as confirmed by the small standard deviations obtained (Fig. 39).

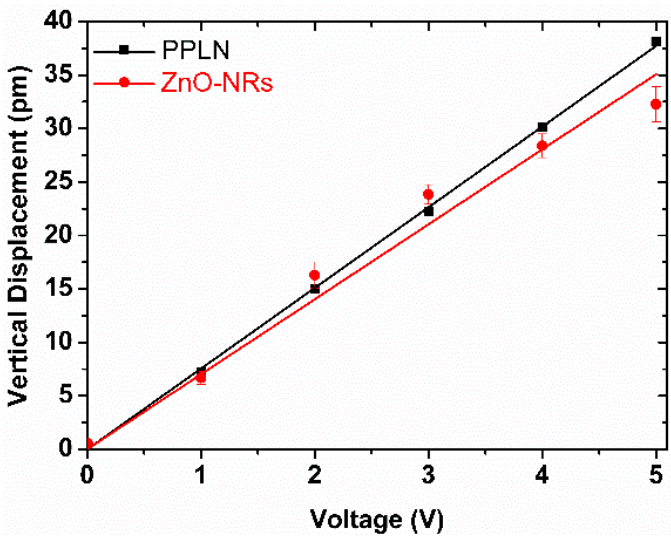


**Fig. 39 Measured ZnO-NRs piezoresponse amplitude with respect to the applied voltage $V_{ac}$. It is also reported the PPLN piezoresponse amplitude, used for calibration.**

As predicted by the theory, the displacement response increases linearly with the driving voltage amplitude. The effective $d_{33}$ was obtained using a linear fit of the amplitude of the average vertical displacement versus the amplitude of the driving voltage, as reported in Fig. 39. Using the calibration procedure described in Chapter II, section

2.2.4, the measured piezoelectric coefficient results: $d_{33} = (7.01 \pm 0.33)$ pm/V (see Fig. 39).

## *3.4 Growth of ZnO Nanowalls*

The procedure and all the chemicals that are used to produce the ZnO nanowalls (ZnO-NWs) are the same used to produce the ZnO-NRs [32]. The only difference is the substrate, that in this case is an aluminium foil (Al-foil ~25 μm thick) purchased from Sigma-Aldrich. When using the Al-foil as a substrate, the thermal annealing made during the seed deposition is made inside a muffle furnace at 300 °C for 30 min. The result of the seeding process is the same as that obtained for the ZnO-NRs (see Fig. 29). The main difference in the growth process of the ZnO-NWs is the position of the seeded Al-foil in the growth solution. Infact, in this case, the substrate is horizontally suspended upside-down into the growth solution.

### *3.4.1 Morphological and Chemical Characterizations*

The morphology of ZnO-NWs, observed through FE-SEM, is shown in Fig. 40 (a)-(b).

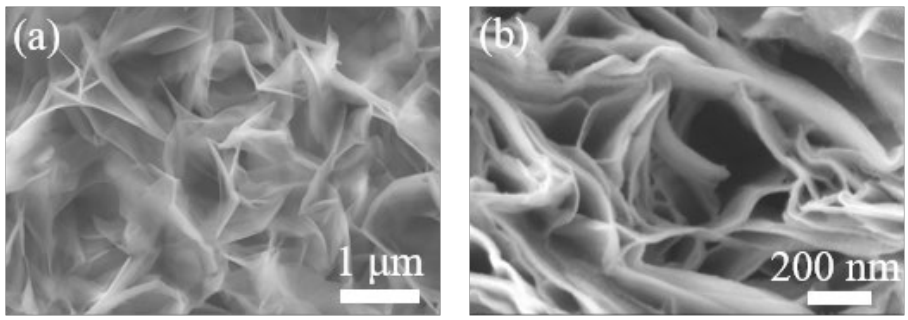


**Fig. 40 FE-SEM micrographs of ZnO-NWs at low magnification (50 kX) (a), and at high magnification (200 kX) (b)** [32]**.**

ZnO-NWs are characterized by thin walls with very sharp edges. The thickness and the lateral size are evaluated from the FE-SEM images as $(\sim 38 \pm 28)$ nm and $(\sim 950 \pm 370)$ nm, respectively. These values are estimated by averaging the thickness and the lateral size of ten different NWs, evaluated using a commercial image processing software (ImageJ ©). The EDX analysis of ZnO-NWs (Fig. 41(a), (b)), shows equally intense O and Zn peaks, together with the peak produced by the Al substrate.

Moreover, we observe a slight excess of oxygen, leading to a non-stoichiometric Zn/O ratio. The Zn compositional map, reported in Fig. 41(a), shows a homogenous distribution of Zn over the NWs.

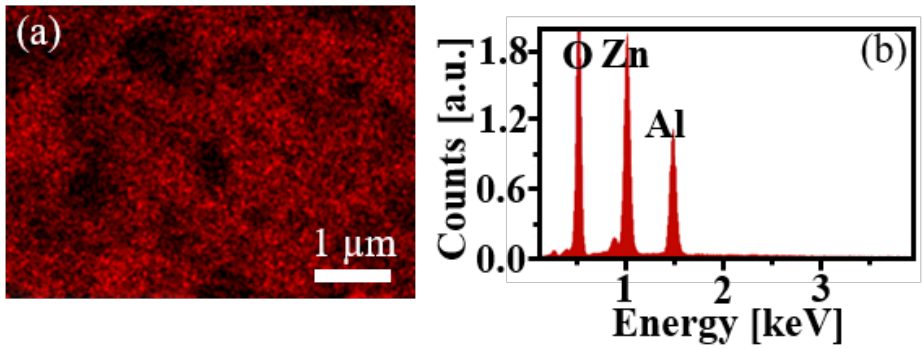


**Fig. 41 EDX elemental Zn mapping (a) and EDX spectra (b) of ZnO-NWs** [32].

The height measurements, performed through AFM in tapping mode (see Fig. 42), resulted in (~890 ± 510) nm, as deduced from the reported signal profiles, averaged along the scanned area (see Fig. 42(b)).

As previously said for the ZnO-NRs, these measurements represent a qualitative indication of the height of the structures, due to the error stemming from the convolution of the real morphology and the tip shape. Nevertheless, it is possible to estimate the aspect ratio of the ZnO-NWs (i.e. height over wall thickness): ~23.

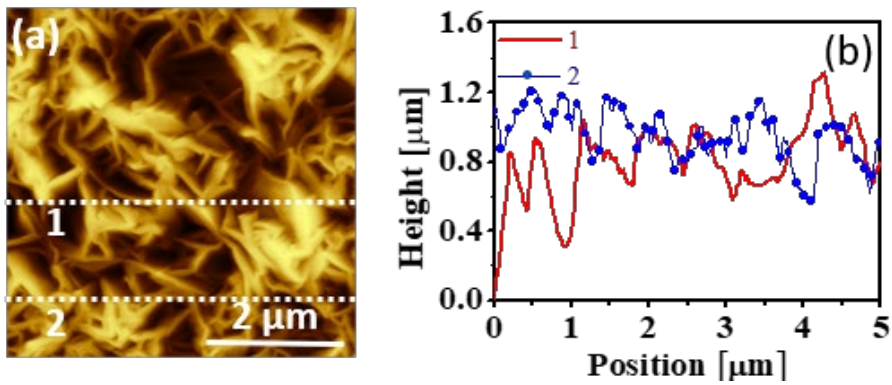


**Fig. 42 AFM topography in tapping mode (a) and the correspond height profile along the lines 1 and 2 for ZnO-NWs (b)** [32].

## *3.4.2 Structural Analysis*

The crystallinity of the ZnO-NWs powder was evaluated by XRD analysis. In Fig. 43 is reported the pattern of the P-XRD.

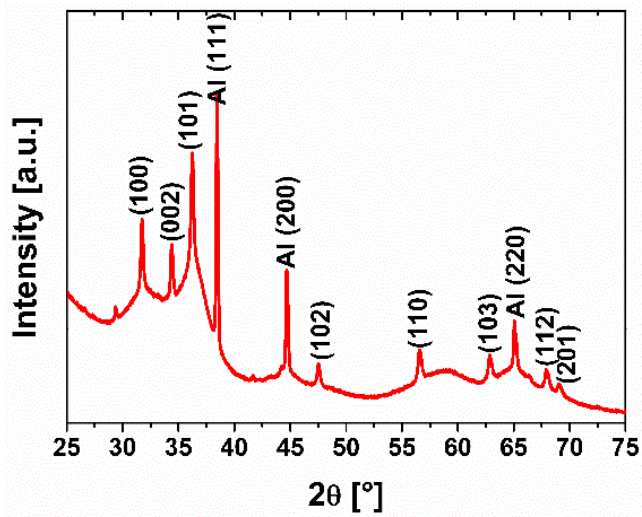


**Fig. 43 X-ray diffraction (XRD) pattern acquired on ZnO-NRs powder** [32].

The sharp and intense peaks, which are observed, indicate the highly crystalline nature of the NWs. However, the spectrum contains some peaks referable to Al, used as the growth substrate, and a strong broad band centred around 21.7° which arises from the glass capillary. Furthermore, an anomalous spread of some peaks is observed at the base of the pattern. We suppose that such an anomalous behaviour can be ascribed to the presence of high defectivity, which is further investigated using photoluminescence and discussed in the subsequent section. The P-XRD spectrum of ZnO-NWs is characterized by a significantly broadened peak shape that was impossible to properly fit even applying the ellipsoid-model of Katerinopoulou et al. [59], describing the diffraction-vector dependent broadening of diffraction maxima. This is clearly due to extended defectivity of the material. This fact is confirmed by a unit cell volume of 47.565(8) $Å^3$ smaller than that found in bulk ZnO (47.598(7) $Å^3$). In particular, Kaurova et al. [60] indicated that the occurrence of O-vacancies is coupled to a marked reduction of the cell parameters. Moreover, we investigated the possible symmetry reduction from $P6_3/mc$, which is typical of stoichiometric zincite, to $P3$, which has been observed in O-defective samples [60]. No Bragg reflection at ca. 17.2° 2θ was observed, attributed to the symmetry-violating 001 peak by those authors, indicating that the correct space group for ZnO-NWs is $P6_3/mc$. Coherently, the $\varepsilon_0$ micro-strain was 0.0901(15) significantly higher than that of ZnO-NRs. Due to the imperfect peak shape fit, bond distances

were not refined [61]. The hypothesis of a significant defectivity of ZnO-NWs is further supported by PL measurements, as discussed in the following.

### *3.4.3 Chemical Composition*

The surface chemical composition of ZnO-NWs has been analysed by XPS. In the samples, like for the ZnO-NRs, Zinc is present in the Zn(+2) chemical state, which is evident from the binding-energy (BE) value of the Zn $2p_{3/2}$ peak at 1021.5 eV (Fig. 44(a)) and from the Auger Zn LMM peak position at a kinetic energy (KE) of ~987.2 eV (Fig. 44(b)) [48,49]. In addition, the values of the modified Auger parameter $\alpha \approx 2008.7$ eV correspond to the Zn(+2) chemical state [48,50]. Furthermore, the presence of Al, in the chemical state $Al_2O_3$, has been evidenced from the binding-energy (BE) value of the Al 2p peak at 74.0 eV Fig. 44 (c). The presence of the Al at the surface is related to the Al-foil used as a substrate to grow the ZnO-NWs. The O1s spectra, shown in Fig. 44(d), consists of three components indicated as O1sA, O1sB and O1sC. The first component is attributed to $O^{2-}$ ions in the wurtzite structure of ZnO, the second one is attributed to the loosely bound oxygen on the surface, such as in adsorbed hydroxyl groups -OH and/or -CO3 radicals [48,51], whereas the third one is attributed to the O bound to Al. Like for the ZnO-NRs, the XPS quantification was done by using Shirley background subtraction and a standard set of Scofield sensitivity factors. The surface contaminants (C and N) were not included in this quantification. The obtained results are reported in Table 3.

**Table 3 XPS Elemental quantification for ZnO-NWs.**

| Sample | Peak | BE (eV) | Atomic % | Chemical State |
|---|---|---|---|---|
| ZnO-NWs | O1s A | 530.5 | 30.1 | ZnO |
| | O1s B | 532.1 | 30.2 | $OH^-$ |
| | O1s C | 531.3 | 6.0 | $Al_2O_3$ |
| | $Zn2p_{3/2}$ | 1021.5 | 24.4 | ZnO |
| | Al2p | 74.0 | 9.3 | $Al_2O_3$ |

In order to better understand the differences between the ZnO-NRs and the ZnO-NWs, the ratio of Zn to O was calculated for the component

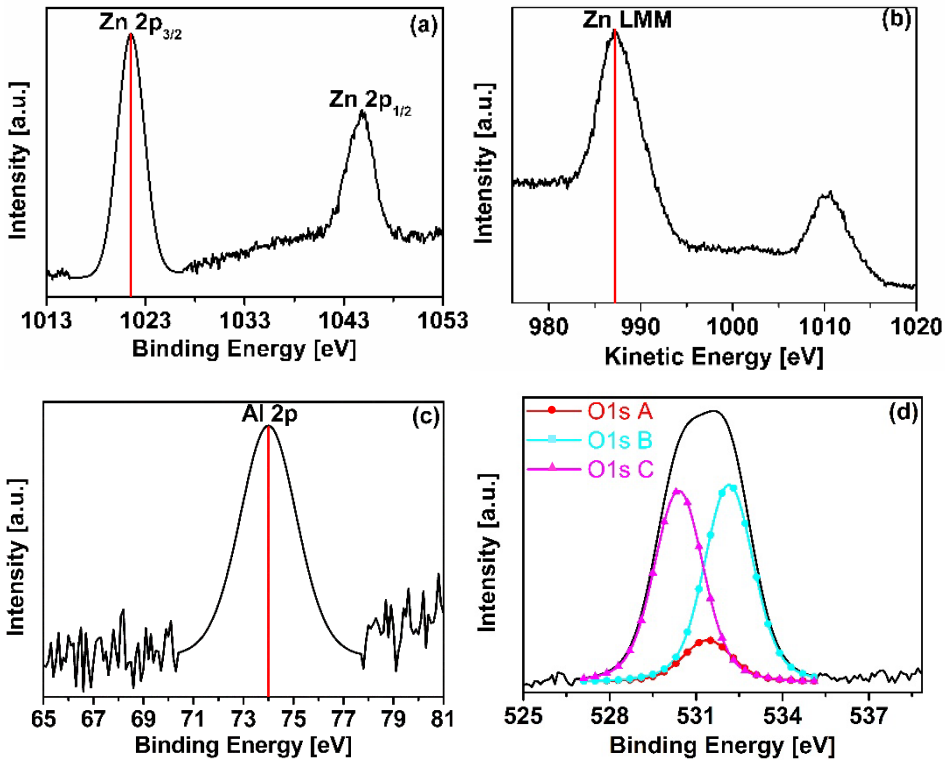


**Fig. 44 XPS Zn 2p (a), Al 2p (c), O1s (d) spectra and Auger Zn LMM spectra (b) of ZnO-NWs** [32].

of oxide O 1s A. As said, in the case of Zn/O > 1, the lack of oxygen is an indicator of a higher number of defects in zinc oxide. In the case of the ZnO-NWs the Zn/O ratio was equal 0.81. This result is in good agreement with the results of EDX and PL measurements (shown in the next paragraph), confirming an excess of O in the ZnO-NWs.

### *3.4.4 Photoluminescence Properties*

In order to investigate the presence of defect on the ZnO-NWs, like for the ZnO-NRs, the PL spectrum was studied (see Fig. 45). The excitation laser power is 1300 W/m$^2$. Similarly for the ZnO-NRs, the spectra have been corrected by taking into account the effect of the substrates, and then they are fitted to multiple Gaussian peaks to identify the UV and VIS components (see Fig. 45).

In Table 4 is reported the best fit results and the UV/VIS ratio, that, as said, it is an indicator of crystal quality. As it can be observed from the Table 4 the UV/VIS ratio for the ZnO-NWs is lower than for the ZnO-NRs,

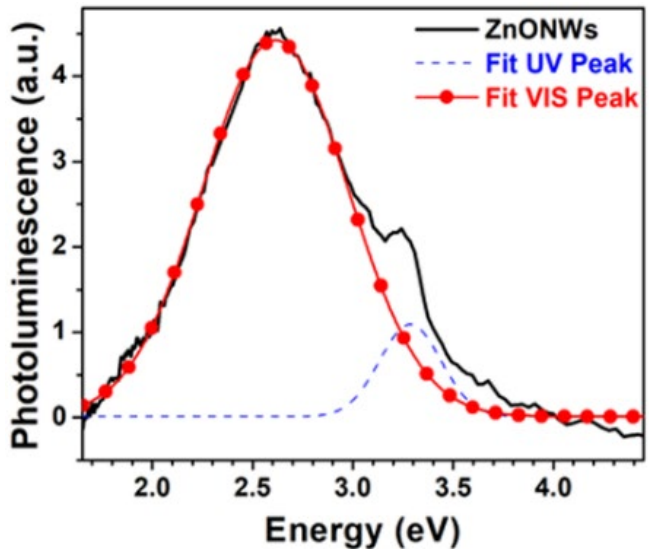


**Fig. 45 Photoluminescence spectra of ZnO-NWs** [32].

confirming the indications gained from XRD results, which suggested that the ZnO-NWs are more defective than the ZnO-NRs. The PL spectrum of the ZnO-NWs is characterized by an UV peak at ~3.3 eV, like for the ZnO-NRs, corresponding to the band edge emission, whereas the VIS band peak is located at 2.6 eV (green band), indicating the presence of different kinds of defects respect to the ZnO-NRs. As observed for the ZnO-NRs the effect of varying the excitation powers on PL emission was to enhance the UV/VIS intensity ratio for increasing powers, as reported in Fig. 46. Similarly, to the ZnO-NRs the UV/VIS intensity ratio increase indicates that the lower energy emission is due to defects, which is known to saturate at lower excitation powers than band-gap emission.

**Table 4 Best fit results of the ZnO-NWs PL spectra.**

| Parameter | ZnO-NWs | |
|---|---|---|
| | UV | VIS |
| Energy (eV) | 3.286±0.008 | 2.613±0.004 |
| Width (meV) | 154±8 | 362±4 |
| Amplit. (a.u.) | 10800±500 | 44100±300 |
| UV/VIS | 0.24±0.01 | |

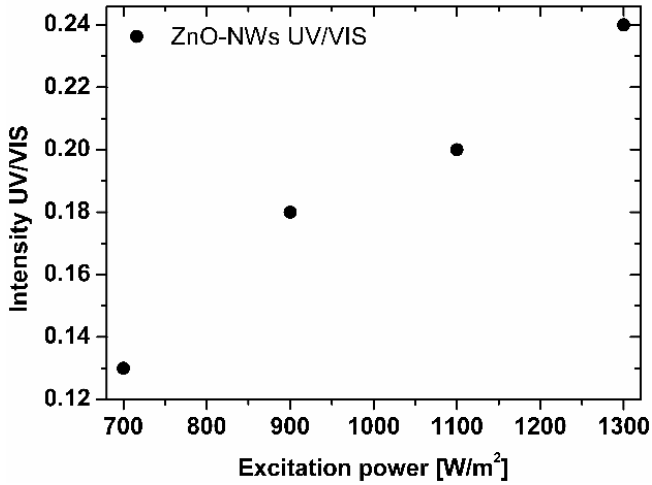


**Fig. 46 ZnO-NRs UV/VIS intensity ratio vs the PL excitation power.**

A possible explanation of the green band around 2.5 eV can be linked to zinc vacancies located at the $(10\bar{1}0)$ non-polar surfaces of ZnO-NWs [58]. Although the cited work does not refer specifically to ZnO nano-walls, its conclusions apply to nanostructures having different morphologies (i.e. ZnO polycrystalline nanostructured films) provided that there were $(10\bar{1}0)$ non-polar surfaces exposed. In the case of the ZnO-NWs, the morphology showed by AFM is consistent with the presence of unipolar $(10\bar{1}0)$ facets exposed upwards on the sample face, from which the luminescence signal is collected. XRD measurements support the presence of $10\bar{1}0$ facets. The presence of zinc vacancies in the ZnO-NWs sample is also supported by XPS and EDX analysis, which indicate a Zn/O ratio <1.

## *3.4.5 Piezoelectric Properties*

The piezoelectric coefficient $d_{33}$ of the ZnO-NWs was estimated through PFM. The measurements are performed using the procedure described in Chapter 2 and the a.c. voltage is applied to the sample through the tip and the bottom electrode was grounded. The morphological map and the vertical (out-of-plane) PMF-signal map is shown in Fig. 47.

As observed from Fig. 47 the morphology and PFM signals of the ZnO-NWs are poorly correlated. This is due to the fact that ZnO-NWs are not

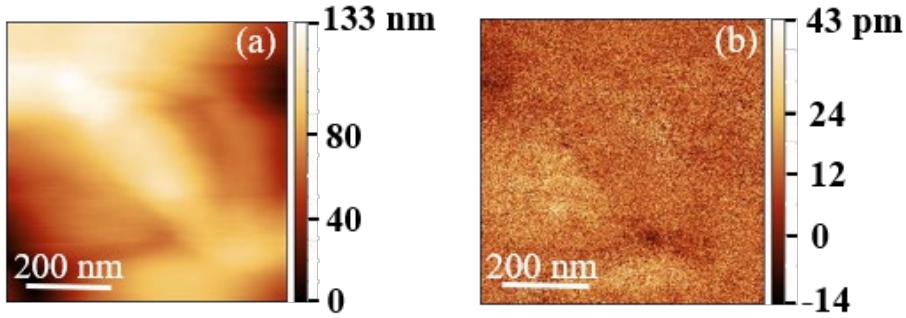


**Fig. 47 Scanning piezoresponse measurements showing the morphology (a) and the vertical (out-of-plane) PFM signal for ZnO-NWs (b)** [32].

so well vertically oriented with respect to the substrate like the ZnO-NRs, so that the vertical piezoelectric domains are poorly localized. In order to evaluate the average piezoelectric properties of the samples, PFM measurements were performed over 3 different areas on each sample. Each area has a scanning size of (600×600) nm$^2$. As reported in Fig. 48 the effective $d_{33}$ was obtained using a linear fit of the amplitude of the average vertical displacement versus the $V_{ac}$. Using the calibration procedure described in Chapter II, section 2.2.4, the measured piezoelectric coefficient is: $d_{33} = (2.63 \pm 0.49)$ pm/V, that is lower than the value obtained for the ZnO-NRs. This is due to the different morphology, structural properties and defectiveness of the two nanostructures. The obtained results both for ZnO-NRs and ZnO-NWs are in line with data reported in previous studies [61,62], which however are focused on a local characterization of the piezoresponse of each single domain or nanostructure. The proposed PFM characterization of both nanostructures (ZnO-NRs and ZnO-NWs) instead provides a quantitative estimation of the average value of $d_{33}$, which is representative of the piezoresponse of the nanostructure's material at nanoscale.

Comparing the piezoelectric coefficient of the two nanostructures: (7.01±0.33) pm/V for ZnO-NRs and (2.63±0.49) pm/V for ZnO-NWs, it is evident that the ZnO-NRs show the better piezoelectric response. It is believed that this behaviour is due to a better crystallinity, more uniform orientation and a less defectiveness of the ZnO-NRs if compared to the ZnO-NWs, confirmed by XRD spectra and by PL measurements. The position of the centre of the visible PL-band in ZnO-NWs indicated that such defectiveness can be attributed to the presence of zinc vacancies.

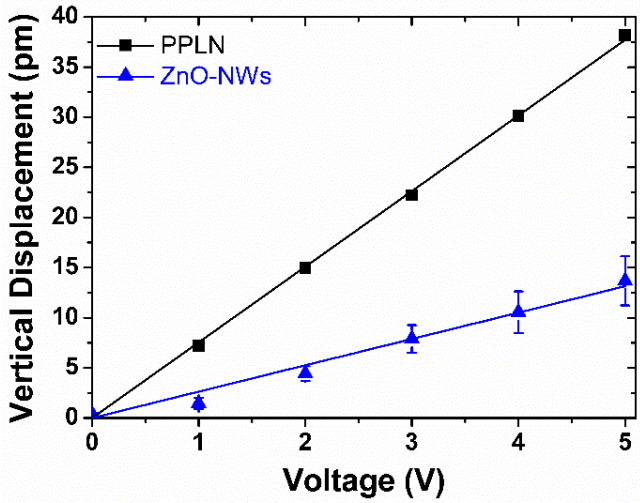


**Fig. 48 Measured amplitude of the piezoresponse with respect to the applied voltage $V_{ac}$.**

# *CHAPTER IV*

## *POLYMER NANOCOMPOSITES*

# Chapter IV

# Polymer Nanocomposites

Novel polymer-based piezoelectric nanocomposites with enhanced electromechanical properties open new opportunities to the development of low-cost wearable energy harvesters and sensors. One of the most interesting flexible piezoelectric organic material is polyvinylidene fluoride (PVDF). This polymer can be obtained in three main polymorphs, namely $\alpha$, $\beta$, and $\gamma$ forms and its piezoelectric properties mainly depend on its $\beta$-phase. The increase of the $\beta$-phase content is considered as an essential prerequisite to the enhancement the piezoelectric response of PVDF polymer thin films. In this chapter the piezoelectric properties of PVDF nanocomposite films are investigated through PFM. The formation of the $\beta$-phase is enhanced adding a nanofiller, like GNPs or ZnO-NRs, or by chemical modification, dissolving different types of HMS, but without applying any electrical poling. The piezoelectric PVDF nanocomposite films are fabricated by a simple solution casting method. The piezoelectric response of the different samples is investigated, and it is correlated both with the relative fraction of the $\beta$-phase ($F(\beta)$) and with the surface morphology (i.e., the spherulite average diameter). The morphology of the produced samples was investigated through FE-SEM and AFM. The $\beta$-phase formation was assessed through FT-IR and XRD.

## *4.1 Introduction*

As above mentioned, the increasing of the β-phase is essential to enhance the piezoelectric response of PVDF [63,64]. A conventional way to induce a preferred orientation of the dipoles along the field direction, thus increasing the electroactive response of the material, is electric field poling, which consists of applying a very high DC electric field (in the range of $10^6$ V/m) to the sample at elevated temperatures (around 120 °C) [65]. However, electric poling is not a convenient or cost-effective industrial approach. Recently, in order to overcome this problem associated with the nucleation of the electroactive state in PVDF, alternative strategies, such as mechanical stretching [66]; heat-controlled spin coating [67]; addition to the PVDF matrix of external additives such

as clay [68], metal oxides [69], metal nanoparticles [9], or ceramic filler [70]; or a combination of spin coating and additive dissolution [71] have been proposed. Such additives are said to yield a large increase in the β-phase content. Several experimental and theoretical studies have confirmed that the use of carbon nanotubes (CNTs) as filler in the PVDF matrix can lead to a relevant increase in the β-phase content [72]. Moreover, the role of graphene nanoplatelets (GNPs) in the nucleation of the electroactive phase in PVDF nanocomposites has been recently investigated [73].

GNPs are 2D nanostructures having a high aspect ratio and a large surface area, which promotes a very strong interfacial interaction with the polymeric chains in nanocomposites. This results in an enhancement of the electric [74], mechanical [73], piezoresistive [75], and piezoelectric [76] properties of the host polymer. The use of ZnO nanorods as fillers in PVDF nanocomposites has been also proposed [77], with the aim of exploiting the synergistic effect on the piezoresponse of piezoelectric ZnO nanostructures [35] and PVDF. An alternative method to enhance the piezoelectric phase in PVDF is the dissolution of a hexahydrate metallic salt (HMS) during the production process of the polymeric film [78]. It was demonstrated that the hydrogen bonding interaction between HMS and PVDF contributes to the β-phase nucleation.

## *4.2 Deposition of PVDF Nanocomposites*

In this thesis the PVDF nanocomposite films are deposited using a simple solution casting method, developed by Bidsorkhi and Chandraiaghari during their PhD thesis [19,79]. PVDF (Solef 6010, Solvay plastics, with molecular weight of 32,000 g/mol) was used as received. GNPs were produced by thermal expansion in air at 1150°C for ~5 s of commercially available Graphite Intercalation Compound (GIC), and successive liquid-phase exfoliation by probe sonication, whereas ZnO-NRs were synthesized through thermal decomposition of zinc acetate di-hydrate, according to the procedure described in [35,74,80]. As shown in Fig. 49, from the FE-SEM and AFM images, the GNPs are characterized by thickness in the range of 2-10 nm and average lateral dimensions of up to a few microns, whereas ZnO-NRs have average diameter in the range 30-50 nm and length of ~500 nm.

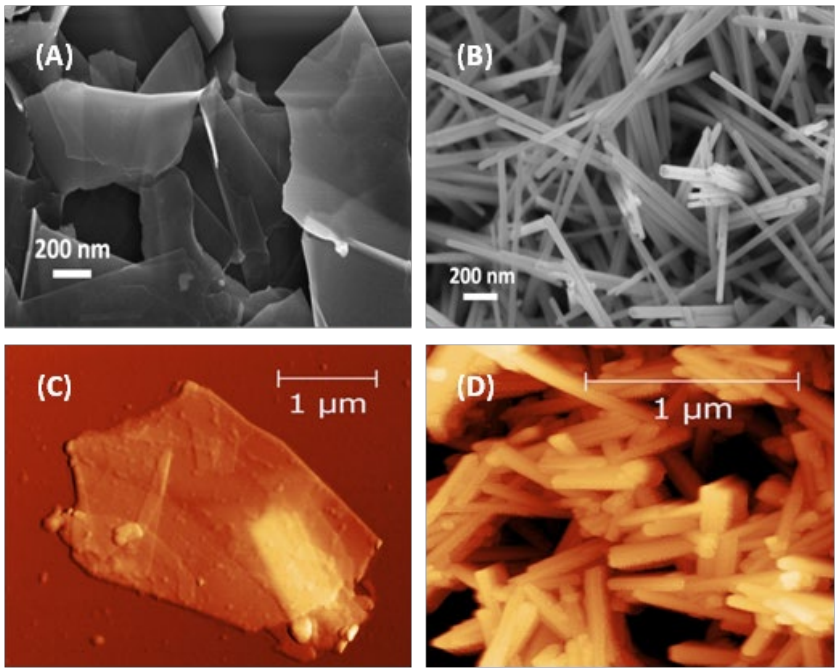


**Fig. 49 FE-SEM micrographs of GNPs (A), and ZnO-NRs (B). AFM micrographs of a GNP flake (C), and ZnO-NRs (D)** [77].

N,N dimethylformaide (DMF, Sigma–Aldrich, ≥99%) and acetone (ACS reagent, ≥99.5%) were employed as solvents, zinc nitrate hexahydrate [$Zn(NO_3)_2 \cdot 6H_2O$] (Sigma–Aldrich, ≥98%), magnesium nitrate hexahydrate [$Mg(NO_3)_2 \cdot 6H_2O$] (Sigma–Aldrich, ACS reagent, 99%), magnesium chloride hexahydrate [$MgCl_2 \cdot 6H_2O$] (Sigma–Aldrich, ≥99%), aluminium chloride hexahydrate [$AlCl_3 \cdot 6H_2O$] (Sigma–Aldrich, ≥99%), iron chloride hexahydrate [$FeCl_3 \cdot 6H_2O$] (Sigma–Aldrich, ≥97%) were used as received.

Four different production routes of PVDF nanocomposite films have been developed in order to enhance the piezoelectric response without electrical poling.

### *4.2.1 Route 1 (R1) – Direct exfoliation of expanded graphite in PVDF solution*

The GNP-PVDF nanocomposite films were fabricated via a solution mixing method [73]. PVDF was firstly dissolved in N,N-dimethylformamide (DMF), through 2 hours-magnetic stirring at 65 °C. Then, thermally expanded graphite (EG), produced through thermal

expansion of a graphite intercalation compound (GIC) in air at 1150°C for ~ 5s [74], were dispersed in the PVDF-DMF solution using an ultrasonic processor in pulsed mode for 20 minutes. The obtained mixture was casted onto a glass plate and the solvent was evaporated in oven for 8 hours at 80°C, as sketched in Fig. 50. The weight concentration of the produced GNP-PVDF nanocomposite films were 0.3 wt.%, 0.5 wt.%, and 0.7 wt.%. Once produced the obtained films, having thickness of approximately 30 μm, were peeled off the substrate. According to [73,81], the advantage of this method is that, at concentrations below 1 wt.%, nanostructures are dispersed homogeneously inside the polymer matrix. Moreover, GNPs are distributed uniformly amongst polymer chains by this method. This results in enhancement of the $\beta$-phase in PVDF nanocomposites. Neat PVDF film was fabricated following only steps 1, 3, 4 and 5 in Fig. 50.

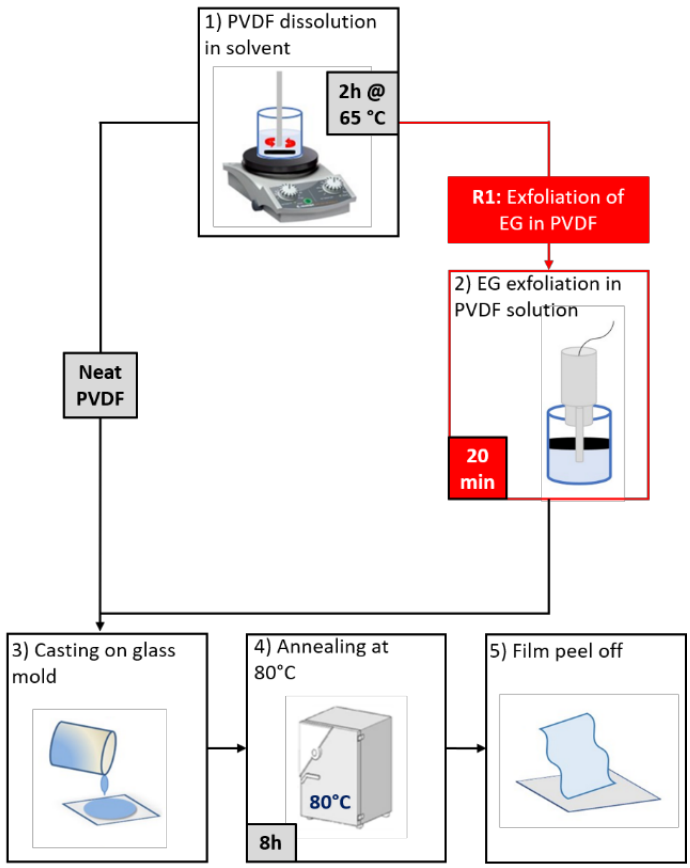


**Fig. 50 Schematic illustration of the solution-derived Neat PVDF and PVDF nanocomposite thin film through direct exfoliation of EG in PVDF solution.**

### *4.2.2 Route 2 (R2) – Solution-induced incorporation of nanofiller in PVDF*

PVDF nanocomposites films loaded with a low amount of nanofillers (0.1 wt.%) were prepared through solution-induced incorporation of the nanofiller in the polymer [81]. At first, nanofillers (either GNPs or ZnO-NRs) were dispersed homogeneously in a solvent mixture through a short probe sonication cycle (5 min in pulse mode at 40% in power amplitude). Next, PVDF powder was added to the as-obtained nanofiller suspension and stirred for 3 h. Flexible and self-standing films, having thickness of approximately 15 μm, were obtained by casting the nano-filled solution onto a clean glass plate, followed by subsequent solvent evaporation in an oven at 100°C for 12 h, as sketched in Fig. 51.

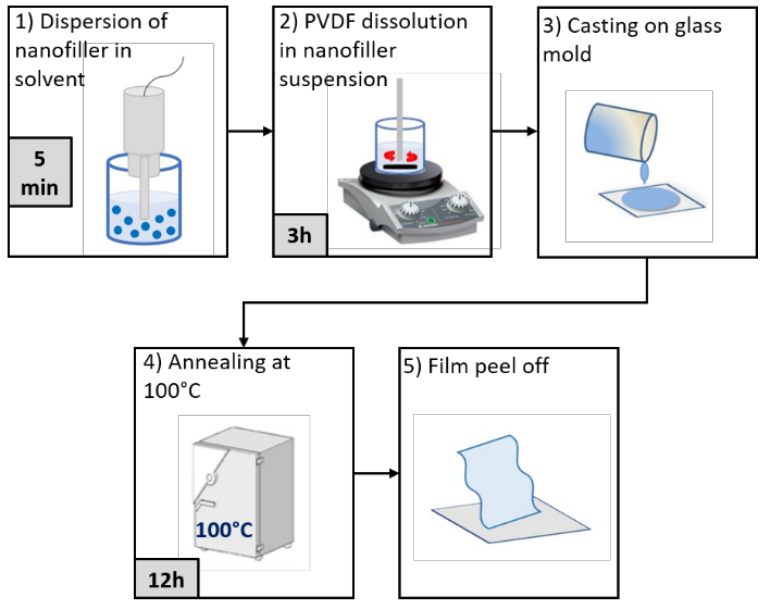


**Fig. 51 Preparation of PVDF nanocomposite thin film through Solution-induced incorporation of nanofiller in PVDF.**

In this case the Neat PVDF film was prepared by dissolving 5 wt.% PVDF powder in 20 mL of a solvent mixture consisting of DMF and acetone (1:1 v/v), chosen according to Hansen's solubility parameters as a good combination to fully dissolve PVDF [82]. A clear and transparent solution was obtained upon continuous stirring at room temperature for 3 h, ensuring the complete dissolution of PVDF. In order to have a

complete evaporation of the solvent, the solution was casted onto a clean glass plate and placed in an oven at 100 °C for 12 h. Finally, the obtained films, having thickness of approximately 15 μm each, were peeled off the substrate [77,81].

### *4.2.3 Route 3 (R3) – Dissolution of hexahydrate salt of different metals (HMS) in PVDF*

The PVDF films produced with the addition of 0.2 wt.% hexahydrate salts of different metals (like zinc, manganese, aluminum, iron) were prepared according to [81]. The samples were prepared through dissolution of the HMS in a solvent mixture of DMF and acetone (1:1 v/v) (Fig. 52). Next, PVDF powder was added to the as-obtained nanofiller suspension and stirred for 3 h. As sketched in Fig. 52, upon casting the obtained solution on a clean glass plate and evaporating the solvent at 100 °C for 12 h, we obtained a flexible self-standing film. The HMS concentration was chosen based on preliminary FT-IR measurements carried out in a previous study as the one corresponding to the most intense peaks of the β-phase in the IR spectrum of PVDF nanocomposite [81].

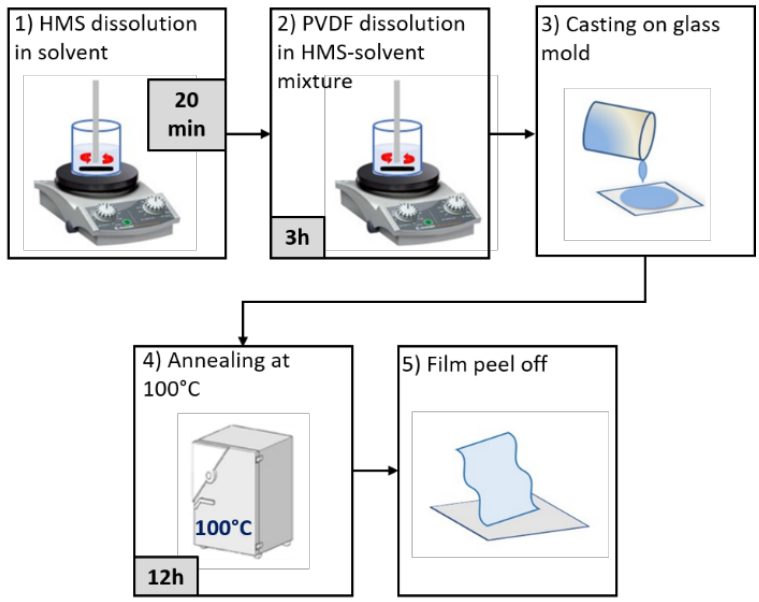


**Fig. 52 Schematic illustration of the solution-derived PVDF nanocomposite thin film through the ddissolution of different HMS in PVDF.**

### 4.2.4 Route 4 (R4) – Combined nanofiller dispersion and HS- dissolution

In order to produce PVDF self-standing nanocomposite films filled with GNPs or ZnO NRs, at first, HMS was dissolved in a solvent mixture of DMF and acetone (1:1 v/v). Next, the nanofiller (either GNPs or ZnO NRs, 0.1 wt.%) was dispersed homogeneously in the HMS solution through a short probe sonication (5 min in pulse mode at 40% in power amplitude). Finally, PVDF powder was added to the as-obtained colloidal suspension and stirred for 3 h, and the nanocomposite films were finally obtained as described above and sketched in Fig. 53.

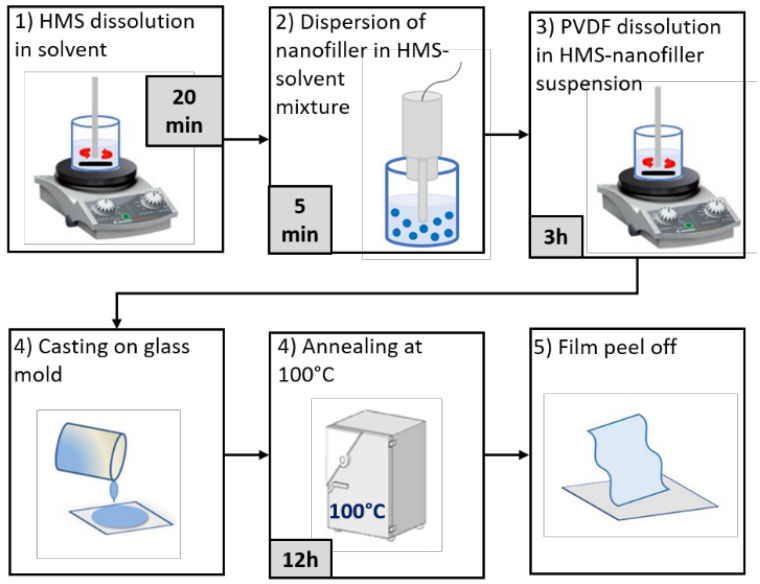


**Fig. 53 Schematic illustration of the solution-derived PVDF nanocomposite thin film combining the nanofiller dispersion and the HMS-dissolution.**

## 4.3 Techniques used to characterize the PVDF Nanocomposites

The produced samples, summarized in Table 5, are characterized in terms of morphology using a FE-SEM (Zeiss Auriga) operating with an accelerating voltage of 3 kV. A Quorum Technologies Q150T ES sputter coater (Laughton, East Sussex, UK) was used to metallize the PVDF films prior to SEM imaging with 20 nm of Cr, in order to prevent charging. The

**Table 5 List of PVDF films prepared, their composition and production process.**

| Sample | Rout | GNPs (wt%) | ZnO-NRs (wt%) | Hexahydrate Salt (0.2 wt%) |
|---|---|---|---|---|
| **R1-PVDF** | R1 | - | - | - |
| **R1-GNP-0.3** | R1 | 0.3 | - | - |
| **R1-GNP-0.5** | R1 | 0.5 | - | - |
| **R1-GNP-0.7** | R1 | 0.7 | - | - |
| **R2-PVDF** | R2 | - | - | - |
| **R2-GNP** | R2 | 0.1 | - | - |
| **R2-ZnO** | R2 | - | 0.1 | - |
| **R3-HS1** | R3 | - | - | $Zn(NO_3)_2{\cdot}6H_2O$ |
| **R3-HS2** | R3 | - | - | $Mg(NO_3)_2{\cdot}6H_2O$ |
| **R3-HS3** | R3 | - | - | $MgCl_2{\cdot}6H_2O$ |
| **R3-HS4** | R3 | - | - | $AlCl_3{\cdot}6H_2O$ |
| **R3-HS5** | R3 | - | - | $FeCl_3{\cdot}6H_2O$ |
| **R4-HS1-GNP** | R4 | 0.1 | - | $Zn(NO_3)_2{\cdot}6H_2O$ |
| **R4-HS1-ZnO** | R4 | - | 0.1 | $Zn(NO_3)_2{\cdot}6H_2O$ |

$\beta$-phase formation was assessed through Fourier transform infrared spectroscopy (FT-IR) and XRD.

The FT-IR measurements were performed, in collaboration with ENEA, Frascati, Italy, using a single-beam instrument (Bruker Tensor 27), equipped with a room temperature deuterated triglycine sulfate (DTGS) detector, mid-IR source and a KBr beamsplitter. Spectra were acquired in the range 4000-600 $cm^{-1}$ with resolution of $cm^{-1}$. Samples were analyzed in the attenuated total reflection (ATR) configuration, using the Pike Miracle ATR cell equipped with a Diamond/ZnSe crystal, with a sampling area of 6 mm diameter.

The XRPD measurements were performed, in collaboration with Department of Earth Sciences, Sapienza University of Rome, using the same instrumentations described in Chapter III section 3.3. Data were collected in a 2θ angular range extending from 7° to 100° with a step size 0.022° and 1 s counting time. Samples were prepared as capillaries loaded with respective nanostructures in powder form obtained after three steps of centrifuge with the high-shear mixer.

The piezoelectric properties of our samples were assessed through PFM [31] measuring the piezoelectric coefficient $d_{33}$. For this purpose, we used the Bruker-Veeco Dimension Icon AFM with a Co–Cr-coated-tip silicon cantilever (MESP-RC-V2, Bruker) [76].

### *4.3.1 Morphological Characterization*

FE-SEM images of neat PVDF produced according to route R1 are shown in Fig. 54(a) and (b).

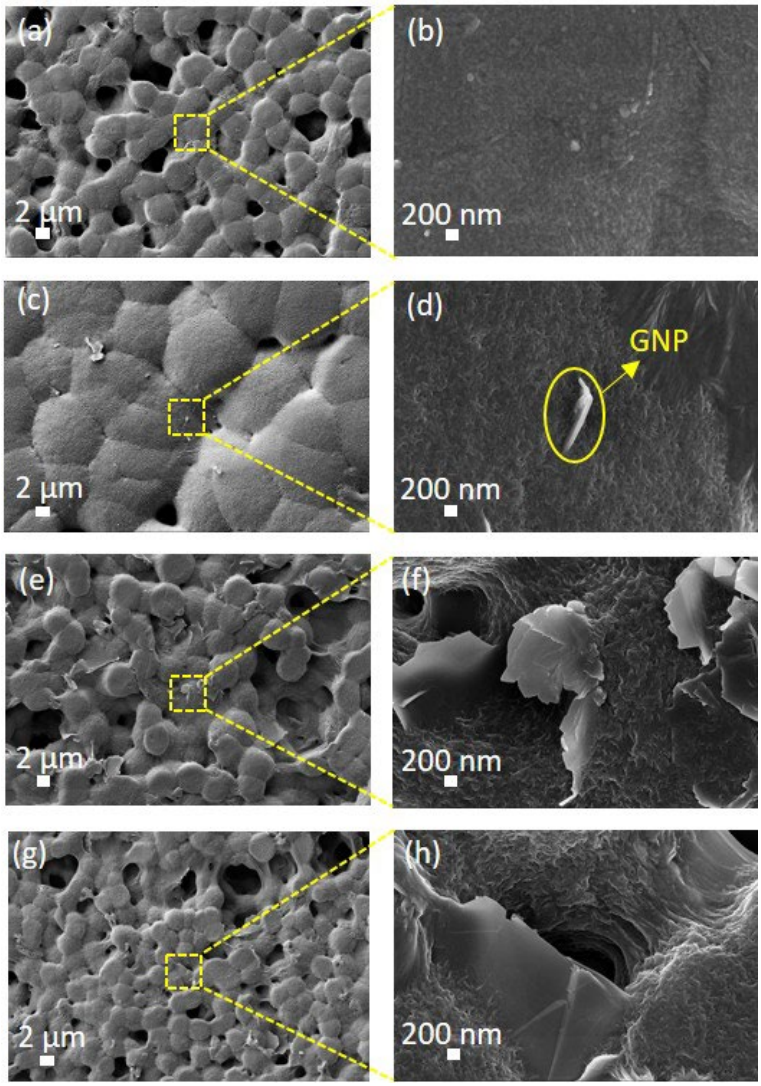


**Fig. 54 FE-SEM images of PVDF films produced via route 1: neat PVDF (a), (b) PVDF-GNP nanocomposite at 0.3 wt% (c), (d), PVDF-GNP nanocomposite at 0.5 wt% (e), (f), PVDF-GNP nanocomposite at 0.7 wt% (g), (h)** [77].

The surface is characterized by spherulitic structure with porosity in the micrometric range. When we added the GNP, we observed a similar spherulitic structure, and a good integration between the GNPs and the polymer matrix, since the GNPs are well embedded into the PVDF. Fig. 54(d), (f) and (h) show the details of GNPs emerging from the surface of the composite films and partially covered by the polymer matrix at 0.3 wt%, at 0.5 wt% and at 0.7 wt%, respectively. Fig. 54(c), (e) and (g) show the FE-SEM surface images for the PVDF/GNP composite films at 0.3 wt%, at 0.5 wt% and at 0.7 wt%, respectively. Is observed that the dimensions of the spherulites decrease as the GNP concentration increases, as described in [73] (see Table 6).

FE-SEM images of neat-PVDF and PVDF-nanocomposite films produced through route R2 are shown in Fig. 55 (a)-(f).

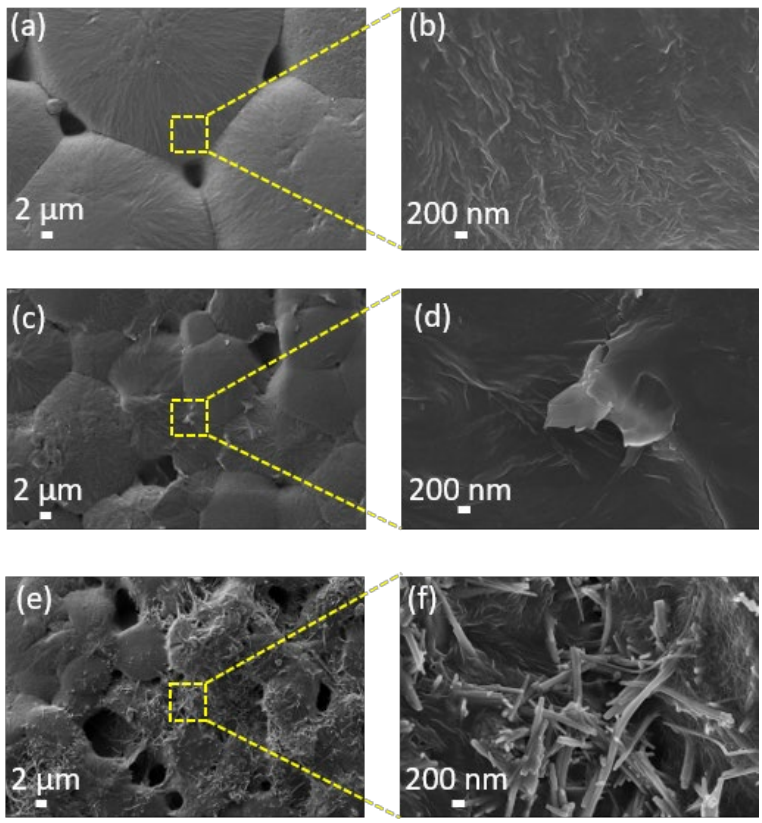


**Fig. 55 FE-SEM images of PVDF films produced via route 2: neat PVDF (a), (b), PVDF-GNP nanocomposite at 0.1 wt.% (c), (d), PVDF-ZnO-NR nanocomposite at 0.1 wt.% (e), (f)** [77].

It is evident that the solution mixing leads to a homogenous dispersion of the 2D shaped GNPs and of the rod-shaped ZnO-NRs in the PVDF

matrix, due to the respective interaction of carboxyl and hydroxyl groups of nanofillers with PVDF [71]. Nanofillers are well encapsulated within the polymer matrix, thereby resulting in a good interfacial interaction. This interaction changes the morphology of the polymer surrounding the nanostructures, as can be observed through the comparison of the micrographs in Figs. 3(b), (d), and (f), the latter representing the neat PVDF sample. In general, it is observed that the average larger spherulites are found in all samples produced according to route R2. This is probably due to the fact that the EG exfoliation in the PVDF solution through ultrasonication produced a disruption of the polymer chains. In Table 6 the diameters of the spherulites are reported.

Fig. 56 show the FE-SEM micrographs at low and high magnifications of the samples prepared with the addition of HMS using route R3. The typical spherulitic morphology is largely affected by the nucleation and formation of the polymer chains during the solid–liquid phase separation. The yellow arrows in Fig. 56 show HMS crystals distributed within the polymer matrix. The interaction between HMS and polymer modifies the morphology of the composite, in particular affecting the average spherulite diameter, as showed in Table 6. In general, we observed a reduction of the spherulite diameter upon addition of the HMS, except for $FeCl_3 \cdot 6H_2O$. HMS originates nucleation sites in the polymer, owing to the strong interfacial interaction between the metallic ion of the HMS and the polymeric chain.

In Fig. 57 are reported the FE-SEM micrographs at low and high magnifications of the samples prepared with the addition of HMS plus nanofillers (either GNPs or ZnO NRs) using route R4. The yellow and the orange arrows show the HMS crystals and the nanofillers distributed within the polymer matrix. Also, in this case the spherulitic morphology is affected by the nucleation and formation of the polymer chains during the solid–liquid phase separation. It is observed that the combination of both HMS and nanofillers dispersed inside the polymer does not induce a reduction of the spherulite diameters, as it can be observed in Table 6.

All the diameters of the spherulites were evaluated from FE-SEM images using a commercial image processing software (ImageJ ©). The mean value of the spherulite diameter was estimated by averaging the

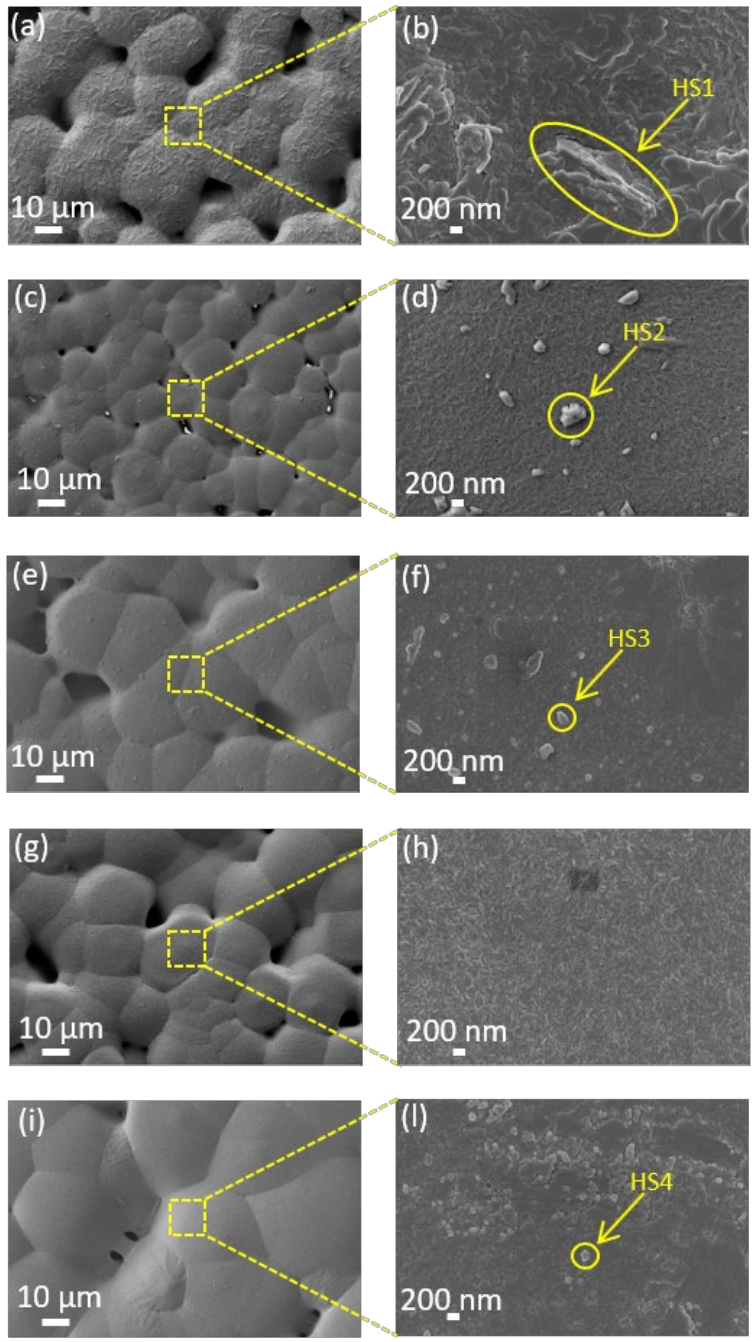


***Fig. 56 FE-SEM low-magnification and high-magnification micrographs of (a,b) R3-HS1 film, (c,d) R3-HS2 film, (e,f) R3-HS3 film, (g,h) R3-HS4 film, and (i,l) R3-HS5 film*** [78].

diameters of 10 different spherulites. The obtained values are reported in Table 6.

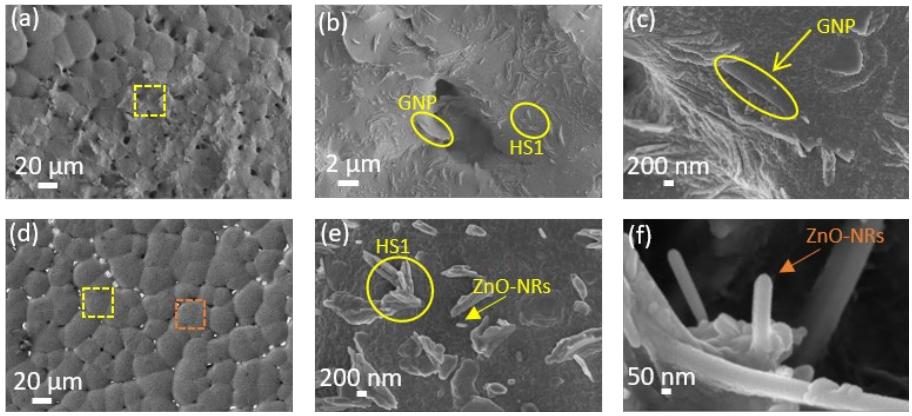


**Fig. 57 FE-SEM low-magnification and high-magnification micrographs of the sample R4-HS1-GNP (a–c), and of the sample R4-HS1-ZnO (d–f)** [78].

**Table 6 Average values of the spherulite diameter estimated from FE-SEM images.**

| Sample | Spherulite diameter (µm) | $F(\beta)$ (%) | $\langle d_{33} \rangle$ (pm/V) |
|---|---|---|---|
| **R1-PVDF** | 4.87 ± 0.97 | 68.70 | 2.32 ± 0.83 |
| **R1-GNP-0.3** | 9.79 ± 2.31 | 48.10 | 3.61 ± 1.50 |
| **R1-GNP-0.5** | 5.00 ± 0.95 | 64.70 | 5.00 ± 0.90 |
| **R1-GNP-0.7** | 4.13 ± 0.20 | 61.50 | 3.87 ± 1.06 |
| **R2-PVDF** | 28.58 ± 4.56 | 69.36 | 4.65 ± 1.70 |
| **R2-GNP** | 13.47 ± 4.09 | 45.45 | 6.54 ± 0.80 |
| **R2-ZnO** | 7.25 ± 1.40 | 37.95 | 6.28 ± 0.97 |
| **R3-HS1** | 28.58 ± 4.56 | 78.25 | 5.87 ± 2.54 |
| **R3-HS2** | 20.09 ± 5.33 | 82.17 | 8.88 ± 3.14 |
| **R3-HS3** | 11.87 ± 3.74 | 79.73 | 6.54 ± 2.13 |
| **R3-HS4** | 26.37 ± 5.17 | 81.18 | 6.34 ± 0.60 |
| **R3-HS5** | 22.19 ± 4.59 | 65.70 | 2.04 ± 0.69 |
| **R4-HS1-GNP** | 34.55 ± 4.67 | 75.98 | 2.05 ± 0.60 |
| **R4-HS1-ZnO** | 27.79 ± 5.50 | 77.87 | 3.89 ± 1.48 |

### *4.3.2 FT-IR Analysis*

The presence of the $\beta$-phase in the produced PVDF nanocomposite films was assessed using FT-IR spectroscopy. The characteristic peaks attributed to the FT-IR absorbance band of $\alpha$-phase are located at 1423,

1383, 120, 1147, 976, 855, 795 and 763 $cm^{-1}$ [35]. The electroactive polar $\beta$-phase can be well identified from peaks at 1275 $cm^{-1}$ and 840 $cm^{-1}$, whereas the semi-polar $\gamma$-phase is evident from the peak at 1234 $cm^{-1}$ [9,83]. All samples produced according to the different routes R1-R4 showed the presence of the electroactive phase, evinced through the characteristic $\gamma$ peak at 1234 $cm^{-1}$ and $\beta$ peak at 840 $cm^{-1}$, as it appears in Fig. 58.

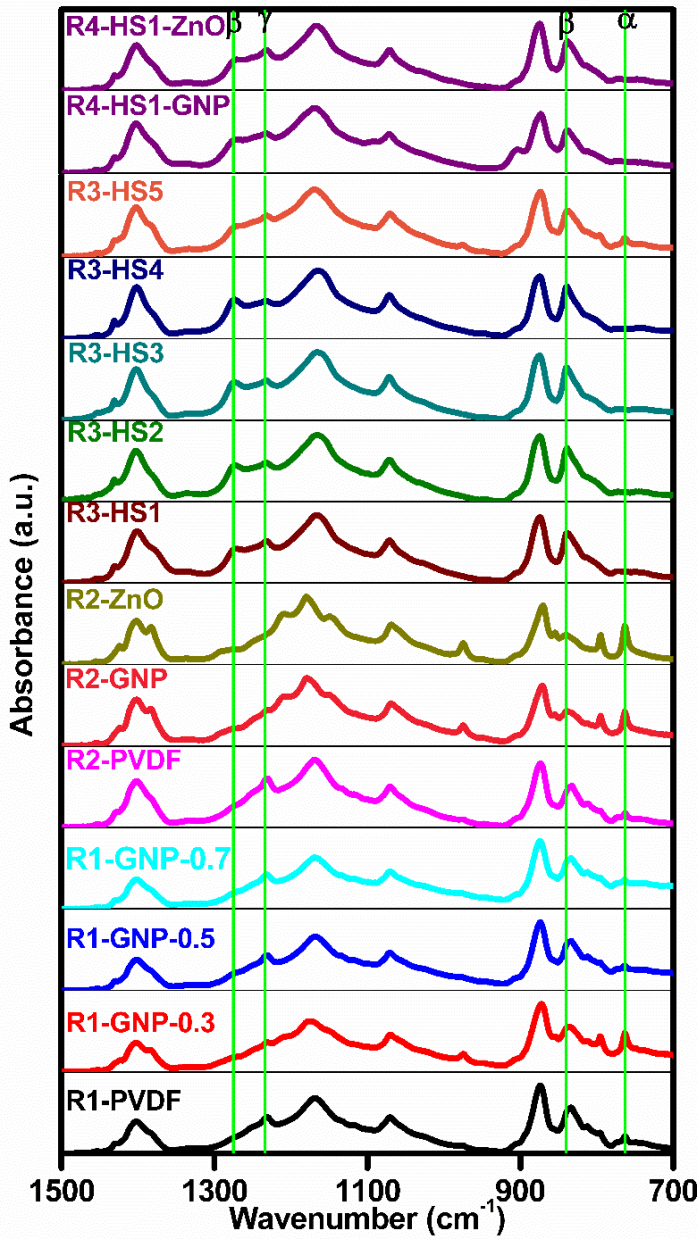


**Fig. 58 FT-IR spectra for PVDF/GNP nanocomposites.**

The FT-IR measurements are used to evaluate the relative fraction of the electroactive $\beta$-phase of PVDF, by using the following equation [84]:

$$F(\beta) = \frac{A_\beta}{\left(K_\beta / K_\alpha\right) A_\alpha + A_\beta} \tag{4.5}$$

where $F(\beta)$, represents the $\beta$-phase content; $A_\alpha$ and $A_\beta$ the absorbance at 766 and 840 cm-1, respectively; $K_\alpha$ and $K_\beta$ are the absorption coefficient at the respective wavenumbers, which values are 6.1 x $10^4$ and 7.7 x $10^4$ $cm^2mol^{-1}$, respectively. The obtained values are reported in Table 6. Note that in the GNP-PVDF nanocomposite films produced according to R1 the fraction $F(\beta)$ is not directly proportional to the amount of GNP content. This is due to the fact that as shown in Fig. 54 the morphology and spherulite size of these composites are quite different. In PVDF nanocomposite films produced according to routes R2-R4, it is observed that when different types of HMS or HMS plus nanofillers are added, the fraction of the $\beta$-phase increases, except for the sample R3-HS5, compared with the value estimated for the neat PVDF. Vice versa, when only the GNP or ZnO-NRs are added (R2), *F(β)* decreased. In order to better understand these results, the XRD-analysis on the samples produced trough R2, R3 and R4 are performed.

### *4.3.3 XRD Analysis*

Fig. 59 shows the XRPD pattern of our samples. An easy discrimination and quantification of the $\alpha$- and $\beta$-phase can be devised from the intensity of the two relatively strong (100) and (020) reflections, located at ca.17.8 and 18.4° 2θ that are typical of the $\alpha$-phase [73]. Accordingly, we observed that the $\alpha$-phase is the abundant in the neat PVDF (sample R2-PVDF) as well as in the samples with nanofillers (samples R2-GNP and R2-ZnO). When we added the HMS or HMS plus nanofillers we, a part of the reduction of the intensity of the two (100) and (020) reflections, the broadening and shift of the position of the strongest peak from 20° to 20.4° [73]. This peak result from the coalescence of the strong (110) reflection of both phases, that of the $\beta$-phase being located at a slightly higher angle. This behavior is less evident in the sample prepared with the addition of the Fe-HMS (R3-HS5) and in the samples containing HMS plus

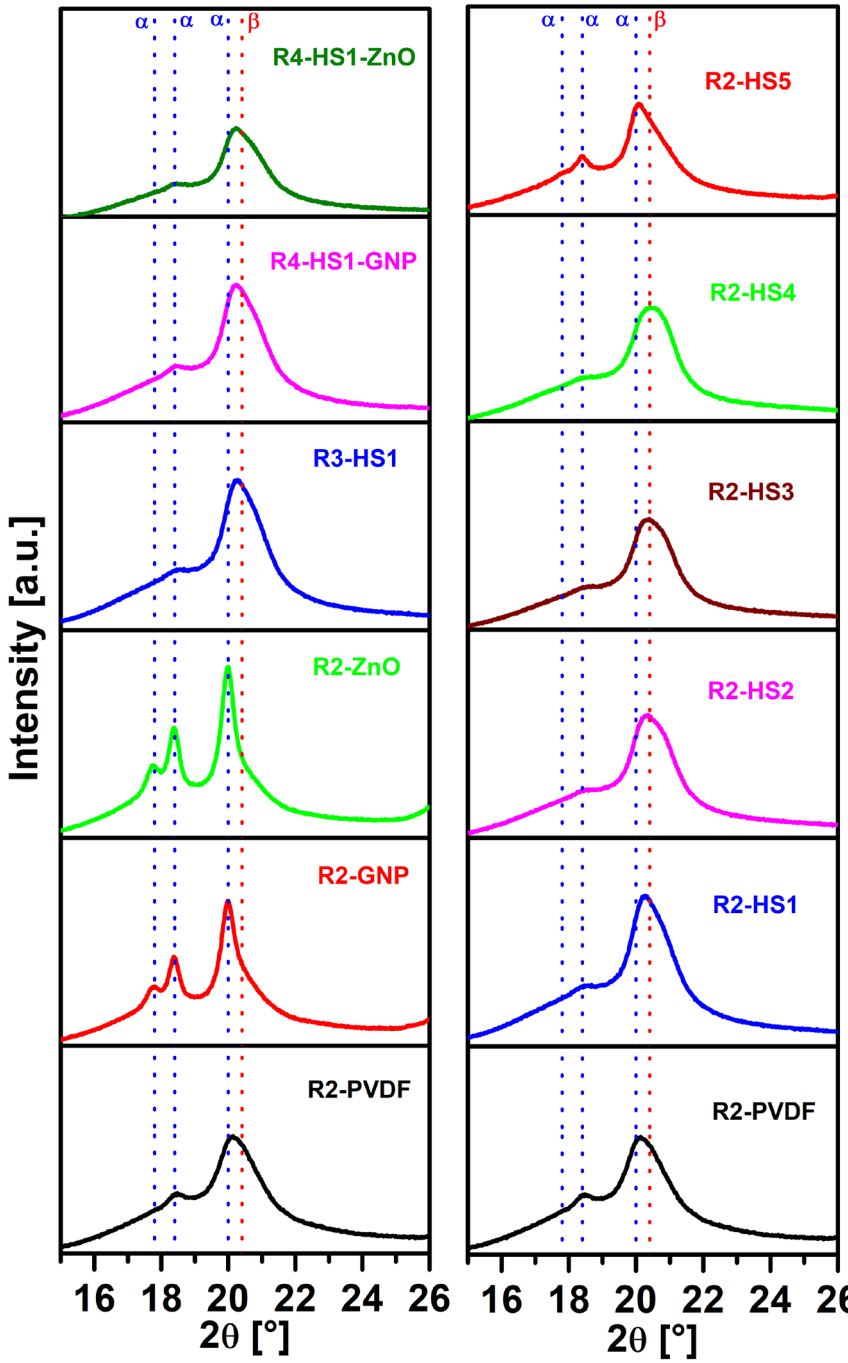


**Fig. 59 X-ray diffraction (XRD) pattern acquired on PVDF nanocomposites.**

nanofillers. Therefore, it is confirmed that the occurrence of $\beta$-phase is prevailing in the samples with the HMS (apart from R3-HS5) with respect to the samples containing both HMS and nanofillers. Based on the XRPD

and FT-IR data, we can conclude that a very small amount of HMS (0.2 wt %) hinders the $\alpha$-phase nucleation and preferentially promotes the polar $\beta$-phase formation. A possible mechanism for the $\beta$-phase enhancement induced by the dissolved HMS is the hydrogen bonding interactions between HMS and the $CF_2$ groups of PVDF [85].

### *4.3.4 Piezoelectric properties*

The PFM measurements were performed by applying to the tip an alternating voltage with the frequency of 15 kHz, and an increasing maximum amplitude $V_{ac}$ of 2, 4, 6, 8, or 10 V. The bottom electrode of the samples was grounded. We scanned 10 different areas (500 × 500) $nm^2$ in size, with 256 × 256 acquisition points per scanning area, and with a scan rate of 0.5 Hz. The 10 scanning areas were located in four different zones of the sample surface, as shown in Fig. 60.

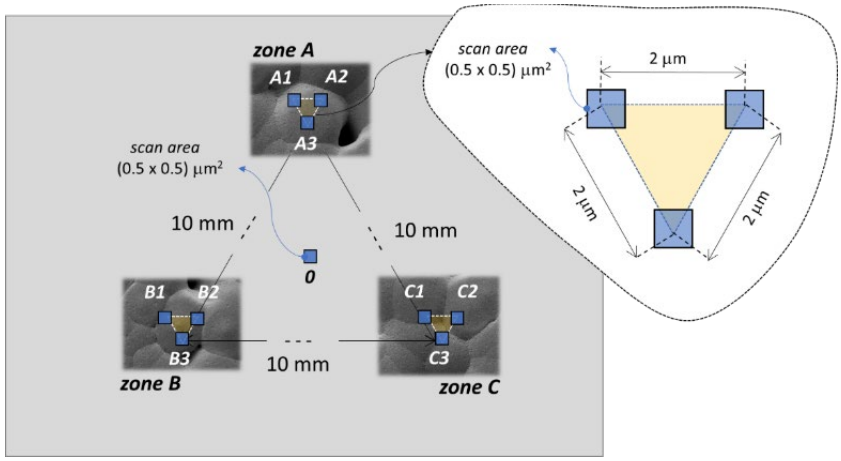


**Fig. 60 Sketch of the measurement points for the local piezoresponse of the sample through piezoresponse force microscopy (PFM)** [78]**.**

The first scanning area (labeled "0" in Fig. 60) was located in the center of the sample and was used as an approach area needed to verify whether the sample had a piezoelectric response. The next 9 scanning areas were located in three different zones of the sample surface, 10 mm apart from each other, as shown in Fig. 60. Two out of the three zones (Zone A and Zone B) are selected in proximity of the center of two different spherulites, whereas the third one includes the valley between two adjacent spherulites. This choice was made in order to characterize the

piezoresponse of areas of the sample with different morphologies and characteristics, with the aim of getting information about the uniformity of the piezoresponse over the whole sample surface.

The procedure applied to measure the piezoresponse of the sample through PFM is described in Chapter II, section 2.2.4. In particular in this case, once the calibration factor $\xi$ was obtained from Equation (2.6), we measured the PFM signal of a PVDF nanocomposite sample. For this purpose, we first scanned the approaching area (0 in Fig. 60) and then the three scanning areas in each selected zone (A, B, C in Fig. 60). For each *i*th scanning area, we obtained the displacement $A^i_{piezo}$ averaged over the (256 × 256) measurement points as follows:

$$A^i_{piezo} = V^i_{piezo}/\xi. \tag{4.1}$$

Since $A^i_{piezo}$ is also related to the applied voltage by [29,31]

$$A^i_{piezo} = d^i_{33}V_{ac} \tag{4.2}$$

we obtain the piezoelectric coefficient $d^i_{33}$ of the *i*th scanning area as the slope of the linear fit of $A^i_{piezo}$ versus the applied voltage $V_{ac}$. The piezoresponse coefficient of the *k*th zone of the sample ($d_{33}^{\text{zone } k}$), is then computed as the average value of the coefficients of the three scanned areas in that zone:

$$d_{33}^{\text{zone } k} = \sum_{i=1}^{3} d^i_{33} \Big/ 3. \tag{4.3}$$

Once the PFM measurements were performed in each selected zone of the sample, we estimated the average PFM response as

$$\langle d_{33} \rangle = \left(d^A_{33} + d^B_{33} + d^C_{33}\right)/3. \tag{4.4}$$

The standard deviation of $\langle d_{33} \rangle$ is representative of the uniformity of the piezoresponse of the sample.

In Fig. 61 and in Fig. 62 the topographic maps and the amplitude of the vertical (out-of-plane) signal measured through PFM over a scan area (500× 500) nm$^2$ in size of the produced samples are reported. The scanning areas were limited to a lateral size of only 500 nm in order to avoid cross-

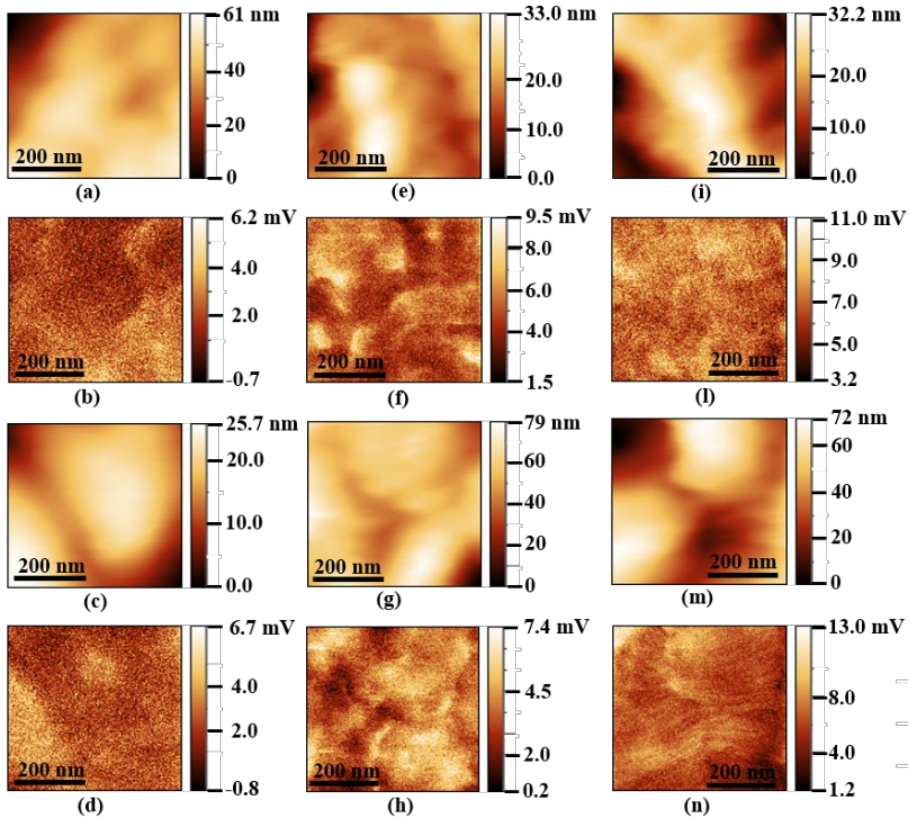


**Fig. 61 Morphological maps and vertical (out-of-plane) PFM signals at $V_{ac}$ = 10 V and at 15 kHz for R1-PVDF (a,b), for R1-GNP-0.3 (c,d), for R1-GNP-0.5 (e,f), for R1-GNP-0.7 (g,h), for R2-ZnO (i,l), for R2-GNP (m,n).**

talk between the amplitude of the vertical PFM and the topographic signals. In fact, under these conditions, the PFM scanned area is much smaller than the average size of spherulites, which ranges from about 10 μm to about 35 μm, as reported in Table 6. As the surface roughness is mainly related to the grain boundaries between spherulites, probing areas within a spherulite guarantees that the topographic signal can be well distinguished from the vertical PFM signal.

As observed from Fig. 61 and in Fig. 62 there is not a direct correlation between the amplitude of the vertical PFM signal and the AFM signal. This consideration allows to affirm that the piezoelectric effect is due to intrinsic piezoelectric properties of the materials and not originated from the cross-talk with the topography. This is in agreement with the results reported in PVDF by Serrado Nunes et al. [86], showing that the piezoelectric constant does not directly follow the topographic shape.

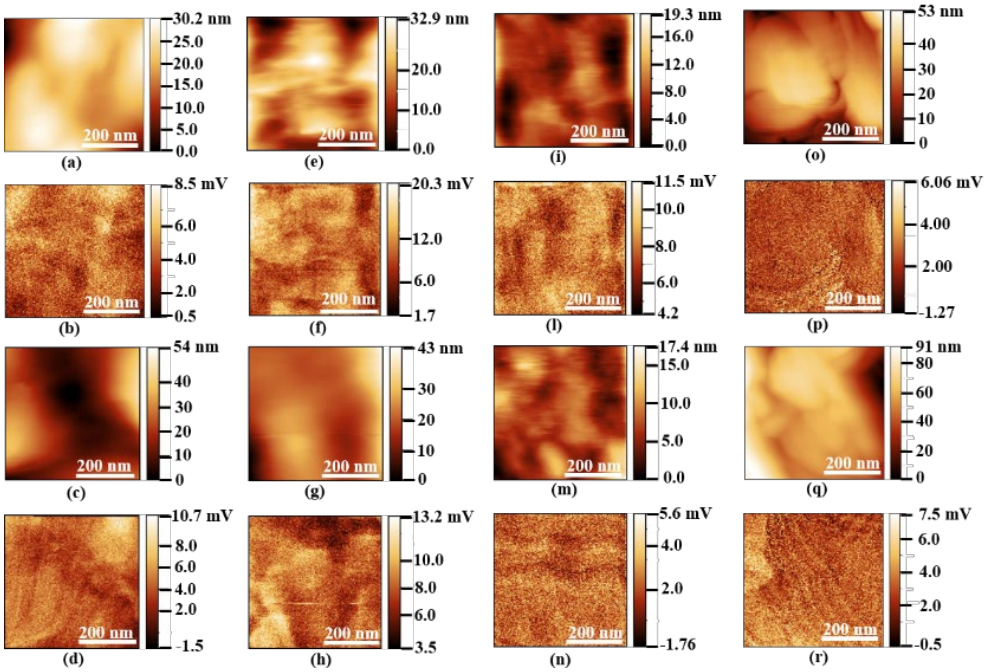


**Fig. 62 Morphological maps and vertical (out-of-plane) PFM signals at $V_{ac}$ = 10 V and at 15 kHz for Neat-PVDF (a,b), for R3-HS1 (c,d), for R3-HS2 (e,f), for R3-HS3 (g,h), for R3-HS4 (i,l), for R3-HS5 (m,n), for R4-HS1-GNP (o,p), and for R4-HS1-ZnO (q,r)** [78]**.**

Next, the average amplitude of the measured vertical displacement for each sample as a function of the amplitude ($V_{ac}$) of the applied alternating voltage is evaluated. The obtained data, which are averaged over 10 scanning areas, and the corresponding linear fits are reported in Fig. 63. Interpolating the measured data and using the calibration procedure described in Chapter II, section 2.2.4, the slope of the straight lines provides the piezoelectric coefficient $d_{33}$.

The average piezoelectric coefficients $d_{33}$ of the three different zones A, B, and C sketched in Fig. 60 for each sample are reported in Fig. 64, together with the corresponding standard deviations. We notice that the highest piezoelectric coefficient is provided by sample R3-HS2, produced using magnesium nitrate hexahydrate salt, with the maximum value of 13.48 pm/mV in zone A, located over a spherulite. The smallest piezoelectric performances are observed in sample R3-HS5, made with iron nitrate hexahydrate salt, and in the samples combining HMS-dissolution and nanofiller dispersion.

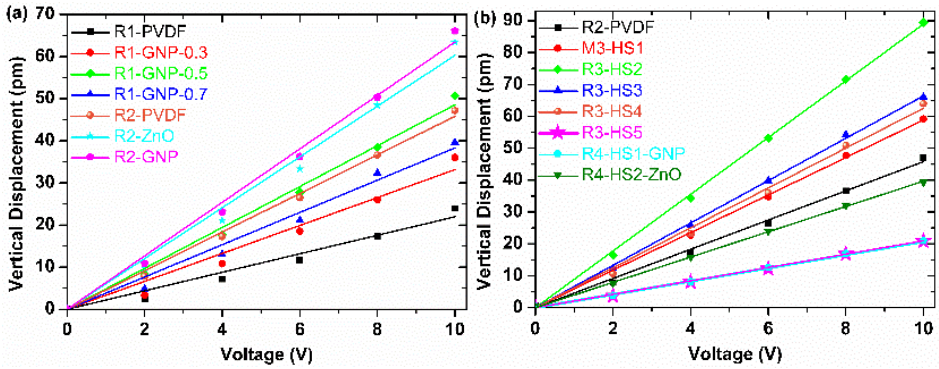


**Fig. 63 Average amplitude of the vertical displacement measured through PFM as a function of the applied voltage $V_{ac}$ [77,78].**

Furthermore, when the nanofillers are added through route R1, the piezoelectric coefficient does not have a considerable increase; on the contrary, when the nanofillers are dispersed through route R2, a significant enhancement of $d_{33}$ is observed. In all cases, the standard deviation of the measured $d_{33}$ in the different zones of the produced samples reaches maximum values of 31.4%, 34.2%, and 25.2% in the samples that are characterized by the highest roughness of the spherulite surface, as resulting from the AFM scanning in Fig. 61 and in Fig. 62.

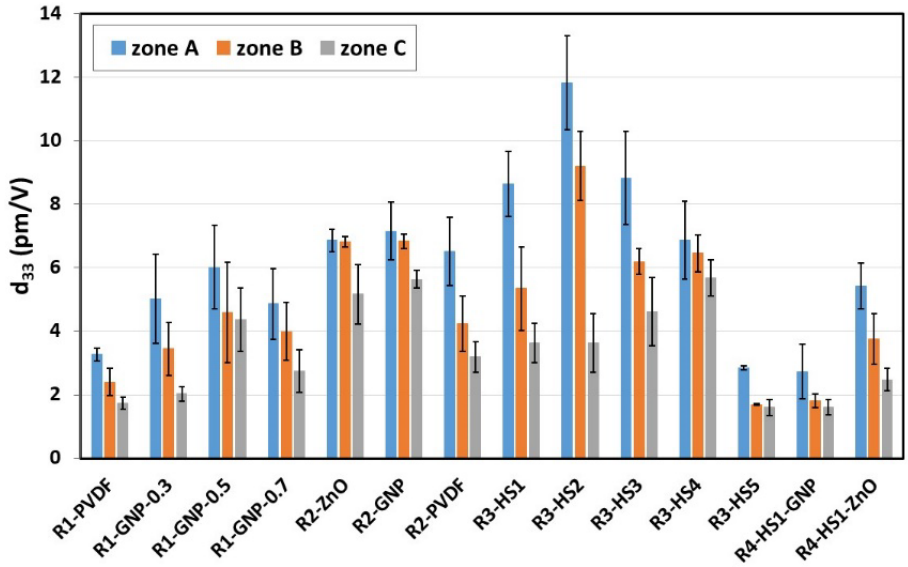


**Fig. 64 Measured average piezoresponse coefficient in the three zones of the produced samples, with standard deviation.**

This proves a correlation between piezoresponse and the local nanoscale morphology of the sample surface. The global average value of

the piezoresponse coefficient $\langle d_{33} \rangle$ for each sample, is computed according to Equation (4.4). The obtained values, including the corresponding standard deviations, are reported in Table 6. It is confirmed that the highest piezoresponse is observed in sample R3-HS2. In this case, the standard deviation varies in the range 30%–40% since it is representative of the local variation of $d_{33}$ over the sample surface. In order to correlate the piezoelectric coefficient with the presence of the $\beta$-phase in the samples, in Fig. 65 is reported the $\langle d_{33} \rangle$ as a function of $F(\beta)$ [77].

As expected from FT-IR and XRPD data, we notice that when we dissolve the HMS into PVDF, the piezoelectric coefficient increases. Indeed, the maximum value of $\langle d_{33} \rangle$ = (8.88 ± 3.14) pm/V was observed in sample R3-HS2, which is also characterized by the highest value of $F(\beta)$ (Table 6), while the lowest value of $\langle d_{33} \rangle$ = (2.04 ± 0.69) pm/V was observed in sample R3-HS5, in agreement with the FT-IR and XRPD data showing the lowest $\beta$-phase fraction. However, when we added only the nanofillers (samples R2-GNP and R2-ZnO), although the FT-IR and the XRD data show a low presence of the $\beta$-phase, we observed an enhancement of the $d_{33}$, if compared with the value estimated for the neat PVDF. Moreover, when we added both HMS and nanofillers, in contrast

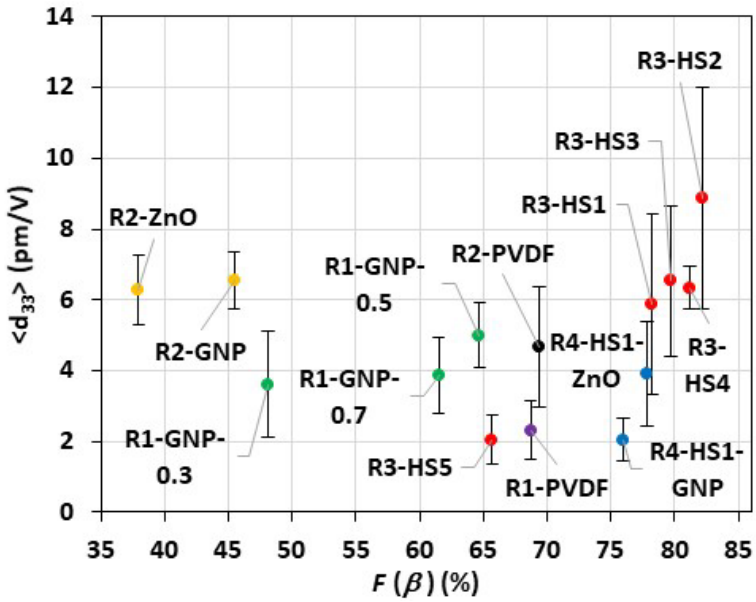


**Fig. 65 Averaged $d_{33}$ as a function of $F(\beta)$ of all produced samples, with standard deviation.**

with the observed increase of the $\beta$-phase deduced from the FT-IR and XRPD data, we found a decrease of $\langle d_{33} \rangle$ compared with the neat PVDF. It is speculated that the reason for this should be found with a poor alignment of the electroactive polymer chains along the vertical axis due to a destructive electrostatic interaction between the metallic part of the HMS filler, the nanofillers (GNP and ZnO NRs), and the $CF_2$ group of the PVDF.

Furthermore, when the nanofillers are added through route R1, the piezoelectric coefficient of the PVDF nanocomposite films increases as the relative fraction of $\beta$-phase in the sample rises. This result is expected, since the electroactive $\beta$-phase determines the piezoelectric response and is in agreement with what already reported for PVDF films [65]. On the other hand, the presence of the $\beta$-phase, as revealed via FT-IR analysis is not directly correlated to a high value of the piezoresponse coefficient (see Table 6).

We believe that the decrease of $\langle d_{33} \rangle$ when the HMS are added in combination with the nanofillers is due to a destructive interaction between the dissolved HMS and nanofillers (either GNPs or ZnO NRs). Dissolved HMS tends to form hydrogen bonding with the $CF_2$ group of the PVDF, which promotes electrostatic interactions between the PVDF polymer chain and metallic salts in the polar solvent, as sketched in Fig. 66 [32].

Moreover, we notice the formation of some nanofiller agglomerations in samples including HMS and either GNPs or ZnO NRs. For instance, Fig. 57 (a) clearly shows the presence of GNP agglomerations over the sample surface, which interfere with the formation of spherulites and, in turn, with the enhancement of the β-phase. Actually, the presence of filler agglomerates is observed in the sample with the lowest value of piezoresponse coefficient (i.e., R4-HS1-GNP). The incoherent interaction between HMS and nanofiller induces an incoherent distribution of the $\beta$-phase polymer chains, resulting in a poor $d_{33}$ signal.

The highest values of $d_{33}$ obtained adding the nanofillers using route R2, despite the lower content of $\beta$-phase, as compared to samples obtained using route R1 can be ascribed to the different fabrication processes employed. In fact, in R1 we used a tip-sonication to disperse the GNPs directly into the polymer solution. Whilst such process guarantees a good

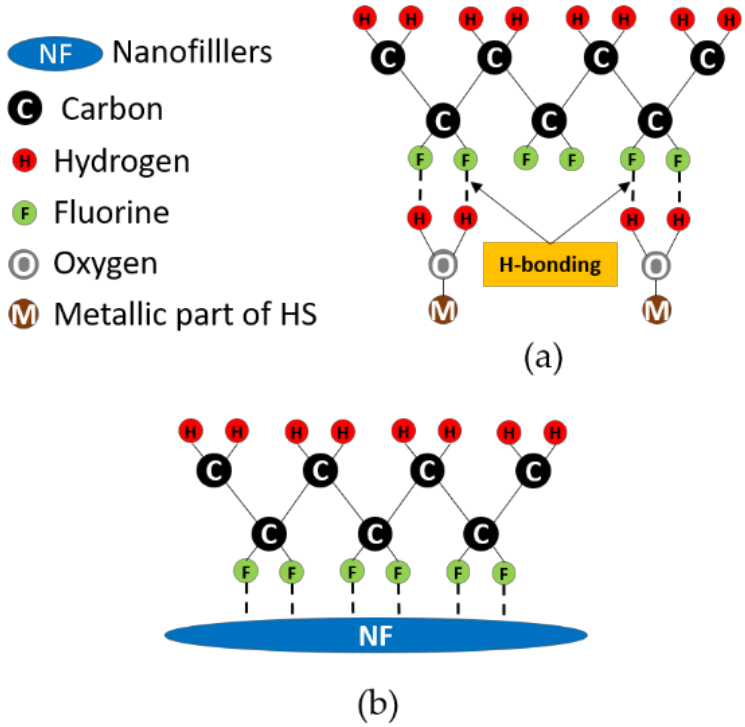


**Fig. 66 Schematic representation of (a) the formation of H-bonding with the metallic part of HS and the $CF_2$ group of PVDF, and (b) the electrostatic interaction between the nanofillers (either GNP or ZnO NRs) and the $CF_2$ group of PVDF** [78].

dispersion and uniformity of the filler in the polymer matrix, it also induces defects and damages to the polymeric chains, resulting in a lower $d_{33}$, if compared with samples produced through R2, where the absence of a direct tip-sonication on the polymer solution, ensures the integrity of the polymeric chains.

Furthermore, for the sample produced adding the HMS (R3 and R4), it is observed that when the average value of the spherulite diameter decreases, the piezoelectric coefficient of the PVDF nanocomposite films increases (Fig. 67). This trend is also observed with respect to the fraction of the $\beta$-phase, $F(\beta)$. Accordingly, the minimum value of $d_{33}$ and the largest spherulite diameter are observed in the sample containing the Fe-HMS (i.e., R3-HS5), due to the relatively large mass and small negative value of the standard electrode potential of $Fe^{3+}$, which weaken the hydrogen bond with PVDF. On the contrary, the highest value of $d_{33}$ (combined with the smaller size of spherulites) is observed in the sample

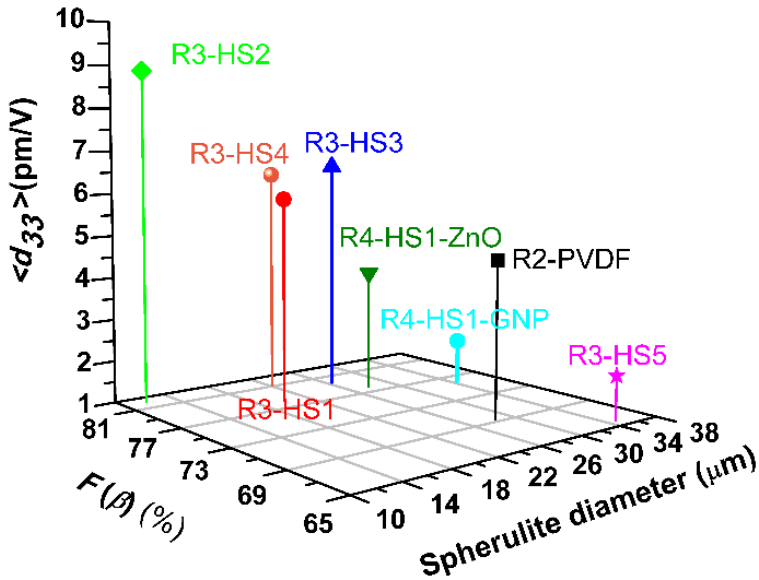


**Fig. 67 Averaged piezoelectric coefficient, $d_{33}$, vs relative fraction of the β-phase, $F(\beta)$, and averaged spherulite diameter of the produced samples** [78].

containing the Mg-HMS (i.e., R3-HS2), with the standard electrode potential of the $Mg^{2+}$ ion being the most negative among the metals in the other HMSs used. These results are in agreement with data reported in literature [86], in which it is shown that a smaller diameter of the spherulites corresponds to a higher presence of $\beta$-phase and, consequently, to a higher piezoelectric coefficient.

In this study it is observed how the incorporation of $Zn(NO_3)_2{\cdot}6H_2O$, $Mg(NO_3)_2{\cdot}6H_2O$, $MgCl_2{\cdot}6H_2O$, and $AlCl_3{\cdot}6H_2O$ salts into the PVDF matrix induces an increase of the electroactive phase, which can be ascribed to the combined effect of the change in the inherent dipole moment of the electroactive phase contained in the PVDF itself, and of the formation of H-bonding between the metallic part of the HMS filler and of PVDF via electrostatic interactions [85]. These combined effects are enhanced in the PVDF nanocomposite produced using HMS containing Mg nitrate, since $Mg^{2+}$ is characterized by the most negative redox potential with respect to the other metal ions considered in this study. This result is in line with the finding that the sample produced through dissolution in PVDF of $FeCl_3{\cdot}6H_2O$, in which the ion $Fe^{3+}$ has a nearly zero standard potential, has a very poor piezoelectric response.

The increase of the β-phase fraction in the samples R3-HS1, R3-HS2, R3-HS3, and R3-HS4, produced through dissolution of an HMS containing metals with negative redox potential, was correlated to the enhancement of the piezoelectric coefficient, measured through PFM. At the same time, the reduction of *β*-phase in the sample R3-HS5 containing Fe corresponds to the reduction of the piezoelectric coefficient compared with neat PVDF. In particular, the highest average value of $d_{33}$ (i.e., 8.88 ± 3.14 pm/V) and the highest local peak value (i.e., 13.49 pm/V) were measured in the sample containing $Mg(NO_3)_2 \cdot 6H_2O$ salt (R3-HS2). This sample also contained the highest fraction of *β*-phase (i.e., 82.18%) with respect to all other samples, and was characterized by the lowest average value of spherulite diameter (i.e., 11.87 ± 3.74 μm), between the samples that contain HMS.

In any case, it is worth underlining that if we analyse the samples produced through the production process R3 or R4, we observe that the piezoelectric coefficient increases as the relative fraction of *β*-phase rises. Moreover, $d_{33}$ and the fraction of β-phase in general increase as the dimension of the averaged spherulite diameter decreases.

The addition of HMS salts results in a marked improvement of the $d_{33}$ value. In particular, it was obtained an enhancement of the piezoelectric coefficient of modified PVDF films with obtained values consistent with those reported in the literature [68,87,88], but through a facile, cost-effective, and time-saving production route.

For these samples the XRPD and FT-IR findings were corroborated by SEM investigation, revealing that the nucleation kinetics are enhanced by the presence of the HMS salts, as evidenced by the formation of an increasing number of spherulites with increasing numbers of nucleation sites, in turn leading to a reduction of the average spherulite diameter.

# *CHAPTER V*

## *ENERGY HARVESTING DEVICE*

# Chapter V

# Energy Harvesting Device

In recent years flexible nanogenerators, nanostructured piezoelectric energy harvester, have attracted a considerable interest to develop wearable energy harvesters and sensors for smart clothing applications. Piezoelectric polymers, such as the Poly(vinylidene fluoride) [PVDF] and novel polymer-based piezoelectric composites, are considered suitable candidates to fabricate such devices.

In this chapter we present the fabrication of a flexible nanogenerators using as active material a porous HMS-PVDF nanocomposites film. We selected such material due to its excellent piezoelectric, structural and mechanical properties. A critical issue in the fabrication of flexible nanogenerators is the electrical bonding of the piezoelectric material through flexible electrodes. In this chapter it is presented the fabrication of a flexible nanogenerator based on piezoelectric PVDF nanocomposite films, using as top and bottom electrodes a bilayer of graphene-gold (GGEs).

## *5.1 Introduction*

The energy harvesting from ambient vibrations originating from sources such as moving parts of machines, fluid flow and even body movement, has enormous potential for small power applications, such as wireless sensors, flexible, portable, wearable electronics, and biomedical implants, to name a few.

Vibrational mechanical energy is one of the most present and accessible forms of energy. Random vibrations have frequencies ranging from hundreds of Hz to kHz and the available energy density is in the range of a few hundred microwatts to milliwatt per cubic centimetre [21]. The most used and efficient devices used to transform vibrational energy in to electrical energy are the piezoelectric devices. Although a huge number of piezoelectric materials have been demonstrated since the discovery of piezoelectricity over a century ago, the use of piezoelectric nanostructure is a relatively recent topic.

Most studies focus on zinc oxide, as its nanostructures are formed relatively easily using low temperature methods [32], unlike many ferroelectrics which require high temperature processing. In addition, the nanostructures are crystallographically aligned and non- ferroelectric, and therefore do not require poling. However, recently, thanks to their high piezoelectric coefficients that permit to have a higher power output, other well-known materials have been investigated for nanostructured energy harvesters including lead zirconate titanate (PZT) and barium titanate. Nevertheless, all these materials are brittle and are not useful to produce flexible nanogenerators.

Piezoelectric polymers, such as the Poly(vinylidene fluoride) [PVDF; $(CH_2CF_2)_n$] are considered as suitable candidates to fabricate such devices. As already mentioned (see Chapter IV), PVDF has attracted much attention for its chemical resistance, thermal stability, high mechanical strength, large remnant polarization, short switching time and significant electrical properties [6,8,76,78].

A critical issue in the fabrication of flexible nanogenerators is the electrical bonding of the piezoelectric material through flexible electrodes. Graphene has been shown to be an excellent electrode for nanogenerators devices, due to its extraordinary electrical and mechanical properties, combined with a good flexibility [89].

Nevertheless, graphene makes the top contact very delicate and its adhesion to PVDF has yet to be tested in depth. Moreover, the sheet resistance of graphene remains still too high, around few 100 Ω/□ [90], to have a low-resistance electrode. For the aforementioned reasons, in this thesis, it is investigated the feasibility of using graphene-gold electrodes (GGEs) to guarantee high flexibility and high electrical conductivity. Actually, it is observed that the direct sputtering of gold electrodes over the surface of porous PVDF can be challenging, due to the fact that the sputtered gold diffuses through the polymer film and produces a short circuit between the top and bottom electrodes. To avoid these short circuits, we used graphene as an interlayer between the polymer and the sputtered gold. In this work it is used an organic compound, namely cyclododecane, to assist the transfer of the gold/graphene films [90].

In this chapter both the morphology and the electrical properties of three different graphene-gold bilayer electrodes, made with sputtered

gold layers of three different thicknesses (80, 50 and 30 nm) are characterized. The piezoelectric properties of the PVDF films with and without GGE are investigated through PFM. For comparison purposes, the macroscopic piezoelectric response (i.e. the piezoelectric coefficient $d_{33}$) of a flexible nanogenerator, with top and bottom bilayer electrodes structure, was characterized, by using a commercial mini-shaker. The produced nanogenerator was realized using as an active material the best PVDF nanocomposite film presented in Chapter IV, i.e. the R3-HS2 sample.

## 5.2 Device Fabrication

The fabrication of the flexible nanogenerators is based on two steps:

- Deposition of the nanocomposite PVDF films;
- Deposition of the graphene gold electrodes.

### 5.2.1 Deposition of PVDF Films

PVDF films were prepared by route R3, described in the previous Chapter IV, section 4.2.3. Briefly HMS are dissolved in a solvent mixture of DMF and acetone (1:1 v/v). Next, PVDF powder was added to the as-obtained nanofiller suspension and stirred for 3 h. The obtained solution is casted upon on a clean glass plate and evaporating the solvent at 100 °C for 12 h. Peeling off the film from the substrate a flexible self-standing film, having thickness of approximately 15 μm each, was obtained (see Fig. 52).

### 5.2.2 Deposition of Graphene-Gold Electrodes

Few layer graphene (FLG) films, in collaboration with ENEA, Casaccia, Italy, were grown on copper foils (25 μm thick) at 1070 °C in an inductively heated furnace by the Chemical Vapor Deposition (CVD) of ethanol ($C_2H_5OH$) at low pressure (8 mbar). The samples were previously annealed in Ar/$H_2$ (20/20 sccm) for 10 min at the same temperature. Three different gold layers: 80, 50 and 30 nm, were then sputtered on as-synthesized FLG coated copper foils. After removing the graphene grown on the back of the sample by oxygen plasma treatment, gold-graphene-copper substrates were spin-coated with cyclododecane as support layer. The substrates were treated in an etching solution of ammonium

persulfate (APS) and deionized water (200 g/l) to remove the copper foil, and then rinsed in deionized water to eliminate any Cu and etch bath residues. The gold/graphene/cyclododecane films were finally scooped from the rinsing bath using the desired substrate and transferred onto the previously obtained PVDF film (see section 5.2.1); cyclododecane was finally removed by heating at 65°C (see Fig. 68) [90].

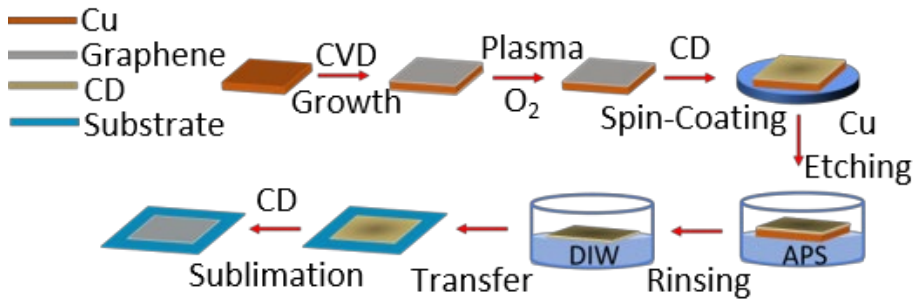


**Fig. 68 Preparation route of Few layer of graphene (FLG).**

## 5.3 *Morphological Characterizations*

The morphology of the GGE was observed using a FE-SEM (Zeiss Auriga) operated at an accelerating voltage of 5 kV, and an AFM (Dimension Icon, Bruker-Veeco) operated in tapping mode. FE-SEM images of neat PVDF, PVDF topped by graphene and PVDF topped by a graphene-gold electrode are shown in Fig. 69(a), (b), and (c), respectively. AFM images and corresponding height profiles of the same samples are show in Fig. 70(a)-(b), (c)-(d) and (e)-(f).

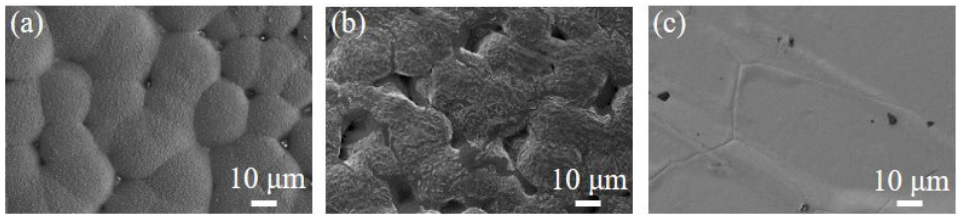


**Fig. 69 FE-SEM image of neat PVDF (a), PVDF with graphene only (b) and PVDF with graphene-gold electrode (c).**

The surface of the neat PVDF is characterized by a classic spherulitic structure. The morphology seems not to be altered by the presence of graphene. On the contrary, the roughness of the sample is highly affected by the topmost gold layer morphology.

## 5.4 *Electrical properties*

Flexibility and sheet resistance of the bilayer electrode can be in general tuned by modifying the thickness of the gold layer. The measured sheet resistance of the GGEs transferred on PVDF and, for sake of comparison, on $Si/SiO_2$ are reported in Table 7.

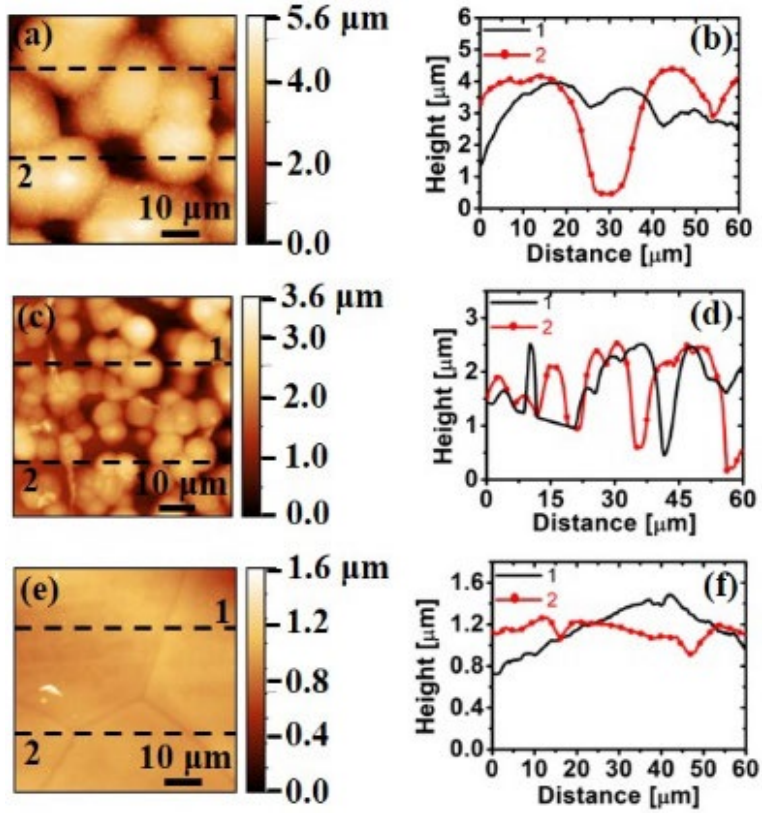


**Fig. 70 AFM topography and height profile along the black lines for neat PVDF (a)-(b), PVDF with graphene (c)-(d) and PVDF with GGE (e)-(f).**

**Table 7 Measured sheet resistance of the graphene-gold electrodes transferred on PVDF and on $Si/SiO_2$.**

| Sample | $R_s$ (Ω/□) | |
|---|---|---|
| | $Si/SiO_2$ | PVDF |
| FLG + Au 80 nm | 0.40 | 0.41 |
| FLG + Au 50 nm | 0.55 | 1.23 |
| FLG + Au 30 nm | 0.71 | 1.02 |

The insulation resistance tests carried on samples having the top electrode made of either a sputtered gold layer or graphene-gold bilayer have shown opposite results. In the former case, we measured resistances of a few Ohms, indicating that the top and bottom electrodes are in electrical contact. In the latter case we measured resistance values higher than 100 GΩ, demonstrating good electrical insulation between the two electrodes.

## *5.5 Piezoelectric response*

Using the procedure described in Chapter 2, section 2.2.4, the $d_{33}$ of the PVDF whiteout GGEs and with GGEs with 30 nm, 50 nm and 80 nm was measured. Three-dimensional topography and the piezoelectric contrast, scanning an area of (500×500) nm², are reported in Fig. 71.

Since the piezoelectric contrast does not directly correlate with the topography [86], the piezoelectric effect is due to intrinsic piezoelectric properties of the materials and not originated from the cross-talk with the topographic signal.

PFM measurements were performed on 3 different regions for each sample (scanning area (500×500) nm²) to evaluate the average piezoelectric properties of the samples. In Fig. 72 we report the average values of displacement as a function of the amplitude of the applied a.c. voltage. In agreement with the theory of the converse piezoelectric effect, a linear behavior of the piezoelectric response as a function of the applied voltage is obtained.

The difference between the $d_{33}$ obtained over the sample with and without the GGEs are reported in Table 8. A slightly lower value is obtained for the measurements without the top electrode.

However, the variation of the $d_{33}$ measured over the sample with and without the GGE was lower than 10%, apart for the sample with GGE with 50 nm of Au. This finding suggests that the local characterization using PFM technique is also a good representation of the global piezoelectric properties of the samples. Infact, while the PFM measurements performed with a top electrode probe a sample area equal to the surface of the top electrode, in our case around (1x1) cm², the PFM measurements without the top electrode probe a much smaller area (typically (500x500) nm²). The present results, i.e. a nearly equal $d_{33}$ values

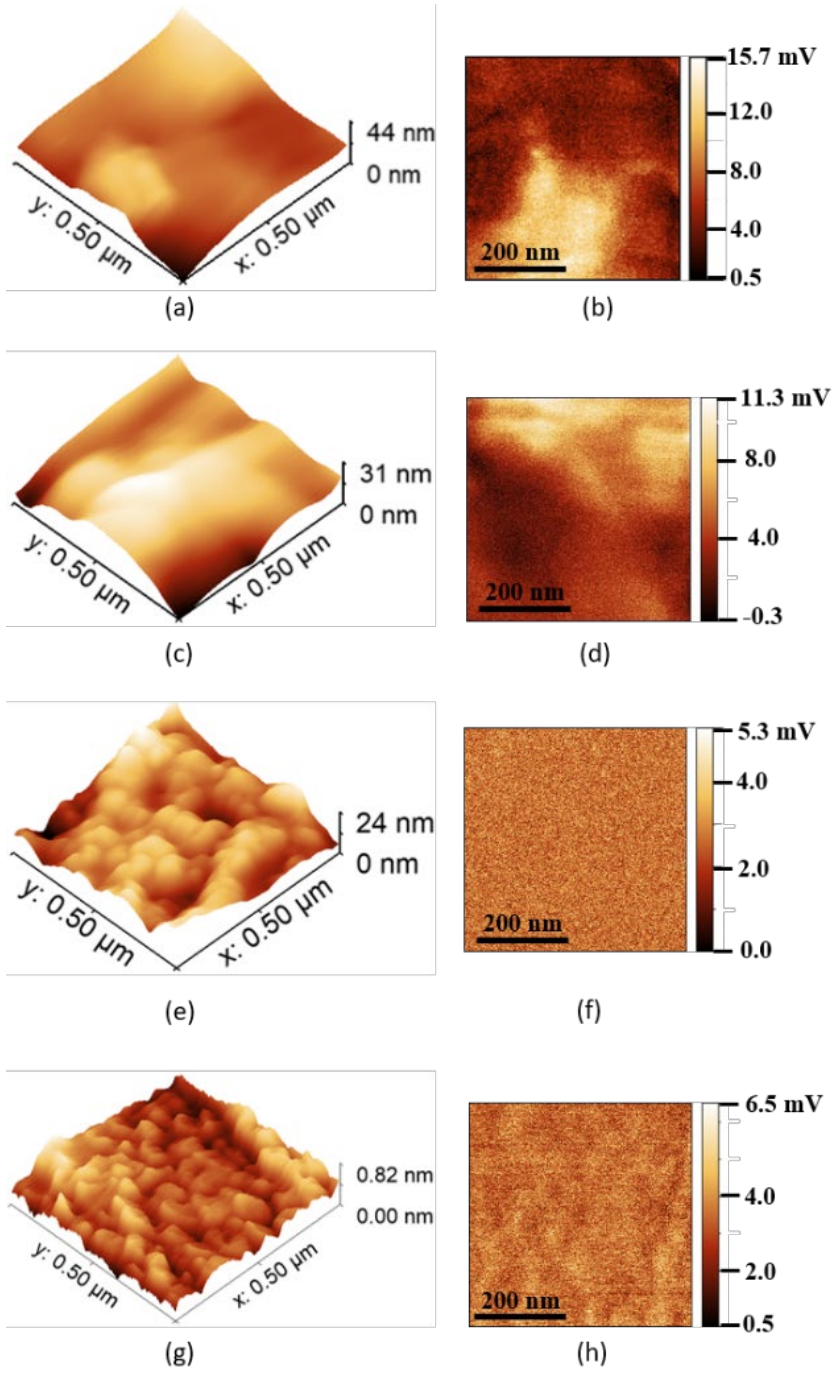


**Fig. 71 Three-dimensional topography and domain contrast of PFM at 10 V of PVDF without GGEs (a)-(b), of PVDF with GGEs with 30 nm of gold (c)-(d), of PVDF with GGEs with 50 nm of gold (e)-(f) and of PVDF with GGEs with 80 nm of gold (g)-(h).**

measured with and without top electrode, imply that the averaging of the PFM signal is able to provide a good estimate of the macroscale

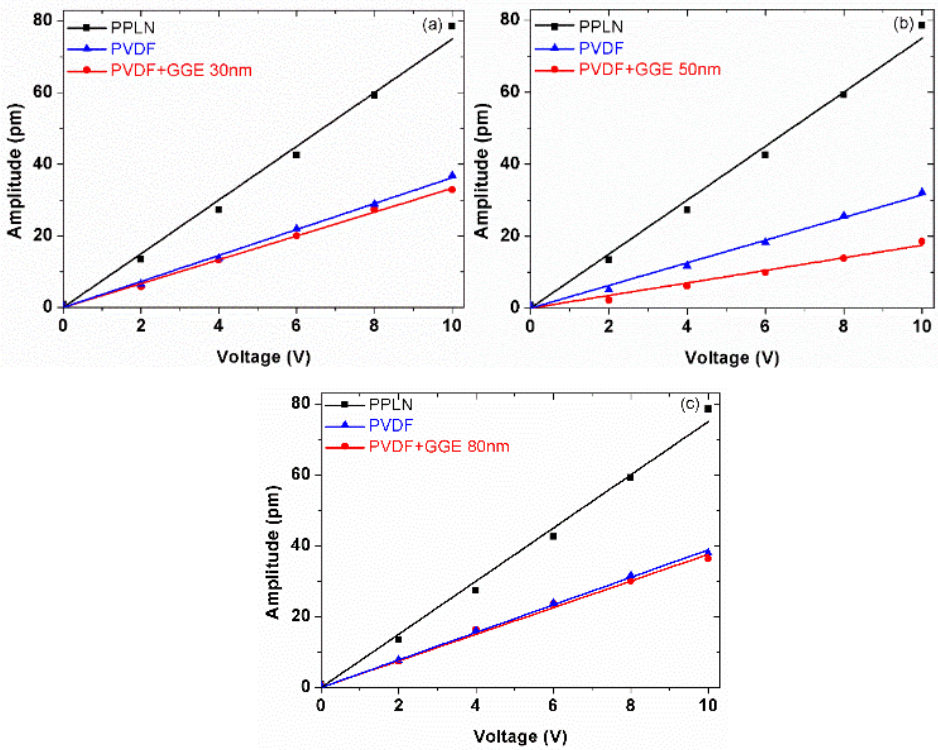


**Fig. 72 Measured piezoelectric signal, averaged over three different areas, versus the amplitude of the applied a.c. voltage. Comparison between PVDF and PVDF plus GGE with 30 nm of gold (a), PVDF and PVDF plus GGE with 50 nm of gold (b), PVDF and PVDF plus GGE with 80 nm of gold (c).**

piezoelectric response. In addition, these results also suggest that the classical capacitive configuration, where all the sample under the top electrode surface responds to the electrical stimulus, and the local PFM characterization, where the top electrode is represented by the conductive tip, provide evaluation of the $d_{33}$ value in very close agreement. The anomalous behavior of the GGE with 50 nm of Au, leading to a larger discrepancy between the two $d_{33}$ values, is probably due to the non-perfect adhesion of the top electrode with the PVDF films. However, further investigations are needed to support this hypothesis.

Since for all the three bilayer electrode structures it is found an excellent flexibility, it is finally adopted the thickest graphene-gold electrode, that showed the lowest value of sheet resistance both on the

**Table 8 Variation of the piezoelectric coefficient evaluated by averaging the PFM signal over 3 different areas each of (500x500) nm².**

| Sample | $\Delta d_{33}$ (pm/V) |
|---|---|
| PVDF+GGE 30 nm | 0.30 ± 0.03 |
| PVDF+GGE 50 nm | 1.40 ± 0.62 |
| PVDF+GGE 80 nm | 0.12 ± 0.01 |

$Si/SiO_2$ and on the PVDF, to fabricate a flexible nanogenerator. In order to produce the flexible nanogenerator we decided to use the R3-HS2 that showed the highest value of $d_{33}$ (8.88±3.14) pm/V. The flexible nanogenerator, fabricated according to the processes above described, is shown in Fig. 73 (b), while Fig. 73 (a) reports a schematic of the structure. The device was tested using a commercial mini-shaker with a force of 0.25 N at the frequency of 110 Hz. We obtained a value of 9.00 pm/V which is in good agreement with the one (8.88±3.14) pm/V measured through the PFM on the same PVDF film without electrodes.

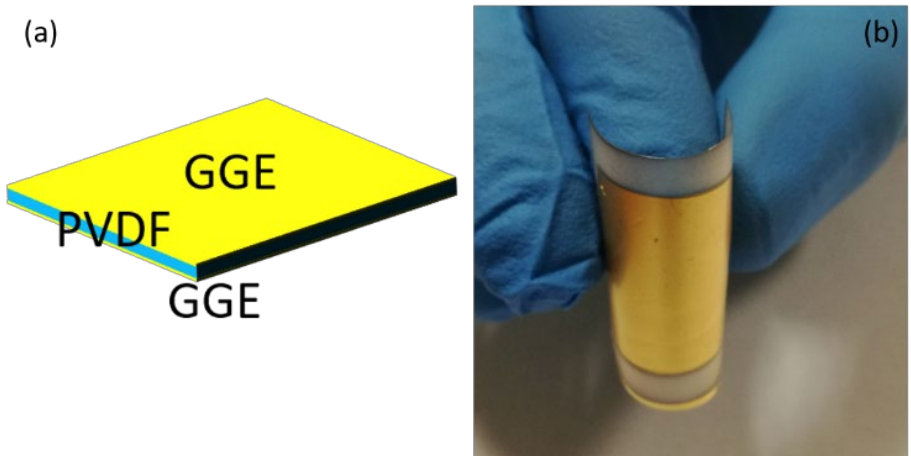


**Fig. 73 Schematic representation of the PVDF nanogenerator with graphene/gold electrodes (GGE) (a); picture of the fabricated flexible nanogenerator (b).**

# *CHAPTER VI*

## *CONCLUSION AND FUTURE PERSPECTIVE*

# Chapter VI

# Conclusions and Future Perspective

The objectives of this thesis were:

- to develop new piezoelectric materials, suitable for the fabrication of low-cost flexible nanogenerators;
- define a characterization protocol, based on the Piezoresponse Force Microscopy (PFM), allowing quantitative evaluation of the piezoelectric response, to easily compare different materials and using simple test structures;
- to demonstrate a flexible nanogenerator based on the developed piezoelectric materials.

To evaluate the piezoelectric properties of the investigated materials we developed a PFM procedure which provides a quantitative measurement of the piezoelectric coefficient at nano- and microscales, through a calibration protocol. To this purpose, the PFM signal is averaged over different areas of the samples (minimum three). Each area is less then (1 x 1) $\mu m^2$ in size in order to guarantee at the same time local information and, by averaging the collected measurements, the macroscopic information.

The synthesis of piezoelectric materials through cost-effective, simple and reliable approaches feasible for large-scale industrial production was also one of the main objectives of this work. Two different classes of piezoelectric materials have been investigated: 1) zinc oxide nanostructures, in particular zinc oxide nanoroads (ZnO-NRs) and zinc oxide nanowalls (ZnO-NWs); 2) piezoelectric polymer nanocomposites based on polyvinylidene fluoride (PVDF).

In particular, it has been presented a comparative study of the properties of 1D (NRs) and 2D (NWs) ZnO-nanostructures, grown by chemical bath deposition (CBD), for potential applications in energy harvesting devices. The CBD technique enables a high deposition rate on a wide variety of substrates and over large areas, being also a facile, cost-effective, non-toxic and easy-to scale-up approach.

The piezoelectric properties of the produced samples were investigated through PFM, by scanning different areas of the specimens.

We found a piezoelectric coefficient of (7.01 ± 0.33) pm/V for ZnO-NRs and (2.63 ± 0.49) pm/V for ZnO-NWs. In particular, the structural, chemical, and morphological properties of the nanostructure were correlated with the piezoelectric response of the produced nanostructured thin films. SEM and AFM analyses confirmed good orientation of the nanostructures. The XRD spectra confirmed a better crystallinity of ZnO-NRs than of ZnO-NWs. Therefore, ZnO-NRs were characterized by a vertical alignment and a well-defined hexagonal symmetry combined with a good crystallinity (sharp and intense peaks).

On the other hand, the XRD data of ZnO-NWs showed an anomalous spread of the (101) peak, which suggests a high defectiveness. The higher defectiveness of ZnO-NWs was also confirmed by PL measurements, highlighting an UV/VIS ratio lower for ZnO-NWs than for ZnO-NRs. The lack of a Bragg reflection at 17.2° in the XRD spectra suggested that sample defectiveness is not related to oxygen vacancies. Vice versa, the position of the centre of the visible PL-band in ZnO-NWs indicated that such defectiveness can be attributed to the presence of zinc vacancies.

This result was supported by XPS measurements, which showed a Zn/O ratio < 1, in agreement with the EDX measurements. From XPS measurements we also observed the absorption of water molecules (BE ≈ 533 eV), on the surface of ZnO-NRs.

The better piezoelectric properties of ZnO-NRs with respect to ZnO-NWs can be related to a combination of the outperforming structural properties, including a better orientation along the *c*-axis, and a lower defectivity of ZnO-NRs over ZnO-NWs. Furthermore, the obtained values of the piezoelectric coefficient, averaged over different areas of the sample surface are representative of the film response and not of the single nanostructure properties. This result suggests that PFM measurements can be employed as a routine test to assess the quality of the piezoelectric nanostructures.

Furthermore, a novel approach to increase the piezoelectric coefficient of PVDF is presented, avoiding the poling process, by inducing an increased $\beta$-phase fraction in the PVDF film through the addition of suitable quantities of nanofillers.

Using a simple, cost-effective, time-saving solution-casting process, without electrical poling, free standing flexible PVDF nanocomposite

films were produced. Four different routes have been investigated to induce an enhancement of the piezoelectric response of PVDF, including the addition of GNPs (R1), ZnO-NRs (R2), HMS (R3) and HMS in combination with the nanofillers (R4). The enhancement of the piezoelectric response of the nanocomposites can be explained by assuming that GNPs or ZnO NRs can influence the polymer structure arrangement, as to induce the $\beta$-phase formation in PVDF, as already reported in previous studies [54,73,91].

The results of this study show a qualitative correlation between induced $\beta$-phase, as assessed through FT-IR measurements, and intensity of the measured piezoelectric response, resulting from the PFM analysis.

Therefore, the obtained results demonstrate the piezoelectric behaviour of the nanocomposite films, induced by the presence of a $\beta$-phase, which is obtained without modification or functionalization of GNPs or ZnO NRs, nor through the application of any strain or electric field during the synthesis.

A higher value of $d_{33}$ adding nanofillers using R2 was obtained, despite the concentration of $\beta$-phase was lower than the samples obtained using R1. This behaviour can be correlated to the tip-sonication process, employed in route 1 to disperse GNPs, and that could lead to a reduction in the length of polymeric chains, resulting in a lower $d_{33}$.

The obtained results can be very attractive for the fabrication at low processing temperatures of energy harvesting devices or pressure sensors on flexible substrates, avoiding chemical modification or poling.

The other two different investigated synthesis routes are based on dissolution of HMS in the polymer (R3) or on nanofiller dispersion in combination with HMS-dissolution (R4).

FT-IR and XRPD investigations revealed that the incorporation of $Zn(NO_3)_2{\cdot}6H_2O$, $Mg(NO_3)_2{\cdot}6H_2O$, $MgCl_2{\cdot}6H_2O$, and $AlCl_3{\cdot}6H_2O$ salts into the PVDF matrix induces an increase of the electroactive phase, which can be ascribed to the combined effect of the change in the inherent dipole moment of the electroactive phase contained in the PVDF itself, and of the formation of H-bonding between the metallic part of the HMS filler and of PVDF via electrostatic interactions [85]. This combined effect is enhanced in the PVDF nanocomposite produced using HMS containing Mg nitrate, since $Mg^{2+}$ is characterized by the most negative redox

potential with respect to the other metal ions considered in this study. This result is in line with the finding that the sample produced through dissolution in PVDF of $FeCl_3 \cdot 6H_2O$, in which the ion $Fe^{3+}$ has a nearly zero standard potential, has a very poor piezoelectric response.

The increase of the β-phase fraction in the samples R3-HS1, R3-HS2, R3-HS3, and R3-HS4, produced through dissolution of an HMS containing metals with negative redox potential, was correlated to the enhancement of the piezoelectric coefficient, measured through PFM.

At the same time, the reduction of β-phase in the sample R3-HS5 containing Fe corresponds to the reduction of the piezoelectric coefficient compared with neat PVDF. In particular, the highest average value of $d_{33}$ (i.e., 8.88 ± 3.14 pm/V) and the highest local peak value (i.e., 13.49 pm/V) were measured in the sample containing $Mg(NO_3)_2 \cdot 6H_2O$ salt (R3-HS2). This sample also contained the highest fraction of β-phase (i.e., 82.18%) with respect to all other samples, and was characterized by the lowest average value of spherulite diameter (i.e., 11.87 ± 3.74 μm).

Another finding of this thesis is that although XRPD and FT-IR measurements show that samples R4-HS1-GNP and R4-HS1-ZnO present a higher fraction of β-phase than does the neat sample, PFM measurements showed an average $d_{33}$ lower than that of the neat sample. The reason for this should be related to a poor alignment of the electroactive polymer chains along the vertical axis due to a destructive electrostatic interaction between the metallic part of the HMS filler, the nanofillers (GNP and ZnO NRs), and the $CF_2$ group of the PVDF.

Moreover, from AFM topological analysis of the produced samples, we speculate that the microstructure of their surface has some influence on the piezoelectric response. A definitely negative effect on the piezoresponse coefficient of the samples produced by combining HMS-dissolution and nanofiller dispersion is observed in the case of agglomerate formation. In any case, it is worth underlining that if the samples produced through the production process R3 or R4 were analysed, it was observed that the piezoelectric coefficient increases as the relative fraction of β-phase rises.

Moreover, $d_{33}$ and the fraction of β-phase in general increase as the dimension of the averaged spherulite diameter decreases. The addition of HMS salts results in a marked improvement of the $d_{33}$ value [32,76,77]. In

particular, it was possible to enhance the piezoelectric coefficient of modified PVDF films with obtained values consistent with those reported in the literature [68,87,88], but through a facile, cost-effective, and time-saving production route.

The XRPD and FT-IR findings were corroborated by SEM investigation, revealing that the nucleation kinetics are enhanced by the presence of the HMS salts, as evidenced by the formation of an increasing number of spherulites with increasing numbers of nucleation sites, in turn leading to a reduction of the average spherulite diameter.

This result opens new routes to the possibility of producing electroactive polymers with tailored electroactive properties and resonant frequency, through the control of the effective piezoelectric properties of the material, which is achieved by means of nanofiller dispersion into the polymer matrix.

From the analysis of the materials investigated in this thesis we conclude that the dissolution of the HMS in PVDF shows the most attractive piezoelectric, structural and mechanical properties to fabricate a flexible nanogenerators. Therefore, it has been used as active material in a flexible nanogenerator, which was fabricated as test vehicle.

To fabricate flexible nanogenerator we also developed flexible electrodes based on bilayers consisting of graphene-gold layers. Such GGE were able to avoid short circuit between the top and bottom electrodes and guarantee, at the same time, low sheet resistance and high flexibility. The quality of our GGE was verified measuring the $d_{33}$, through PFM, over the neat PVDF films and over the PVDF films topped by a GGE electrode. The device was tested measuring the piezoelectric response using a commercial mini-shaker. The device was successfully operating and a value of 9.00pm/V was measured. This value was found in very good agreement with the value obtained through the PFM measurements (8.88 ± 3.14) pm/V (measured without top electrode).

In addition, we measured $d_{33}$ over PVDF with and without top GGE: we found that both values were in good agreement with each other. This finding provides evidences that the local characterization made using PFM is a good representation of the global piezoelectric properties of the samples, as measured using top electrodes.

Future perspectives of the present studies will be focused on the optimization of flexible nanogenerators, trying to improve the piezoelectric properties of the materials as well as the electrical contact formation. For instance, we plan to evaluate a hybrid system made of vertically aligned ZnO-NRs array embedded in PVDF polymer matrix on PET -ITO flexible substrates.

# Bibliography


[1] Steenwelle R J A 2007 *Characterization of piezo- and ferroelectric thin films by Scanning Probe Techniques*

[2] Yang J 2005 *An Introduction to the Theory of Piezoelectricity* ed D Y Gao and R W Ogden (Boston)

[3] Mercadelli E 2010 *Multilaminati Piezoelettrici a Gradiente Funzionale*

[4] Sirohi J and Chopra I 2000 Fundamental Understanding of Piezoelectric Strain Sensors *Journal of Intelligent Material Systems and Structures* **11** 246–57

[5] Belloni M P 2014 *Realizzazione e Caratterizzazione di Film in Nitruro di Alluminio e Prove di Funzionamento di un Cantiliver Commerciale* (Università degli studi di Padova)

[6] Li J, Seok S Il, Chu B, Dogan F, Zhang Q and Wang Q 2009 Nanocomposites of Ferroelectric Polymers with TiO 2 Nanoparticles Exhibiting Significantly Enhanced Electrical Energy Density *Advanced Materials* **21** 217–21

[7] Taylor G W, Burns J R, Kammann S M, Powers W B and Welsh T R 2001 The Energy Harvesting Eel: A Small Subsurface Ocean/River Power Generator *IEEE J. Oceanic Eng.*

[8] Granstrom J, Feenstra J, Sodano H A and Farinholt K 2007 Energy harvesting from a backpack instrumented with piezoelectric shoulder straps *Smart Mater. Struct.*

[9] Mandal D, Henkel K, Schmeißer D, Dipankar M, Karsten H and Dieter S 2012 The electroactive β-phase formation in Poly(vinylidene fluoride) by gold nanoparticles doping *Materials Letters* **73** 123–5

[10] Sajkiewicz P, Wasiak A and Goclowski Z 1999 Phase transitions during stretching of poly (vinylidene fluoride) *European polymer journal* 423–9

[11] Scheinbeim J, Nakafuku C, Newman B A and Pae K D 1979 High--pressure crystallization of poly (vinylidene fluoride) *Journal of Applied Physics* 4399–405

[12] Miller R L and Raisoni J 1976 Single crystals of poly (vinylidene fluoride) *Journal of Polymer Science: Polymer Physics Edition* 2325–6

[13] Luongo J 1972 Far--infrared spectra of piezoelectric polyvinylidene fluoride *Journal of Polymer Science Part A--2: Polymer Physics* 1119–23

[14] Sencadas V, Gregorio Filho R and Lanceros-Mendez S 2006

Processing and characterization of a novel nonporous poly(vinilidene fluoride) films in the β phase *Journal of Non-Crystalline Solids* **352** 2226–9

[15] Martins P, Lopes A C and Lanceros-Mendez S 2014 Electroactive phases of poly(vinylidene fluoride): Determination, processing and applications *Progress in Polymer Science* **39** 683–706

[16] Dakua I and Afzulpurkar N 2013 Piezoelectric Energy Generation and Harvesting at the Nano-Scale: Materials and Devices *Nanomaterials and Nanotechnology* **3** 21

[17] Besleaga C, Stan G E, Galca A C, Ion L and Antohe S 2012 Double layer structure of ZnO thin films deposited by RF-magnetron sputtering on glass substrate *Appl. Surf. Sci.* **258** 8819–24

[18] Zhang Y, Ram M K, Stefanakos E K and Goswami D Y 2012 Synthesis, Characterization, and Applications of ZnO Nanowires *Journal of Nanomaterials* **2012** 1–22

[19] Chandraiahgari C R 2015 *Scale-Up Production of Multifunctional Nanostuctured Materials for Energy and Environment Applications* (Sapienza University of Rome)

[20] Fraden J 2016 *Handbook of Modern Sensors* (Cham: Springer International Publishing)

[21] Roundy S, Leland E S, Baker J, Carleton E, Reilly E, Lai E, Otis B, Rabaey J M, Sundararajan V and Wright P K 2005 Improving Power Output for Vibration-Based Energy Scavengers *{IEEE} Pervasive Computing* **4** 28–36

[22] Becker M 2016 *Investigation of Ferroelectric Domain Walls in Lithium Niobate* (University of Bonn)

[23] Bruker Tapping mode

[24] Voigtländer B 2015 *Scanning Probe Microscopy* (Berlin, Heidelberg: Springer Berlin Heidelberg)

[25] Birk H 1991 The local piezoelectric activity of thin polymer films observed by scanning tunneling microscopy *Journal of Vacuum Science & Technology B: Microelectronics and Nanometer Structures* **9** 1162

[26] Güthner P and Dransfeld K 1992 Local poling of ferroelectric polymers by scanning force microscopy *Applied Physics Letters* **61** 1137–9

[27] Morelli A 2009 *Piezoresponse force microscopy of ferroelectric thin films* (University of Groningen)

[28] Jungk T, Hoffmann Á, Soergel E, Hoffmann A and Soergel E 2006

Quantitative analysis of ferroelectric domain imaging with piezoresponse force microscopy *Applied Physics Letters* **89** 163507

[29] Denning D, Guyonnet J and Rodriguez B J 2016 Applications of piezoresponse force microscopy in materials research: from inorganic ferroelectrics to biopiezoelectrics and beyond *International Materials Reviews* **61** 46–70

[30] Jungk T, Hoffmann Á and Soergel E 2006 Detection mechanism for ferroelectric domain boundaries with lateral force microscopy *Applied Physics Letters* **89** 042901

[31] Soergel E 2011 Piezoresponse Force Microscopy (PFM) *Journal of Physics D: Applied Physics* **44** 464003

[32] Fortunato M, Chandraiahgari C R, De Bellis G, Ballirano P, Soltani P, Kaciulis S, Caneve L, Sarto F and Sarto M S M S 2018 Piezoelectric Thin Films of ZnO-Nanorods/ Nanowalls Grown by Chemical Bath Deposition *IEEE Transactions on Nanotechnology* 1–1

[33] Bekermann D, Gasparotto A, Barreca D, Devi A, Fischer R A, Kete M, Stangar U L, Lebedev O I, Maccato C, Tondello E and Van Tendeloo G 2010 ZnO Nanorod Arrays by Plasma-Enhanced CVD for Light-ActivatedFunctional Applications *Chem.Phys.Chem.* **11** 2337–40

[34] Lin C C and Li Y Y 2009 Synthesis of ZnO nanowires by thermal decomposition of zinc acetate dihydrate *Materials Chemistry and Physics* **113** 334–7

[35] Chandraiahgari C R, De Bellis G, Ballirano P, Balijepalli S K, Kaciulis S, Caneve L, Sarto F and Sarto M S 2015 Synthesis and characterization of ZnO nanorods with a narrow size distribution *RSC Advances* **5**

[36] Cao B and Cai W 2008 From ZnO Nanorods to Nanoplates: Chemical Bath Deposition Growth and Surface-Related Emissions *The Journal of Physical Chemistry C* **112** 680–5

[37] Strano V, Urso R G, Scuderi M, Iwu K O, Simone F, Ciliberto E, Spinella C and Mirabella S 2014 Double Role of HMTA in ZnO Nanorods Grown by Chemical Bath Deposition *The Journal of Physical Chemistry C* **118** 28189–95

[38] Yi G-C, Wang C and Park W Il 2005 ZnO nanorods: synthesis, characterization and applications *Semiconductor Science and Technology* **20** S22–34

[39] Falconi C, Mantini G, D'Amico A and Wang Z L 2009 Studying piezoelectric nanowires and nanowalls for energy harvesting

*Sensors and Actuators, B: Chemical* **139** 511–9

[40] Warule S S, Chaudhari N S, Kale B B and More M A 2009 Novel sonochemical assisted hydrothermal approach towards the controllable synthesis of ZnO nanorods, nanocups and nanoneedles and their photocatalytic study *CrystEngComm* **11** 2776

[41] Rai P, Raj S, Lee I-H, Kwak W-K and Yun Y-T 2013 Conversion of ZnO microrods into microdisks like structures and its effect on photoluminescence properties *Ceram. Int.* **39** 8287–91

[42] Chandraiahgaria C R, De Bellis G, Balijepalli S K, Kaciulis S, Ballirano P, Migliori A, Morandi V, Caneve L, Sarto F and Sarto M S 2016 Control of size and density of ZnO-nanorods grown onto graphene nanoplatelets in aqueous suspensions *RSC Advances* **1** 1–3

[43] Umar A, Ribeiro C, Al-Hajry A, Masuda Y and Hahn Y B 2009 Growth of highly c-axis-oriented ZnO nanorods on ZnO/glass substrate: growth mechanism, structural, and optical properties *J. Phys. Chem. C* **113** 14715–20

[44] Sowa H and Ahsbahs H 2006 High-pressure X-ray investigation of zincite ZnO single crystals using diamond anvils with an improved shape *J. of Applied Crystallography* **39** 169–75

[45] Di Marco M, Port M, Couvreur P, Dubernet C, Ballirano P and Sadun C 2006 Structural Characterization of Ultrasmall Superparamagnetic Iron Oxide (USPIO) Particles in Aqueous Suspension by Energy Dispersive X-ray Diffraction (EDXD) *Journal of the American Chemical Society* **128** 10054–9

[46] Di Marco M, Ballirano P, Port M, Piscopiello E, Couvreur P, Dubernet C and Sadun C 2009 Atomic Pair Distribution Function (PDF) study of iron oxide nanoparticles in aqueous suspension *Journal of Materials Chemistry* **19** 6354–60

[47] Ballirano P, De Vito C, Ferrini V and Mignardi S 2010 The thermal behaviour and structural stability of nesquehonite, MgCO3·3H2O, evaluated by in situ laboratory parallel-beam X-ray powder diffraction: New constraints on CO2 sequestration within minerals *Journal of Hazardous Materials* **178** 522–8

[48] Moulder J F, Stickle W F, Sobol P E and Bomben K D 1992 *Handbook of X-ray Photoelectron Spectroscopy* ed P E D J.Chastain Perkin-Elmer Corp. (Eden Prairie)

[49] Barreca D, Gasparotto A, Maccato C, Maragno C and Tondello E 2007 TiO 2 Thin Films by Chemical Vapor Deposition: An XPS

Characterization *Surface Science Spectra* **14** 27–33

[50] Kaciulis S, Pandolfi L, Comini E, Faglia G, Ferroni M, Sberveglieri G, Kandasamy S, Shafiei M and Wlodarski W 2008 Nanowires of metal oxides for gas sensing applications *Surf. Interface Anal.* **40** 575–8

[51] Kaciulis S, Mattogno G, Galdikas A, Mironas A and Setkus A 1996 Influence of surface oxygen on chemoresistance of tin oxide film *J. Vac. Sci. Technol., A* **14** 3164

[52] Shalish I, Temkin H and Narayanamurti V 2004 Size-dependent surface luminescence in ZnO nanowires *Phys. Rev. B: Condens. Matter Mater. Phys.* **69** 245401

[53] Jiang S, Ren Z, Gong S, Yin S, Yu Y, Li X, Xu G, Shen G and Han G 2014 Tunable photoluminescence properties of well-aligned ZnO nanorod array by oxygen plasma post-treatment *Appl. Surf. Sci.* 252

[54] Chandraiahgari C R, De Bellis G, Ballirano P, Balijepalli S K, Kaciulis S, Caneve L, Sarto F, Sarto M S, Bellis G De, Ballirano P, Balijepalli S K, Kaciulis S, Caneve L, Sarto F and Sarto M S 2015 Synthesis and characterization of ZnO nanorods with a narrow size distribution *{RSC} Adv.* **5** 49861–70

[55] Djurisic A B, Leung Y H, Tam K H, Ding L, Ge W K, Chen H Y and Gwo S 2006 Green, yellow, and orange defect emission from ZnO nanostructures: Influence of excitation wavelength *Appl. Phys. Lett.* 103107

[56] Heo Y W and Pearton S J 2005 Origin of green luminescence in ZnO thin film grown by molecular-beam epitaxy *J. of Applied Physics* **98** 73502

[57] Tay Y Y, Tan T T, Boey F, Liang M H, Ye J, Zhao Y, Norby T and Li S 2010 Correlation between the characteristic green emissions and specific defects of ZnO *Phys. Chem. Chem. Phys.* **12** 6008

[58] Fabbri F, Villani M, Catellani A, Calzolari A, Cicero G, Calestani D, Calestani G, Zappettini A, Dierre B, Sekiguchi T and Salviati G 2015 Zn vacancy induced green luminescence on non-polar surfaces in ZnO nanostructures *Scientific Reports* **4** 5158

[59] Katerinopoulou A, Balic-Zunic T and Lundegaard L F 2012 Application of the ellipsoid modeling of the average shape of nanosized crystallites in powder diffraction *J. of Applied Crystallography* **45** 22

[60] Kaurova I A, Kuzmicheva G M and Rybakov V B 2013 Growth and Structural, Optical, and Electrical Properties of Zincite Crystals

*Crystallography Reports* **58** 226–33

[61] Tamvakos D, Lepadatu S, Antohe V-A, Tamvakos A, Weaver P M, Piraux L, Cain M G and Pullini D 2015 Piezoelectric properties of template-free electromechemically grown ZnO nanorod arrays *Appl. Surf. Sci.* **356** 1214–20

[62] Gupta M K, Lee J-H, Lee K Y and Kim S-W 2013 Two-Dimensional Vanadium-Doped ZnO Nanosheet-Based Flexible Direct Current Nanogenerator *ACS Nano* **7** 8932–9

[63] Jana S, Garain S, Ghosh S K, Sen S and Mandal D 2016 The preparation of γ-crystalline non-electrically poled photoluminescant ZnO-PVDF nanocomposite film for wearable nanogenerators *Nanotechnology* **27** 445403

[64] Bohlen M and Bolton K 2015 Inducing the β-phase of poly(vinylidene fluoride)-a review *Rev. Nanosci. and Nanotech.* **1** 150110

[65] Gomes J, Serrado Nunes J, Sencadas V and Lanceros-Mendez S 2010 Influence of the β-phase content and degree of crystallinity on the piezo- and ferroelectric properties of poly(vinylidene fluoride) *Smart Materials and Structures* **19** 065010

[66] Kang S B, Won S H, Im M J, Kim C U, Park W Il, Baik J M and Choi K J 2017 Enhanced piezoresponse of highly aligned electrospun poly(vinylidene fluoride) nanofibers *Nanotechnology* **28** 395402

[67] Ramasundaram S, Yoon S, Kim K J and Lee J S 2008 Direct Preparation of Nanoscale Thin Films of Poly(vinylidene fluoride) Containing β-Crystalline Phase by Heat-Controlled Spin Coating *Macromol. Chem. Phys.* **209** 2516–26

[68] Lopes A C, Costa C M, Tavares C J, Neves I C and Lanceros-Mendez S 2011 Nucleation of the Electroactive γ Phase and Enhancement of the Optical Transparency in Low Filler Content Poly(vinylidene)/Clay Nanocomposites *The Journal of Physical Chemistry C* **115** 18076–82

[69] Wang Vand Deng Y, Xiang Y and Guo L 2008 Fabrication of radial ZnO nanowire clusters and radial ZnO/PVDF composites with enhanced dielectric properties *Adv. Funct. Mater.* 2584–92

[70] Patil R, Ashwin A and Radhakrishnan S 2007 Novel polyaniline/PVDF/BaTiO3 hybrid composites with high piezo-sensitivity *Sensors and Actuators A: Physical* **138** 361–5

[71] He X and Yao K 2006 Crystallization mechanism and piezoelectric properties of solution-derived ferroelectric poly(vinylidene

fluoride) thin films *Applied Physics Letters* **89**

[72] Yu S, Zheng W, Yu W, Zhang Y, Jiang Q and Zhao Z 2009 Formation mechanism of β-phase in PVDF/CNT composite prepared by the sonication method *Macromolecules* **42** 8870–4

[73] Bidsorkhi H C, D'Aloia A G, De Bellis G, Proietti A, Rinaldi A, Fortunato M, Ballirano P, Bracciale M P, Santarelli M L and Sarto M S 2017 Nucleation effect of unmodified graphene nanoplatelets on PVDF/GNP film composites *Materials Today Communications* **11** 163–73

[74] De Bellis G, Tamburrano A, Dinescu A, Santarelli M L L and Sarto M S S 2011 Electromagnetic properties of composites containing graphite nanoplatelets at radio frequency *Carbon* **49** 4291–300

[75] Tamburrano A, Sarasini F, De Bellis G, D'Aloia A G and Sarto M S S 2013 Piezoresistive effect in graphene-based polymeric composites *Nanotechnology* **24** 465702

[76] Fortunato M, Bidsorkhi H C C, De Bellis G, Sarto F and Sarto M S S 2017 Piezoelectric Response of Graphene-Filled PVDF Nanocomposites Through Piezoresponse Force Microscopy (PFM) *Proceedings of the 17th IEEE International Conference on Nanotechnology Pittsburgh, USA*

[77] Fortunato M, Bidsorkhi H C, Chandraiahgari C R, De Bellis G, Sarto F and Sarto M S 2018 PFM Characterization of PVDF Nanocomposite Films With Enhanced Piezoelectric Response *IEEE Transactions on Nanotechnology* **17** 955–61

[78] Fortunato M, Chandraiahgari C, De Bellis G, Ballirano P, Sarto F, Tamburrano A and Sarto M 2018 Piezoelectric Effect and Electroactive Phase Nucleation in Self-Standing Films of Unpoled PVDF Nanocomposite Films *Nanomaterials* **8** 743

[79] Bidsorkhi H C 2017 *Large Scale Production of Porous and Non-Porous PVDF/GNPs Nanocomposites for Electrical and Electromechanical Applications* (Sapienza University of Rome)

[80] Paliotta L, De Bellis G, Tamburrano A, Marra F, Rinaldi A, Balijepalli S K, Kaciulis S and Sarto M S 2015 Highly conductive multilayer-graphene paper as a flexible lightweight electromagnetic shield *Carbon* 260–71

[81] Chandraiahgari C R R, De Bellis G, Martinelli A, Bakry A, Tamburrano A and Sarto M S S 2015 Nanofiller induced electroactive phase formation in solution derived poly(vinylidene fluoride) polymer composites *2015 IEEE 15th International*

*Conference on Nanotechnology (IEEE-NANO)* (IEEE) pp 1346–9

[82] Bottino A, Capannelli G, Munari S and Turturro A 1988 Solubility parameters of poly(vinylidene fluoride) *Journal of Polymer Science Part B: Polymer Physics* **26** 785–94

[83] Garain S, Kumar Sinha T, Adhikary P, Henkel K, Sen S, Ram S, Sinha C, Schmeißer D and Mandal D 2015 Self-poled transparent and flexible UV light-emitting cerium complex-PVDF composite: A high-performance nanogenerator *ACS Applied Materials and Interfaces* **7** 1298–307

[84] Gregorio R J and Borges D S 2008 Effect of crystallization rate on the formation of the polymorphs of solution cast poly(vinylidene fluoride) *Polymer* **49** 4009–16

[85] Jana S, Garain S, Sen S and Mandal D 2015 The influence of hydrogen bonding on the dielectric constant and the piezoelectric energy harvesting performance of hydrated metal salt mediated {PVDF} films *Phys. Chem. Chem. Phys.* **17** 17429–36

[86] Nunes J S, Wu A, Gomes J, Sencadas V, Vilarinho P M, Lanceros-Mendez S, Serrado Nunes J, Wu A, Gomes J, Sencadas V, Vilarinho P M and Lanceros-Méndez S 2009 Relationship between the microstructure and the microscopic piezoelectric response of the $\alpha$- and $\beta$-phases of poly(vinylidene fluoride) *Appl. Phys. A* **95** 875–80

[87] Kim G H, Hong S M and Seo Y 2009 Piezoelctric properties of poly(vnylidene fluoride) and carbon nanotube blends: $\beta$-phase develpment *Phys. Chem. Chem. Phys.* **11** 10506–12

[88] Bystrov V S, Bdikin I K, Silibin M V, Karpinsky D V, Kopyl S A, Goncalves G, Sapronova A V, Kuznetsova T and Bystrova V V 2017 Graphene/graphene oxide and polyvinylidene fluoride polymer ferroelectric composites for multifunctional applications *Ferroelectrics* **509** 124–42

[89] Kwon J, Sharma B K and Ahn J-H 2013 Graphene Based Nanogenerator for Energy Harvesting *Japanese Journal of Applied Physics* **52** 06GA02

[90] Capasso A, Francesco M De, Leoni E, Dikonimos T, Buonocore F, Lancellotti L, Bobeico E, Sarto M S, Tamburrano A, Bellis G De and Lisi N 2014 Cyclododecane as support material for clean and facile transfer of large-area few-layer graphene *Applied Physics Letters* **105** 113101

[91] Layek R K, Samanta S, Chatterjee D P and Nandi A K 2010 Physical and mechanical properties of poly (methyl methacrylate)-

functionalized graphene/poly (vinylidine fluoride) nanocomposites: Piezoelectric $β$ polymorph formation *Polymer* 5846–56

# Acknowledgments

The PhD activity has been an immensely valuable experience during which I have learnt and acclimatized the necessary research skills for innovation. Firstly, I want to thank my supervisor Prof. Maria Sabrina Sarto for her precious teachings and her professional help. I want also to thank all the members of the group that I had the pleasure of meeting during the PhD experience and in particular: Alessio, Giovanni, Agnese, Andrea, Alessandro, Fabrizio, Domenico and Hossein. They made these years lighter and funnier.

I want to thank Dr. Soergel for having allowed me to be part of her research group. She taught me a lot about PFM with her helpful comments and discussion. In a short period, only a month, I gained a lot of knowledge.

A huge thanks goes to my historic group of friends, the "AM": Adriano, Agnese, Alessandro, Alessia, Beatrice, Claudia, Giulia, Lorenzo, Paolo and Silvia for always being present and for supporting me.

Finally, huge thanks go to my amazing parents: they always believed in me and supported me. They are always pushing me to go on. My father always helps me to think lucidly and I want to thank him for his precious advice. My mother is a priceless woman that takes care of everything since I was a baby. She taught me to work hard and to be honest every day. My sister is always present during the important moments of my life and is always available to help me. I also thank my grandmother who is always proud of me.

*……. Thanks for all.*

*Marco*

# Publications List

**Journals**

- **M. Fortunato**, C.R. Chandraiahgari, G. De Bellis, P. Ballirano F. Sarto, A. Tamburrano and M.S. Sarto "**Piezoelectric Effect and Electroactive Phase Nucleation in Self-Standing Films of Unpoled PVDF Nanocomposite Films**", Nanomaterials, 8(9), 2018.
- **M. Fortunato**, H.C. Bidsorkhi, C.R. Chandraiahgari, G. De Bellis, F. Sarto and M.S. Sarto "**PFM Characterization of PVDF Nanocomposite Films with Enhanced Piezoelectric Response**", IEEE Transaction on Nanotechnology, 17(5), 2018.
- **M. Fortunato**, C.R. Chandraiahgari, G. De Bellis, P. Ballirano, P. Soltani, S. Kaciulis, L. Caneve, F, Sarto and M.S. Sarto "**Piezoelectric Thin Films of ZnO-Nanorods/ Nanowalls Grown by Chemical Bath Deposition**", IEEE Transaction on Nanotechnology, 17(2), 2018.
- **M.Fortunato**, H.C. Bidsorkhi, G. De Bellis, F. Sarto and M.S. Sarto "**Piezoelctric Response of Graphene-Filled PVDF Nanocoposites Trought Piezoresponse Force Microscopy (PFM)**", Proceedings IEEE Nano 2017, p. 125-129, 2017.
- H.C. Bidsorkhi, A.G. D'Aloia, G. De Bellis, A. Proietti, A. Rinaldi, **M. Fortunato**, P. Ballirano, M.P. Bracciale, M.L. Santarelli and M. S. Sarto "**Nucleation effect of unmodified graphene nanoplatelets on PVDF/GNP film composites**", *Materials Today Communications*, 11, 2017.
- A. Rinaldi, A. Tamburrano, **M. Fortunato** and M.S. Sarto "**A Flexible and Highly Sensitive Pressure Sensor Based on a PDMS Foam Coated with Graphene Nanoplatelets**", Sensors, 16 (12), 2016.

**Conferences**

- **M.Fortunato**, A. Rinaldi, A. Tamburrano, T. Dikonimos, G. De Bellis, N. Lisi, and M.S. Sarto "**Graphene-Gold Electrodes for Flexible Nanogenerators Based on Porous Piezoelectric PVDF**", Nanoinnovation 2018, Rome, 11-14 September 2018, oral presentation.
- D. Cavallini, **M. Fortunato**, G. De Bellis and M.S. Sarto "**PFM Characterization of Piezoelectric PVDF/ZnO-Nanorod thin films**", Nanoinnovation 2018, Rome, 11-14 September 2018, oral presentation.

- **M.Fortunato**, A. Rinaldi, A. Tamburrano, T. Dikonimos, G. De Bellis, N. Lisi, and M.S. Sarto "**Graphene-Gold Electrodes for Flexible Nanogenerators Based on Porous Piezoelectric PVDF Films**", IEEE NANO 2018, Cork, 23-26 July, 2018, Poster.

- D. Cavallini, **M. Fortunato**, G. De Bellis and M.S. Sarto "**PFM characterization of PVDF-ZnO hybrid structures for energy harvesting**", IEEE NANO 2018, Cork, 23-26 July 2018, oral presentation.

- **M.Fortunato**, A. Rinaldi, A. Tamburrano, T. Dikonimos, G. De Bellis, N.Lisi, and M.S. Sarto "**Elettrodi di Grafene-Oro per Nanogeneratori Flessibili Basati su Films di PVDF Piezoelettrici Porosi**", ET 2018, Rome, 13-14 Jun 2018, Poster.

- D. Cavallini, **M. Fortunato**, G. De Bellis and M.S. Sarto "**Film Polimerici Piezoelettrici in PVDF e nanorod di ZnO e Caratterizzazione Mediante Piezo Force Microscopy**", ET 2018, Rome, 13-14 Jun 2018, Poster, award for best poster.

- D.Cavallini, C.R. Chandraiahgari, G. De Bellis, **M. Fortunato**, A. Bregnocchi and M.S. Sarto "**Synthesis and characterization of zinc-oxide nanostructures for application in cultural heritage**", Nanoinnovation 2017, Rome, 26-29 September 2017, oral presentation.

- **M.Fortunato**, H.C. Bidsorkhi, G. De Bellis, F. Sarto and M.S. Sarto "**Piezoelctric Response of Graphene-Filled PVDF Nanocoposites Trought Piezoresponse Force Microscopy (PFM)**", IEEE Nano 2017, Pittsburgh (USA), 25-28 July 2017, oral presentation.